

<b>REPORT DOCUMENTATION PAGE</b>			Form Approved OMB No. 0704-0188		
Public reporting burden for this collection of information is estimated to average 1 hour per response, including the time for reviewing instructions, searching existing data sources, gathering and maintaining the data needed, and completing and reviewing this collection of information. Send comments regarding this burden estimate or any other aspect of this collection of information, including suggestions for reducing this burden to Department of Defense, Washington Headquarters Services, Directorate for Information Operations and Reports (0704-0188), 1215 Jefferson Davis Highway, Suite 1204, Arlington, VA 22202-4302. Respondents should be aware that notwithstanding any other provision of law, no person shall be subject to any penalty for failing to comply with a collection of information if it does not display a currently valid OMB control number. <b>PLEASE DO NOT RETURN YOUR FORM TO THE ABOVE ADDRESS.</b>					
<b>1. REPORT DATE (DD-MM-YYYY)</b> February 1, 2010		<b>2. REPORT TYPE</b> Final Report		<b>3. DATES COVERED (From - To)</b> 11/01/2006 - 10/31/2009	
<b>4. TITLE AND SUBTITLE</b>  Gravity-Wave Dynamics in the Atmosphere			<b>5a. CONTRACT NUMBER</b>		
			<b>5b. GRANT NUMBER</b> FA9550-07-1-0005		
			<b>5c. PROGRAM ELEMENT NUMBER</b>		
<b>6. AUTHOR(S)</b>  Akylas, Triantaphyllos, R.			<b>5d. PROJECT NUMBER</b>		
			<b>5e. TASK NUMBER</b>		
			<b>5f. WORK UNIT NUMBER</b>		
<b>7. PERFORMING ORGANIZATION NAME(S) AND ADDRESS(ES)</b>  Massachusetts Institute of Technology 77 Massachusetts Avenue Cambridge, MA 02139			<b>8. PERFORMING ORGANIZATION REPORT NUMBER</b>		
<b>9. SPONSORING / MONITORING AGENCY NAME(S) AND ADDRESS(ES)</b>  Air Force Office of Scientific Research i ifi Dr. Arje Nachman - NE 875 North Randolph Road Ste. 325, Room 3112 Arlington, VA 22203			<b>10. SPONSOR/MONITOR'S ACRONYM(S)</b>		
			<b>11. SPONSOR/MONITOR'S REPORT NUMBER(S)</b>		
<b>12. DISTRIBUTION / AVAILABILITY STATEMENT A</b>					
<b>13. SUPPLEMENTARY NOTES</b>					
<b>14. ABSTRACT</b> Motivated by reports of accidents in high-altitude aircraft flights due to unforecast turbulence caused by gravity waves over mountain ranges, this research program aimed to advance the theoretical understanding of physical mechanisms responsible for the generation of gravity waves by wind over orography. Specifically, a systematic study was made of the role of the Earth's rotation under various atmospheric conditions. It was found that rotation can contribute to significantly increased gravity-wave activity when the tropopause (the border between the troposphere and the stratosphere) is located at certain heights over mesoscale mountains. Under such 'tuned' conditions, the combined effect of rotation and nonlinear interactions is to drive inertia-gravity waves that propagate far downstream from the mountain. The effect of temporal variations in the wind velocity was also studied for time scales typically encountered in the field. It was found that small-amplitude oscillatory wind components play an important part, and the wave response to unsteady wind can be quite stronger than that predicted by assuming an average steady wind profile. Finally, a preliminary study was made of the radiation of gravity waves by weakly nonlinear wavepackets arising from shear-flow instabilities.					
<b>15. SUBJECT TERMS</b>					
<b>16. SECURITY CLASSIFICATION OF:</b>			<b>17. LIMITATION OF ABSTRACT</b>	<b>18. NUMBER OF PAGES</b>	<b>19a. NAME OF RESPONSIBLE PERSON</b>
<b>a. REPORT</b>	<b>b. ABSTRACT</b>	<b>c. THIS PAGE</b>			<b>19b. TELEPHONE NUMBER (include area code)</b>

## I. EXECUTIVE SUMMARY

Motivated by reports of accidents in high-altitude aircraft flights due to unforecast stratospheric turbulence caused by gravity waves over mountains, this research program aimed to improve the theoretical understanding of various physical mechanisms relevant to the generation of stratospheric gravity waves by orography. Specifically, the main objectives were to study: the effects of the Earth's rotation on nonlinear mountain inertia-gravity waves; the generation of gravity waves by transient wind over mountains; the interaction of mountain gravity waves with the tropopause and possible amplification of these waves in the stratosphere; and possible transfer of energy from shear-flow instabilities to low-frequency inertia-gravity waves via resonant nonlinear interactions.

Towards reaching these goals, the following problems have been studied:

(i) *Effect of the Earth's rotation on nonlinear mountain waves.* Formally, the effect of rotation on the generation of mountain waves by wind is controlled by the Rossby number,  $Ro = U/(Lf)$ , where  $U$  denotes the wind speed,  $L$  is the mountain length and  $f$  the Coriolis parameter. Rotation is expected to be relatively unimportant when  $Ro \geq \mathcal{O}(1)$ , and this regime is realized if the mountain is not too long,  $L \leq 50$  km typically. However, even when  $Ro \gg 1$ , rotation does affect the low-frequency part of the gravity wave spectrum, suggesting that weak rotation effects could become important at long distances from the mountain. This, in turn, raises the question: under what conditions can rotation be safely neglected in analyzing/modeling mountain waves?

We have addressed this issue by constructing an asymptotic model. It turns out that rotation behaves as a 'singular perturbation': the effects of rotation become equally important to the effects of stratification far from the mountain, regardless of how large  $Ro$  is. As a result, the response far from the mountain is dominated by inertia-gravity waves that would be absent had rotation been ignored. Hence, the wave signature of the mountain extends much further than would be expected. This piece of work forms part of the doctoral thesis of B. Druecke (in preparation). For technical details, see §1 in Sec. II below.

(ii) *Combined effect of rotation and the tropopause.* The asymptotic model above was generalized to account for the combined effect of the Earth's rotation and the tropopause. In the presence of the tropopause, the induced wave disturbance over the mountain can be dramatically increased when the tropopause is at certain heights (depending on the wind speed and the stratification). Under such 'tuned' conditions, nonlinear wave interactions are particularly strong and, combined with rotation, drive inertia-gravity waves that propagate far downstream of the mountain. Our theoretical results indicate that this generation mechanism is robust for mesoscale mountains, and rotation effects can be far more important than previously thought, especially when tropopause tuning is taken into account. A numerical code was also written for solving the Euler equations in the presence of stratification and rotation. Fully numerical simulations of unsteady responses for various heights of the tropopause lend support to the theoretical predictions. This piece of work is also part of B. Druecke's doctoral thesis (in preparation). Technical details can be found in §2 of Sec. II.

(iii) *Effect of unsteady wind on nonlinear mountain waves.* Previous work on mountain gravity waves invariably assumes steady wind; apart from a few studies of the effect of a time-harmonic wind component on the linear response, the possible significance of wind variations remains unexplored theoretically. Using an earlier study by Kantzios and Akylas (Proc. Roy. Soc. Lond. A **440**, 1993) as the starting point, an asymptotic model was developed for the evolution of the nonlinear response in the presence of slowly varying wind (timescale of the order of hours). In the case of time-harmonic wind variation, the model reveals that the appropriate perturbation parameter is the relative amplitude of the oscillatory wind component divided by the wind frequency (made dimensionless by the buoyancy frequency). As a result, a small-amplitude low-frequency oscillatory wind component can play a significant role, and the response may be quite different from that predicted by steady-state theory. We have also developed a fully numerical code to study the effects of unsteady wind and validate the theoretical predictions. This work is part of B. Druecke’s doctoral thesis (under preparation). Technical details are given in §3 of Sec. II below.

(iv) *Energy transfer to low-frequency gravity waves via resonant nonlinear interactions.* We have examined the radiation of low-frequency gravity waves by weakly nonlinear wavepackets propagating in a stratified fluid of variable buoyancy frequency. When wave trapping is possible as, for example, in the case of a density inversion, we find that the mean flow induced by nonlinear interactions can give rise to radiating gravity waves. This mechanism is analogous to the transfer of energy from instability wavepackets, generated by shear-flow instability, to low-frequency radiating gravity waves. This is work still in progress.

The main results of the present study are highlighted and discussed in connection with atmospheric gravity wave generation, in §4 of Sec. II.

- Personnel supported: Professor T. R. Akylas, B. Druecke (graduate research assistant)
- Publications

Akylas, T. R., Grimshaw, R. H. J., Clarke, S. R. & Tabaei, A., “Reflecting Tidal Wave Beams and Local Generation of Solitary Waves in the Ocean Thermocline”, *Journal of Fluid Mechanics*, **593**, 297-313 (2007)

Akylas, T. R. & Druecke, B. C., “The Effect of Rotation on Finite-Amplitude Mountain Gravity Waves”, *Physica D* (Special Volume on the 80th Birthday of Professor L. N. Howard), to be submitted.

Druecke, B. C., Skopovi, I. & Akylas, T. R., “Effects of Temporal Wind Variations on Mountain Gravity Waves”, *Theoretical and Computational Fluid Dynamics*, to be submitted.

Druecke, B. C. “The Effects of Rotation and Variable Wind in the Generation of Mountain Gravity Waves”, PhD Thesis, in preparation.

## II. TECHNICAL DESCRIPTION

### 1 Rotation Effects on Nonlinear Stratified Flow Over Topography

In the atmosphere, the typical value of the Brunt–Väisälä (buoyancy) frequency  $N \sim 10^{-2}$  rad/s and the wind speed  $U \sim 10 - 30$  m/s, so the characteristic vertical length-scale of mountain waves,  $U/N \sim 1 - 3$  km, is much shorter than the typical length of the topography,  $L \sim 10 - 100$  km; this justifies using the hydrostatic approximation, taking dispersive effects to be weak. The significance of rotation effects is controlled by the Rossby number  $Ro = U/(Lf)$ ,  $f$  being the Coriolis parameter, and  $f/N \sim 10^{-2}$  in the atmosphere. On scaling grounds, then, rotation would be expected to be relatively unimportant when  $Ro \gg 1$  and this regime is realized if the topography is not too long,  $L \leq 50$  km. Here we make a systematic study of gravity waves over topography in the limit  $Ro \gg 1$ , which reveals that weak rotation can have a significant effect in the far-field response. For simplicity, we first consider the case of  $N$  constant. The effects of the tropopause, which turn out to be crucial, are included in §2.

#### 1.1 Governing Equations

The governing equations for incompressible, inviscid, stratified flow in a rotating coordinate system are

$$\begin{aligned}\rho \left( \frac{Du}{Dt} + fw \right) &= -p_x \\ \rho \frac{Dv}{Dt} &= -p_y - g\rho \\ \rho \left( \frac{Dw}{Dt} - fu \right) &= -p_z \\ \nabla \cdot \mathbf{u} &= 0 \\ \frac{D\rho}{Dt} &= 0\end{aligned}\tag{1}$$

where  $f = 2\Omega \sin \theta$  is the Coriolis parameter,  $\Omega = 7.2722$  rad/sec being the angular speed of the earth's rotation and  $\theta$  the latitude. The Coriolis parameter ranges in value from  $f = 0 \text{ sec}^{-1}$  at the equator where rotation does not locally affect flows to  $f = \pm 1.4544 \times 10^{-4} \text{ sec}^{-1}$  at the poles where local rotation effects are maximum. The assumption that the thickness of the fluid is relatively small compared with the horizontal length scales has been made following Kundu and Cohen [12]. The coordinate system is chosen such that  $y$  is the outward-pointing normal to the earth's surface (vertical),  $x$  points in the eastward direction and  $z$  southward, as depicted in Fig. 1.

Assuming the flow is two-dimensional such that there is no variation in the  $z$ -direction, the velocity components in the streamwise and vertical directions can be written using the

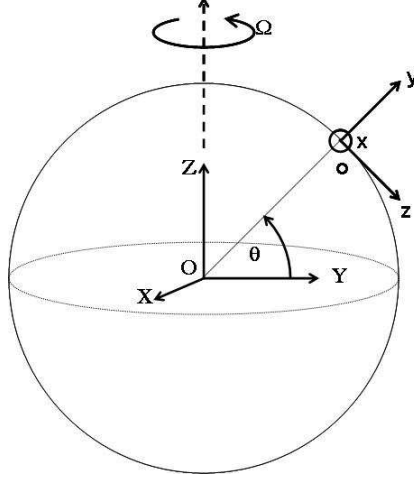


Figure 1: Local coordinate system  $xyz$  rotating about polar axis with frequency  $\Omega$ .

streamfunction,  $\Psi$ , as

$$\mathbf{u}(x, y, t) = (u, v, w) = (\Psi_y, -\Psi_x, w) \quad (2)$$

The governing equations then become

$$\begin{aligned} \rho_t + J(\rho, \Psi) &= 0 \\ \rho \{ \Psi_{yt} + J(\Psi_y, \Psi) + fw \} &= -p_x \\ \rho \{ -\Psi_{xt} - J(\Psi_x, \Psi) \} &= -p_y - g\rho \\ \rho \{ w_t + J(w, \Psi) - f\Psi_y \} &= -p_z \end{aligned} \quad (3)$$

where  $J(\phi, \eta) = \phi_x \eta_y - \phi_y \eta_x$  is the Jacobian. For inviscid flow, only the kinematic boundary condition can be imposed at the surface of the topography. For two-dimensional topography given by  $y = h(x)$  as depicted in Fig. 2, the kinematic boundary condition is

$$\mathbf{u} \cdot \hat{\mathbf{n}} = 0 \quad \text{on } y = h(x) \quad \Rightarrow \quad \frac{d\Psi}{dx} = 0 \quad \text{on } y = h(x) \quad \Rightarrow \quad \Psi = \text{const} \quad \text{on } y = h(x) \quad (4)$$

The assumption that disturbances do not propagate far upstream is made. Therefore, far upstream as  $x \rightarrow -\infty$ , the wind velocity is uniform giving  $\Psi \rightarrow U_0 y$  and there is no transverse velocity,  $w \rightarrow 0$ . The density field is unperturbed,  $\rho \rightarrow \bar{\rho}(y)$  and hydrostatic,  $\frac{d\bar{p}}{dy} = -g\bar{\rho}$ . Finally, the pressure gradient in the transverse direction is geostrophic, giving  $p_z = \rho f U_0$ .

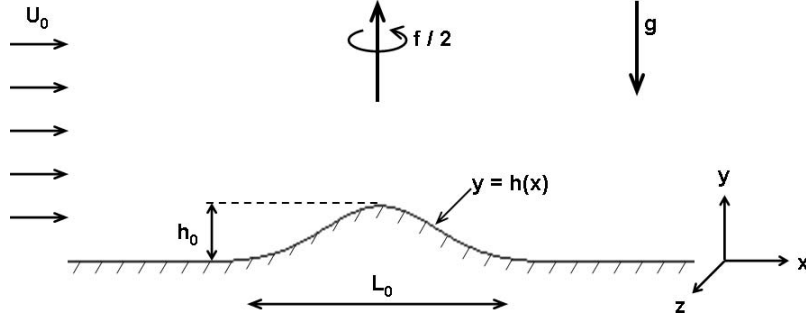


Figure 2: Physical system of stratified flow over topography in the presence of rotation.

### 1.1.1 Nondimensionalization

We nondimensionalize the variables as follows

$$\begin{aligned} x &= Lx', \quad y = \frac{U_0}{N_0}y', \quad t = \frac{L}{U_0}t' \\ \Psi &= \frac{U_0^2}{N_0}\Psi', \quad w = fLw', \quad \rho = \rho_0\rho', \quad p = g\rho_0\frac{U_0}{N_0}p' \end{aligned} \quad (5)$$

where  $L$  is the characteristic width of the mountain,  $U_0$  the characteristic wind velocity,  $N_0$  the characteristic Brunt–Väisälä frequency and  $\rho_0$  the characteristic density. Substituting these into the governing equations of (3) and dropping the primes gives

$$\begin{aligned} \rho_t + J(\rho, \Psi) &= 0 \\ \beta\rho \left\{ \Psi_{yt} + J(\Psi_y, \Psi) + \frac{1}{Ro^2}w \right\} &= -p_x \\ \beta\mu^2\rho \{ \Psi_{xt} + J(\Psi_x, \Psi) \} &= p_y + \rho \\ \rho \{ w_t + J(w, \Psi) - \Psi_y \} &= -\rho \end{aligned} \quad (6)$$

where the dimensionless parameters are the Boussinesq parameter,  $\beta = \frac{U_0 N_0}{g}$ , the longwave parameter  $\mu = \frac{U_0}{N_0 L}$  and the Rossby number  $Ro = \frac{U_0}{fL}$ . The Boussinesq parameter is the ratio of the vertical length scale of fluid motion to the vertical length scale over which density changes, and the limit as  $\beta \rightarrow 0$  gives the Boussinesq approximation. The longwave parameter is the ratio of vertical to horizontal length scales, and the limit as  $\mu \rightarrow 0$  gives the hydrostatic approximation. The Rossby number is the ratio of the Coriolis time scale to the advective time scale. Thus in the limit as  $Ro \rightarrow \infty$ , rotational effects are relatively unimportant. The limit where  $Ro = 1$  is the limit where both rotation and advection are of equal importance, and as  $Ro \rightarrow 0$ , rotation dominates.

Far upstream the flow is undisturbed, and the nondimensionalized flow is

$$\Psi \rightarrow y, \quad w \rightarrow 0, \quad \bar{\rho}_y = -\beta\bar{\rho}N^2 \quad (x \rightarrow -\infty) \quad (7)$$

The nondimensionalized boundary condition on the topography becomes

$$\Psi = \text{const on } y = \epsilon h(x) \quad (8)$$

where  $\epsilon = \frac{h_0 N_0}{U_0}$  is a parameter determining the importance of nonlinearity and  $h_0$  is the characteristic height of the topography. The nondimensional topographic profile used in the analyses summarized below is either the Gaussian profile of functional form

$$h(x) = e^{-x^2} \quad (9)$$

or the algebraic (Witch of Agnesi) profile

$$h(x) = \frac{1}{1+x^2} \quad (10)$$

The flow is assumed to be hydrostatic, implying  $\mu \rightarrow 0$ , and nearly steady. We define a slow time

$$T = \nu^2 t, \quad \nu \ll 1 \quad (11)$$

Then the time derivatives in the governing equations can be rescaled and the hydrostatic approximation imposed to give

$$\begin{aligned} J(\rho, \Psi) &= -\nu^2 \rho_T \\ \beta \rho \left\{ \nu^2 \Psi_{yT} + J(\Psi_y, \Psi) + \frac{1}{Ro^2} w \right\} &= -p_x \\ p_y &= -\rho \end{aligned} \quad (12)$$

$$\rho \left\{ \nu^2 w_T + J(w, \Psi) - \Psi_y \right\} = -\rho$$

Differentiating the second equation with respect to  $y$  and eliminating pressure in favor of density using the third equation gives

$$\begin{aligned} J(\rho, \Psi) &= -\nu^2 \rho_T \\ \beta \left\{ \rho \left[ \nu^2 \Psi_{yT} + J(\Psi_y, \Psi) + \frac{1}{Ro^2} w \right] \right\}_y &= \rho_x \\ p_y &= -\rho \end{aligned} \quad (13)$$

$$J(w, \Psi) = \Psi_y - (1 + \nu^2 w_T)$$

### 1.1.2 Integration of Density Equation

Making the assumption that the streamlines never become vertical,  $\Psi_y \neq 0$ , throughout the domain, one can make the coordinate transformation

$$(x, y, T) \rightarrow (x, \Psi, T). \quad (14)$$

Then substituting this into the density equation above gives

$$\Psi_y \rho_x|_\Psi = -\nu^2 \rho_T \quad (15)$$

Dividing through by  $\Psi_y$  and integrating with respect to  $x$  along contours of constant streamfunction (streamlines) gives

$$\rho = F(\Psi, T) - \nu^2 \int_{-\infty}^x \frac{\rho_T}{\Psi_y} \Big|_\Psi dx' \quad (16)$$

where  $F(\Psi, T)$  is a constant of integration. The density profile far upstream as  $x \rightarrow -\infty$  is  $\rho \rightarrow \bar{\rho}(y) = \bar{\rho}(\Psi)$ . Therefore  $F(\Psi, T) = \bar{\rho}(\Psi)$  and

$$\rho(x, \Psi, T) = \bar{\rho}(\Psi) - \nu^2 \int_{-\infty}^x \frac{\rho_T}{\Psi_y} \Big|_\Psi dx' \quad (17)$$

This implies that  $\rho(x, y, T) = \rho(x, \Psi)$  and  $\rho_T = \rho_\Psi \Psi_T = \bar{\rho}_\Psi \Psi_T + \mathcal{O}(\nu^2)$ . Finally, combining everything gives

$$\rho = \bar{\rho}(\Psi) - \nu^2 \bar{\rho}_\Psi(\Psi) \int_{-\infty}^x \frac{\Psi_T}{\Psi_y} \Big|_\Psi dx' + \mathcal{O}(\nu^4) \quad (18)$$

### 1.1.3 Integration of In-Plane Momentum Equation

We next integrate the second equation in (13). Taking the  $y$ -derivative of the left-hand-side gives

$$\rho J(\Psi_{yy}, \Psi) + \rho_\Psi \Psi_y J(\Psi_y, \Psi) - \frac{1}{\beta} \rho_x|_\Psi - \frac{1}{\beta} \rho_\Psi \Psi_x = -\nu^2 (\rho \Psi_{yT})_y - \frac{1}{Ro^2} (\rho w)_y \quad (19)$$

In order to simplify notation, we define

$$S \equiv \rho \Psi_{yy} + \rho_\Psi \left( \frac{1}{2} \Psi_y^2 + \frac{y}{\beta} \right) \quad (20)$$

Then

$$\begin{aligned} J(S, \Psi) &\equiv S_x \Psi_y - S_y \Psi_x \\ &= \rho J(\Psi_{yy}, \Psi) + \rho_\Psi J\left(\frac{1}{2} \Psi_y^2 + \frac{y}{\beta}, \Psi\right) + \rho_x|_\Psi \Psi_y \Psi_{yy} + \rho_{x\Psi}|_\Psi \left(\frac{1}{2} \Psi_y^2 + \frac{y}{\beta}\right) \Psi_y \end{aligned} \quad (21)$$



and the momentum equation can be written as

$$J(S, \Psi) = \left\{ \rho_x|_{\Psi} \left( \frac{1}{2} \Psi_y^2 + \frac{y}{\beta} \right) \right\}_y - \nu^2 (\rho \Psi_{yT})_y - \frac{1}{Ro^2} (\rho w)_y \quad (22)$$

We next make the Boussinesq approximation, which can be written formally as the limit in which the Boussinesq parameter,  $\beta$ , approaches zero. Physically this means that the vertical displacement of fluid particles is small compared with the vertical length scale over which the density changes are significant. In the Boussinesq approximation, the vertical variation of density scales as the Boussinesq parameter

$$\rho_y = \rho_{\Psi} \Psi_y = \mathcal{O}(\beta) \quad (23)$$

and the horizontal variation of density along a streamline can be written using (15) as

$$\rho_x|_{\Psi} = -\nu^2 \frac{\rho_T}{\Psi_y} = -\nu^2 \frac{\rho_{\Psi} \Psi_T}{\Psi_y} = -\nu^2 \bar{\rho}_{\Psi} \frac{\Psi_T}{\Psi_y} + \mathcal{O}(\nu^4) = \nu^2 \beta \bar{\rho}(\Psi) N^2(\Psi) \frac{\Psi_T}{\Psi_y} + \mathcal{O}(\nu^4) \quad (24)$$

Then the momentum equation becomes

$$J(S, \Psi) = \nu^2 \bar{\rho}(\Psi) N^2(\Psi) \left( \frac{\Psi_T}{\Psi_y} y \right)_y - \nu^2 \bar{\rho}(\Psi) \Psi_{yyT} - \frac{1}{Ro^2} \bar{\rho}(\Psi) w_y \quad (25)$$

Defining

$$R \equiv \bar{\rho}(\Psi) \left\{ \Psi_{yyT} - N^2(\Psi) \left( y \frac{\Psi_T}{\Psi_y} \right)_y \right\}$$

the momentum equation can be written as

$$J(S, \Psi) = -\nu^2 R - \frac{\bar{\rho}(\Psi)}{Ro^2} w_y \quad (26)$$

As in the integration of the density equation, we again make the transformation  $(x, y, T) \rightarrow (x, \Psi, T)$  and assume the streamlines are not vertical throughout the domain ( $\Psi_y \neq 0$ ). Then the momentum equation can be written

$$S_x|_{\Psi} \Psi_y = -\nu^2 R - \frac{\bar{\rho}(\Psi)}{Ro^2} w_y \quad (27)$$

and integrated along streamlines to give

$$S = G(\Psi, T) - \nu^2 \int_{-\infty}^x \frac{R}{\Psi_y|_{\Psi}} dx' - \frac{1}{Ro^2} \int_{-\infty}^x \bar{\rho}(\Psi) \frac{w_y}{\Psi_y|_{\Psi}} dx' \quad (28)$$

The constant of integration,  $G(\Psi, T)$ , is determined by the behavior of the flow far upstream as  $x \rightarrow -\infty$ . Far upstream,

$$S \rightarrow -\bar{\rho}(\Psi) N^2(\Psi) \Psi \text{ as } x \rightarrow -\infty \Rightarrow G(\Psi) = -\bar{\rho}(\Psi) N^2(\Psi) \Psi$$

and the solution to the momentum equation is

$$S = -\bar{\rho}(\Psi) N^2(\Psi) \Psi - \nu^2 \int_{-\infty}^x \frac{R}{\Psi_y} \Big|_{\Psi} dx' - \frac{1}{Ro^2} \int_{-\infty}^x \bar{\rho}(\Psi) \frac{w_y}{\Psi_y} \Big|_{\Psi} dx' \quad (29)$$

Substituting the definition of  $S$  given in (20) and utilizing the Boussinesq approximation gives

$$\Psi_{yy} + N^2(\Psi) (\Psi - y) = -\frac{1}{Ro^2} \int_{-\infty}^x \frac{w_y}{\Psi_y} \Big|_{\Psi} dx' + \nu^2 H + \mathcal{O}(\nu^4) \quad (30)$$

where

$$H \equiv -\frac{\partial}{\partial \Psi} \int_{-\infty}^x \Psi_{yT} \Big|_{\Psi} dx' + N^2(\Psi) \frac{\partial}{\partial \Psi} \int_{-\infty}^x y \frac{\Psi_T}{\Psi_y} \Big|_{\Psi} dx' - y N^2(\Psi) \frac{\partial}{\partial \Psi} \int_{-\infty}^x \frac{\Psi_T}{\Psi_y} \Big|_{\Psi} dx'$$

We rewrite the first term on the right-hand-side of (30) to give

$$\Psi_{yy} + N^2(\Psi) (\Psi - y) = -\frac{1}{Ro^2} \frac{\partial}{\partial \Psi} \int_{-\infty}^x w \Big|_{\Psi} dx' + \nu^2 H + \mathcal{O}(\nu^4) \quad (31)$$

#### 1.1.4 Integration of Transverse (Spanwise) Momentum Equation

We finally integrate the equation governing momentum in the  $z$ -direction, given by the fourth equation in (13). Using the same coordinate transformation as above, again assuming  $\Psi \neq 0$  everywhere, we rewrite this equation as

$$w_x \Big|_{\Psi} \Psi_y = \Psi_y - 1 - \nu^2 w_T \quad (32)$$

and integrate to obtain

$$w = \int_{-\infty}^x \frac{\Psi_y - 1}{\Psi_y} \Big|_{\Psi} dx' - \nu^2 \int_{-\infty}^x \frac{w_T}{\Psi_y} \Big|_{\Psi} dx' \quad (33)$$

where the constant of integration has been set to zero because  $w \rightarrow 0$  as  $x \rightarrow -\infty$ . The first term can be rewritten to give

$$w = \frac{\partial}{\partial \Psi} \int_{-\infty}^x (\Psi - y) \Big|_{\Psi} dx' - \nu^2 \int_{-\infty}^x \frac{w_T}{\Psi_y} \Big|_{\Psi} dx' \quad (34)$$

For the remainder of the report, we shall focus on the results in the limit of steady flow over topography. The governing equations for steady flow are

$\rho = \bar{\rho}(\Psi)$ $\Psi_{yy} + N^2(\Psi) (\Psi - y) = -\frac{1}{Ro^2} \frac{\partial}{\partial \Psi} \int_{-\infty}^x w \Big _{\Psi} dx' \quad (35)$ $w = \frac{\partial}{\partial \Psi} \int_{-\infty}^x (\Psi - y) \Big _{\Psi} dx'$
--

subject to the boundary condition along the topography

$$\Psi = 0 \text{ on } y = \epsilon h(x) \quad (36)$$

and the radiation condition as  $y \rightarrow \infty$  ensuring energy propagates outward away from the topography.

## 1.2 Linear Solution for Uniformly Stratified Flow

In the limit when the topography amplitude is small,  $\epsilon \ll 1$ , the governing equations become linear because the streamline displacement,  $\eta \equiv y - \Psi \sim \epsilon$  scales with  $\epsilon$ . Thus derivatives with respect to the streamfunction can be rewritten as derivatives with respect to  $y$  and the linearized equations become

$$\begin{aligned} \Psi_{yy} + N^2(y)(\Psi - y) &= -\frac{1}{Ro^2} \frac{\partial}{\partial y} \int_{-\infty}^x w dx \\ w &= \frac{\partial}{\partial y} \int_{-\infty}^x (\Psi - y) dx' \end{aligned} \quad (37)$$

Defining the streamfunction perturbation,  $\psi$ , as

$$\psi \equiv \Psi - y \quad (38)$$

and combining equations gives

$$\psi_{yy} + N^2(y)\psi = -\frac{1}{Ro^2} \frac{\partial^2}{\partial y^2} \int_{-\infty}^x \int_{-\infty}^{x'} \psi dx'' dx' \quad (39)$$

Taking two derivatives with respect to  $x$  gives

$$\left( \psi_{yy} + N^2(y)\psi \right)_{xx} + \frac{1}{Ro^2} \psi_{yy} = 0 \quad (40)$$

subject to the linearized boundary condition

$$\psi = -\epsilon h(x) \text{ on } y = 0 \quad (41)$$

Defining the Fourier transform in the horizontal and its inverse as

$$\begin{aligned} \hat{f}(k) &= \mathcal{F}\{f(x)\} = \frac{1}{2\pi} \int_{-\infty}^{\infty} f(x) e^{-ikx} dx \\ f(x) &= \mathcal{F}^{-1}\{\hat{f}(k)\} = \int_{-\infty}^{\infty} \hat{f}(k) e^{ikx} dk \end{aligned} \quad (42)$$

the transformed differential equation becomes

$$(k^2 - \beta^2) \hat{\psi}_{yy} + k^2 N^2(y) \hat{\psi} = 0 \quad (43)$$

subject to the boundary condition

$$\hat{\psi} = -\epsilon \hat{h}(k) \text{ on } y = 0 \quad (44)$$

and the radiation condition as  $y \rightarrow \infty$ , where  $\beta \equiv \frac{1}{Ro}$ . The general solution is

$$\psi = 2\Re \left\{ \int_0^\infty a(k) \exp \left( i \frac{k}{\sqrt{k^2 - \beta^2}} y \right) e^{ikx} dx + \int_0^\infty b(k) \exp \left( -i \frac{k}{\sqrt{k^2 - \beta^2}} y \right) e^{ikx} dx \right\} \quad (45)$$

In general, the radiation condition requires disturbances to radiate outward from their source as time increases. Here the disturbances must radiate upward away from the topography. The radiation condition can be formulated by requiring the vertical component of group velocity to be positive. The linear dispersion relation is

$$\omega = k - \frac{\text{sgn } k}{|m|} \sqrt{k^2 + \beta^2 m^2} \quad (46)$$

and the vertical component of the group velocity is

$$c_g|_y = \frac{\partial \omega}{\partial m} = \frac{\text{sgn } (km) k^2}{m^2 \sqrt{k^2 + \beta^2 m^2}} \quad (47)$$

Therefore the radiation condition requires the signs of the vertical and horizontal wavenumbers to be the same.

$$c_g|_y > 0 \Rightarrow \text{sgn } (km) > 0$$

In addition, the solution must be bounded as  $y \rightarrow \infty$ , which requires  $b(k) = 0$  when  $|k| < \beta$ . Applying the radiation condition and boundedness in conjunction with the boundary condition at  $y = 0$  given by (44) yields the solution

$$\psi(x, y) = -2\epsilon \Re \left\{ \int_0^\beta \exp \left( \frac{-ky}{\sqrt{\beta^2 - k^2}} \right) \hat{h}(k) e^{ikx} dk + \int_\beta^\infty \exp \left( \frac{iky}{\sqrt{k^2 - \beta^2}} \right) \hat{h}(k) e^{ikx} dk \right\} \quad (48)$$

The equation governing the spanwise velocity in the linear limit is  $w_x = \psi_y$  and in Fourier space  $\hat{w} = -i \frac{\hat{\psi}_y}{k}$ . Using the solution for the streamfunction given in (48) gives the solution for the spanwise velocity as

$$w(x, y) = -2\epsilon \Re \left\{ \int_0^\beta \frac{i \hat{h}(k) e^{ikx}}{\sqrt{\beta^2 - k^2}} \exp \left( \frac{-ky}{\sqrt{\beta^2 - k^2}} \right) dk + \int_\beta^\infty \frac{\hat{h}(k) e^{ikx}}{\sqrt{k^2 - \beta^2}} \exp \left( \frac{iky}{\sqrt{k^2 - \beta^2}} \right) dk \right\} \quad (49)$$

In both (48) and (49) the integral over wavenumbers  $0 < k < \beta$  is evanescent in the vertical and is the contribution dominated by rotation. The integrals for wavenumber  $k > \beta$  are oscillatory in the vertical. These are the relatively short wavelengths for which rotation is negligible.

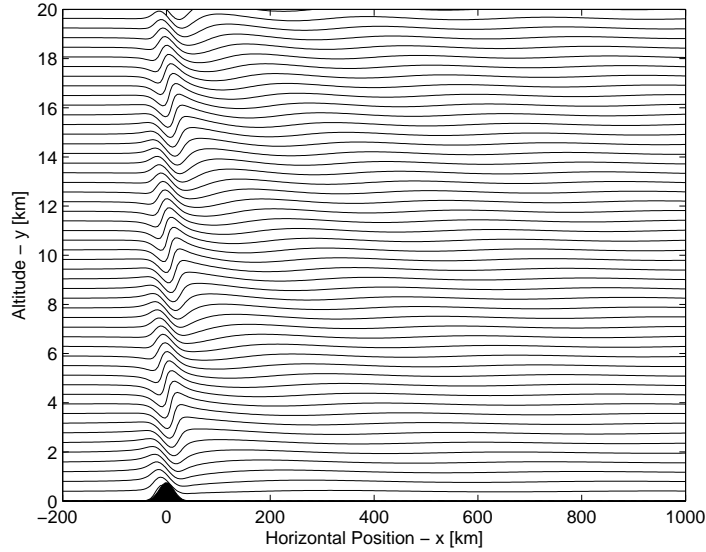


Figure 3: Streamlines for linear solution of stratified flow over topography in the presence of rotation for  $Ro = 5$ . The values of the Coriolis parameter, Brunt-Väisälä frequency, freestream velocity, mountain width and mountain height for this simulation were  $f = 1.0 \times 10^{-4} \text{ sec}^{-1}$ ,  $N_0 = 1.0 \times 10^{-2} \text{ sec}^{-1}$ ,  $U_0 = 10 \text{ m/s}$ ,  $L_0 = 20 \text{ km}$  and  $h_0 = 0.75 \text{ km}$ , respectively. The topography shape is Gaussian (9).

Figures 3 and 4 show representative solutions for the linear streamlines and spanwise velocity, respectively. The solutions shown are for a Rossby number of 5 ( $\beta = \frac{1}{5}$ ). The streamlines near  $x = 0$  above the topography are dominated by stratification effects, whereas further downstream of the topography the effect of rotation is evident in the longer wavelength inertial-gravity waves. The spanwise velocity is a purely rotational effect which is not present in the limit as  $Ro \rightarrow \infty$ . Note that the first streamline in Figure 3 does not coincide with the topography because the linear boundary condition has been applied.

### 1.3 Inner Nonlinear Solution and Lack of Uniform Validity

While the above solution accounts for rotation, it neglects the effect of nonlinearity. In order to incorporate nonlinearity, we return to the original governing equations of (35). In the case of weak rotation, the Rossby number is large and right-hand-side of the second equation in (35) is a small correction. As a first approximation, we follow Smith [21] and examine the solution to the nonlinear problem with weak rotation using a naive perturbation expansion of the form

$$\Psi = \Psi^{(0)} + \beta^2 \Psi^{(1)} + \beta^4 \Psi^{(2)} + \dots \quad (50)$$

Then the leading order equation is

$$\Psi_{yy}^{(0)} + \Psi^{(0)} - y = 0 \quad (51)$$

subject to

$$\Psi^{(0)} = 0 \text{ on } y = \epsilon h(x) \quad (52)$$

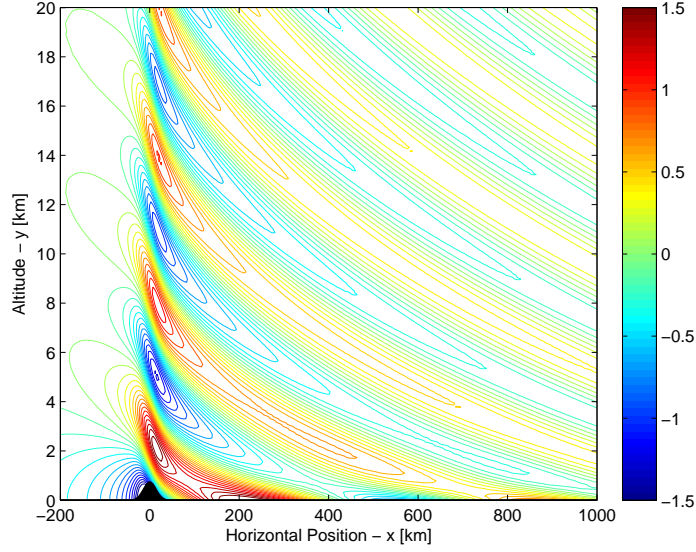


Figure 4: Spanwise velocity,  $w$  [m/s], for linear solution of stratified flow over topography in the presence of rotation as given in (49) for  $Ro = 5$ . The parameters are the same as those for Figure 3.

and the radiation condition as  $y \rightarrow \infty$ . This is the classic Long's problem [14] in which the nonlinear governing equations are reduced to a linear equation with nonlinear boundary condition. The solution can be written by decomposing the streamfunction as above into its undisturbed component,  $y$ , and a streamfunction disturbance,  $\psi$ .

$$\Psi^{(0)} = y + \psi^{(0)} \quad (53)$$

Then the solution becomes

$$\psi^{(0)} = 2(a(x) \cos y - b(x) \sin y) \quad (54)$$

The radiation condition requires

$$\hat{b}(k) = -i \operatorname{sgn} k \hat{a}(k) \Rightarrow b = -\mathcal{H}\{a\} \quad (55)$$

where  $\mathcal{H}\{a\}$  is the Hilbert transform of  $a(x)$ . Finally, the boundary condition requires

$$a(x) \cos(\epsilon h) + \mathcal{H}\{a\} \sin(\epsilon h) = -\frac{1}{2} \epsilon h(x) \quad (56)$$

which must be solved for  $a(x)$ .

The leading order equation for the spanwise velocity is

$$w^{(0)} = C(\Psi) + \frac{\partial}{\partial \Psi^{(0)}} \int_0^x (\Psi^{(0)} - y) \Big|_{\Psi^{(0)}} dx' \quad (57)$$

where the integral is evaluated along the contours of constant  $\Psi^{(0)}$ . Substituting the leading order solution for  $\Psi^{(0)}$  gives

$$w^{(0)} = C(\Psi) + 2 \frac{\partial}{\partial \Psi^{(0)}} \int_0^x [a(x') \cos y - b(x') \sin y] |_{\Psi^{(0)}} dx' \quad (58)$$

We wish to examine the asymptotic behavior of the solution for the streamfunction and spanwise velocity in the limit as  $x \rightarrow \pm\infty$ . In order for the Fourier transform of the topography to converge in the linear solution, it is necessary that  $h(x) = o\left(\frac{1}{x}\right)$  as  $x \rightarrow \pm\infty$ . In this limit when  $x$  is large, the amplitude is small and the solution is linear. Thus we have

$$\left. \begin{aligned} a &\sim -\frac{\epsilon}{2} h(x) = o\left(\frac{1}{x}\right) \\ b = -\mathcal{H}\{a\} &= -i \int_0^\infty \hat{a}(k) e^{ikx} dk + c.c. \sim \frac{2}{x} \hat{a}(0) = \frac{1}{\pi x} \int_{-\infty}^\infty a(x') dx' \end{aligned} \right\} \text{ as } x \rightarrow \pm\infty \quad (59)$$

Since  $a(x) \ll b(x)$  as  $x \rightarrow \pm\infty$ , the behavior of the leading-order streamfunction solution as  $x \rightarrow \pm\infty$  is

$$\Psi^{(0)} \sim y - \frac{4}{x} \hat{a}(0) \sin y \text{ as } x \rightarrow \pm\infty \quad (60)$$

which decays to the undisturbed solution,  $\Psi = y$ , as  $x \rightarrow \pm\infty$ . In the limit as  $x \rightarrow \pm\infty$ , the spanwise solution behaves as

$$w^{(0)} \sim 2 \frac{\partial}{\partial y} \int_0^\infty \frac{-2}{x} \hat{a}(0) \sin y dx' + C(\Psi^0) \sim -4 \hat{a}(0) \ln |x| \cos y \text{ as } x \rightarrow \pm\infty \quad (61)$$

Thus the spanwise velocity diverges logarithmically far from the topography, and the naive perturbation solution of (50) is not uniformly valid, which agrees with the findings of Smith [21]. As Smith suggests, there are really two horizontal length scales present. The first is the width of the mountain used above, and the second is the length over which rotational effects act, and is  $L_{rot} \sim \frac{U_0}{f}$ . The procedure of matched asymptotic expansions can be used to account for these two distinct length scales and the logarithmic divergence of the spanwise velocity. In this matching, the domain is divided into an inner solution for  $x \rightarrow 0$  and an outer solution as  $|x| \rightarrow \infty$ . The above naive perturbation solution represents the first approximation for the inner solution, for which rotation is a weak perturbation. Far from the topography as length scales become large and Coriolis acceleration has sufficient time to act, rotation is of leading order importance. However, assuming the topography decays as  $h = o\left(\frac{1}{x}\right)$ , the disturbances far from  $x = 0$  are small and the solution becomes linear, allowing the application of the linear boundary condition and superposition. Figure (5) shows the effect of rotation in the linear limit. Near the topography, the solutions with and without rotation are nearly identical. Rotational effects become important further downstream. This provides a justification for the approach of matched asymptotic expansion, wherein rotation is weak in the inner solution and is of leading order importance in the outer solution.

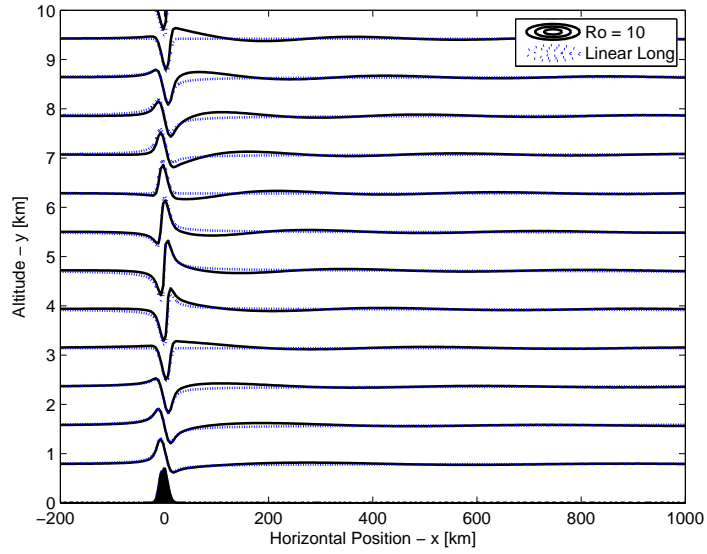


Figure 5: A comparison of streamlines showing the effect of rotation for the linear solution. Downstream of the topography rotational effects become more important as the Coriolis force has more time to act. Far downstream the inertia-gravity waves decay as energy is radiated upward. The values of the Coriolis parameter, Brunt-Väisälä frequency, freestream velocity, mountain width and mountain height for  $Ro = 10$  were  $f = 1.0 \times 10^{-4} \text{ sec}^{-1}$ ,  $N_0 = 1.0 \times 10^{-2} \text{ sec}^{-1}$ ,  $U_0 = 10 \text{ m/s}$ ,  $L_0 = 10 \text{ km}$  and  $h_0 = 0.75 \text{ km}$ , respectively. For the linear limit of Long's solution the parameter values were the same, with the exception that the Coriolis parameter was set to zero. The topography shape is Gaussian (9).



#### 1.4 Outer Solution

Far from the center of the topography, the solution is linear and the governing equations are given by (40) and (1.2) subject to the boundary condition given in (41). In order to account for the leading-order importance of rotation, the horizontal coordinate and wavenumber should be scaled by  $\beta$  as

$$\tilde{x} = \beta x, \quad \tilde{k} = \frac{1}{\beta} k \quad (62)$$

and the streamfunction and velocity variables as

$$\psi = \beta \tilde{\psi}, \quad u = 1 + \beta \tilde{u}, \quad v = \beta^2 \tilde{v}, \quad w = \tilde{w} \quad (63)$$

where  $\tilde{u} = \tilde{\psi}_y$  and  $\tilde{v} = -\tilde{\psi}_{\tilde{x}}$ . Then the governing equations become

$$\begin{aligned} (\tilde{\psi}_{yy} + N^2 \tilde{\psi})_{\tilde{x}\tilde{x}} + \tilde{\psi}_{yy} &= 0 \\ \tilde{w}_{\tilde{x}} &= \tilde{\psi}_y \end{aligned} \quad (64)$$

Far from the topography in the stretched coordinate,  $\tilde{x}$ , the topography appears to be a Dirac  $\delta$ -distribution. Then the linearized boundary condition along  $y = 0$  in this outer region can be written as

$$\psi = \beta \tilde{\psi} = -2\pi\epsilon\hat{h}(0) \delta(\tilde{x}) \quad \text{on } y = 0 \quad (65)$$

where the factor  $2\pi\epsilon\hat{h}(0)$  is the area under the topography curve. Then the solution to these is found via Fourier transforms to be

$$\begin{aligned} \tilde{\psi} &= -2\epsilon\hat{h}(0) (I_1 + I_2) \\ \tilde{w} &= -2\epsilon\hat{h}(0) (I_3 + I_4) \end{aligned} \quad (66)$$

where

$$\begin{aligned} I_1 &\equiv \Re \left\{ \int_0^1 \exp \left( \frac{-\tilde{k}y}{\sqrt{1-\tilde{k}^2}} \right) e^{i\tilde{k}\tilde{x}} d\tilde{k} \right\} \\ I_2 &\equiv \Re \left\{ \int_1^\infty \exp \left( \frac{i\tilde{k}y}{\sqrt{\tilde{k}^2-1}} \right) e^{i\tilde{k}\tilde{x}} d\tilde{k} \right\} \\ I_3 &\equiv \Re \left\{ \int_0^1 \frac{ie^{i\tilde{k}\tilde{x}}}{\sqrt{1-\tilde{k}^2}} \exp \left( \frac{-\tilde{k}y}{\sqrt{1-\tilde{k}^2}} \right) d\tilde{k} \right\} \\ I_4 &\equiv \Re \left\{ \int_1^\infty \frac{e^{i\tilde{k}\tilde{x}}}{\sqrt{\tilde{k}^2-1}} \exp \left( \frac{i\tilde{k}y}{\sqrt{\tilde{k}^2-1}} \right) d\tilde{k} \right\} \end{aligned} \quad (67)$$

In order to match this solution with the inner solution near the topography, it is necessary to examine (66) in the limit as  $\tilde{x} \rightarrow 0$ . The limit of this outer solution as  $\tilde{x} \rightarrow 0$  is

$$\left. \begin{aligned} \tilde{\psi} &\sim 2\epsilon\hat{h}(0) \frac{\sin y}{\tilde{x}} \\ \tilde{u} &\sim 2\epsilon\hat{h}(0) \frac{\cos y}{\tilde{x}} \\ \tilde{v} &\sim 2\epsilon\hat{h}(0) \frac{\sin y}{\tilde{x}^2} \\ \tilde{w} &\sim 2\epsilon\hat{h}(0) \cos y \ln |\tilde{x}| + \pi\epsilon\hat{h}(0) \sin y \operatorname{sgn} \tilde{x} \end{aligned} \right\} (\tilde{x} \rightarrow 0) \quad (68)$$

$$\tilde{w}|_{\tilde{x} \rightarrow 0^-}^{\tilde{x} \rightarrow 0^+} = 2\pi\epsilon\hat{h}(0) \sin y$$

The details of the evaluation of these limits is found in Appendix A.

### 1.5 Matching

In order to match the inner and outer solutions, one must return to the inner solution and evaluate its limit as  $x \rightarrow \infty$  more precisely. The inner solution for the streamfunction disturbance was given in (54). Since the integrals involved in evaluating  $w$  are along contours of constant streamfunction, it is useful to rewrite the solution in terms of harmonic functions of streamfunction,  $\Psi$ , as

$$\psi^{(0)} = \Psi^{(0)} - y = 2 \left[ a(x) \cos \Psi^{(0)} - b(x) \sin \Psi^{(0)} \right] + \sum_{n=1}^{\infty} r_n \sin n\Psi^{(0)} + s_n \cos n\Psi^{(0)} \quad (69)$$

where  $r_n$  and  $s_n$  are coefficients arising from nonlinearity and can be determined analytically by expanding

$$\psi^{(0)} = 2(a \cos y - b \sin y) = 2 \left[ a(x) \cos \Psi^{(0)} - b(x) \sin \Psi^{(0)} \right] + \sum_{n=1}^{\infty} r_n \sin n\Psi^{(0)} + s_n \cos n\Psi^{(0)}$$

The first few terms can be shown by hand to be

$$\begin{aligned} r_1 &= b(a^2 + b^2), & s_1 &= -a(a^2 + b^2) \\ r_2 &= 2(a^2 - b^2), & s_2 &= 4ab \\ r_3 &= 3b(3a^2 - b^2), & s_3 &= 3a(3b^2 - a^2) \end{aligned}$$

Substituting the above expansion into the leading order equation for the spanwise velocity given in (57), the spanwise velocity is

$$\begin{aligned}
w^{(0)}(x, \Psi^{(0)}) &= C(\Psi^{(0)}) - 2 \left[ \sin \Psi^{(0)} \int_0^x a(x') dx' + \cos \Psi^{(0)} \int_0^x b(x') dx' \right] \\
&+ \sum_{n=1}^{\infty} n \left[ \cos n \Psi^{(0)} \int_0^x r_n(x') dx' - \sin n \Psi^{(0)} \int_0^x s_n(x') dx' \right]
\end{aligned} \tag{70}$$

Then the jump in spanwise velocity across the inner solution is found to be

$$w^{(0)} \Big|_{-\infty}^{\infty} = -4\pi \hat{a}(0) \sin \Psi^{(0)} + 2\pi \sum_{n=1}^{\infty} n \left( \hat{r}_n(0) \cos n \Psi^{(0)} - \hat{s}_n(0) \sin n \Psi^{(0)} \right) \tag{71}$$

Details of this computation are found in Appendix B.

In summary, we have thus far obtained an inner solution of

$$\begin{aligned}
\psi^{(0)} &= 2 \left( a \cos \Psi^{(0)} - b \sin \Psi^{(0)} \right) + \sum_{n=1}^{\infty} \left( r_n \sin n \Psi^{(0)} + s_n \cos n \Psi^{(0)} \right) \\
w^{(0)} &= -2 \left[ \sin \Psi^{(0)} \int_0^x a(x') dx' + \cos \Psi^{(0)} \int_0^x b(x') dx' \right] \\
&+ \sum_{n=1}^{\infty} n \left[ \cos n \Psi^{(0)} \int_0^x r_n(x') dx' - \sin n \Psi^{(0)} \int_0^x s_n(x') dx' \right] + C(\Psi^{(0)})
\end{aligned}$$

with asymptotic behavior

$$\left. \begin{aligned} \psi^{(0)} &\sim -4\hat{a}(0) \frac{\sin y}{x} \\ w^{(0)} &\sim -4\hat{a}(0) \cos y \ln |x| + C(\Psi^{(0)}) \end{aligned} \right\}, |x| \rightarrow \infty$$

$$w^{(0)} \Big|_{-\infty}^{\infty} = -4\pi \hat{a}(0) \sin y + 2\pi \sum_{n=1}^{\infty} n [\hat{r}_n(0) \cos ny - \hat{s}_n(0) \sin ny]$$

and an outer solution of

$$\begin{aligned}
\tilde{\psi} &= -2\epsilon \hat{h}(0) \Re \{I_1 + I_2\} \\
\tilde{w} &= -2\epsilon \hat{h}(0) \Re \{I_3 + I_4\}
\end{aligned}$$

with asymptotic behavior

$$\left. \begin{aligned} \tilde{\psi} &\sim 2\epsilon\hat{h}(0)\frac{\sin y}{\tilde{x}} \\ \tilde{w} &\sim 2\epsilon\hat{h}(0)\cos y\ln|\tilde{x}| - \frac{\pi}{2}\operatorname{sgn}\tilde{x}\sin y \end{aligned} \right\}, \tilde{x} \rightarrow 0$$

$$\tilde{w}|_{0-}^{0+} = 2\pi\epsilon\hat{h}(0)\sin y$$

At present, the inner and outer solutions do not match. Thus it is necessary to superimpose a second linear solution in the outer domain upon the current outer solution in order to satisfy the matching conditions as  $\tilde{x} \rightarrow 0$ . The derivation is found in Appendix C and the result is

$$\begin{aligned} \tilde{\psi} &= \left[ 4\hat{a}(0) - \sum_{n=2}^{\infty} \hat{s}_n(0) \right] \Re\{I_1 + I_2\} + \sum_{n=2}^{\infty} \Phi_{\tilde{x}}^{(n)} \\ \tilde{w} &= \left[ 4\hat{a}(0) - \sum_{n=2}^{\infty} \hat{s}_n(0) \right] \Re\{I_3 + I_4\} + \sum_{n=2}^{\infty} \Phi_y^{(n)} \end{aligned} \quad (72)$$

where

$$\Phi^{(n)} = -2\pi \cos k_n \tilde{x} [\hat{r}_n(0) \sin ny + \hat{s}_n(0) \cos ny] H(\tilde{x}) + 2\hat{s}_n(0) (I_5^{(n)} + I_6^{(n)}), \quad n > 1 \quad (73)$$

where

$$\begin{aligned} I_5^{(n)} &\equiv \Im \left\{ \int_0^1 \frac{ke^{ik\tilde{x}}}{k^2 - k_n^2} \exp\left(-\frac{ky}{\sqrt{1-k^2}}\right) dk \right\}, \quad n > 1 \\ I_6^{(n)} &\equiv \Im \left\{ \int_1^\infty \frac{ke^{ik\tilde{x}}}{k^2 - k_n^2} \exp\left(i\frac{ky}{\sqrt{k^2-1}}\right) dk \right\}, \quad n > 1 \end{aligned} \quad (74)$$

This results contains the proper jump condition for higher harmonics,  $n > 2$ . However, the first harmonic in the outer domain still does not match the first harmonic in the inner. In order to correct that, we add another linear solution to the solution in the outer domain, such that the the first harmonic also satisfies the jump condition. The final result is

$$\begin{aligned} \tilde{\psi} &= \left[ 4\hat{a}(0) - \sum_{n=2}^{\infty} \hat{s}_n(0) \right] \Re\{I_1 + I_2\} + \sum_{n=2}^{\infty} \Phi_{\tilde{x}}^{(n)} + 2 \left[ \hat{s}_1(0) \tilde{\psi}_a^{(1)} + \hat{r}_1(0) \tilde{\psi}_b^{(1)} \right] \\ \tilde{w} &= \left[ 4\hat{a}(0) - \sum_{n=2}^{\infty} \hat{s}_n(0) \right] \Re\{I_3 + I_4\} + \sum_{n=2}^{\infty} \Phi_y^{(n)} + 2 \left[ \hat{s}_1(0) \tilde{w}_a^{(1)} + \hat{r}_1(0) \tilde{w}_b^{(1)} \right] \end{aligned} \quad (75)$$

where

$$\begin{aligned}
\tilde{\psi}_a^{(1)} &\equiv I_1 + I_7 \\
\tilde{\psi}_b^{(1)} &\equiv \Re \left\{ \int_1^\infty \sin \left( \frac{\tilde{k}y}{\sqrt{\tilde{k}^2 - 1}} \right) e^{i\tilde{k}\tilde{x}} d\tilde{k} \right\} \\
\tilde{w}_a^{(1)} &\equiv I_3 + I_8 \\
\tilde{w}_b^{(1)} &\equiv \Im \left\{ \int_1^\infty \frac{e^{i\tilde{k}\tilde{x}}}{\sqrt{\tilde{k}^2 - 1}} \cos \left( \frac{\tilde{k}y}{\sqrt{\tilde{k}^2 - 1}} \right) d\tilde{k} \right\} \\
I_7 &\equiv \Re \left\{ \int_1^\infty \cos \left( \frac{\tilde{k}y}{\sqrt{\tilde{k}^2 - 1}} \right) e^{i\tilde{k}\tilde{x}} d\tilde{k} \right\} \\
I_8 &\equiv -\Im \left\{ \int_1^\infty \frac{e^{i\tilde{k}\tilde{x}}}{\tilde{k}^2 - 1} \sin \left( \frac{\tilde{k}y}{\sqrt{\tilde{k}^2 - 1}} \right) d\tilde{k} \right\}
\end{aligned} \tag{76}$$

## 1.6 Analytic Results

Figures 6 and 7 show the streamlines for the linear and nonlinear cases, respectively for a Gaussian mountain (9) of amplitude  $\epsilon = 0.75$  and a Rossby number  $Ro = 3$ . The solution is only shown downstream of the topography where the outer, nonlinear analytic theory is valid for  $x \gg 0$ . Qualitatively the linear and nonlinear streamlines are very similar. This is consistent with the numerical simulations of Trüb and Davies[22].

Figures 8 and 9 are spanwise velocity analogs of Figures 6 and 7, respectively, showing the spanwise velocity far downstream of the topography. Here the linear and nonlinear solutions are qualitatively quite different. While the linear spanwise velocity has relatively long contours of constant velocity running primarily from a high altitude upstream to a low altitude downstream, the nonlinear spanwise velocity exhibits much more structure as shown by the closed contours of spanwise velocity in Figure 9. This is indicative of the nonlinearity in the inner solution, which forces higher harmonics in the outer solution. These higher harmonics propagate far downstream of the topography and do not dissipate because the analytic model does not include viscous and turbulent dissipative effects.

## 1.7 Computational Approach

In addition to an analytic theory for the examination of rotation effects on nonlinear flow over topography, a computer code has been developed for the fully numeric simulation of these waves. The code solves Euler's equations in a rotating coordinate system as given in (1) using a projection method for density-stratified fluid based on the work of Bell and others [2, 3] as implemented by Skopovi [18, 19, 20].

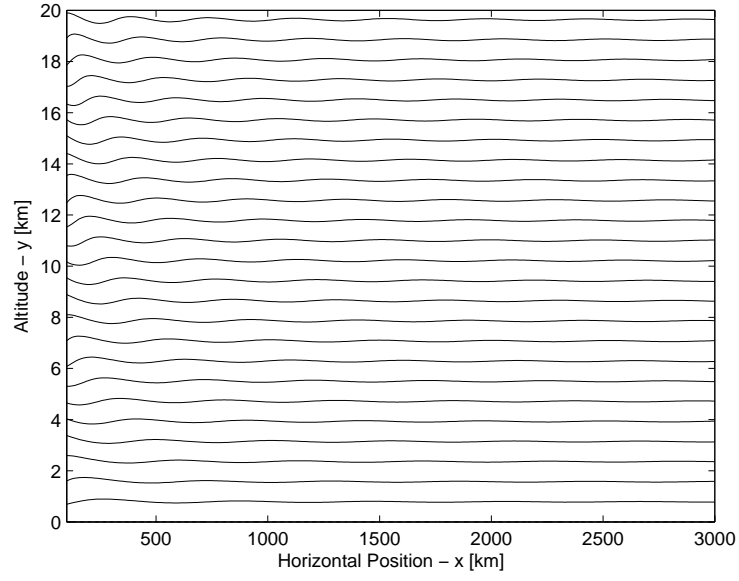


Figure 6: Streamlines from linear analytic solution far downstream of Gaussian topography for  $\epsilon = 0.75$  and  $Ro = 3$ . The values of the Coriolis parameter, Brunt-Väisälä frequency, freestream velocity, mountain width and mountain height for this simulation were  $f = 1.0 \times 10^{-4} \text{ sec}^{-1}$ ,  $N_0 = 1.0 \times 10^{-2} \text{ sec}^{-1}$ ,  $U_0 = 10 \text{ m/s}$ ,  $L_0 = 33.3 \text{ km}$  and  $h_0 = 0.75 \text{ km}$ , respectively. The topography shape is Gaussian (9).

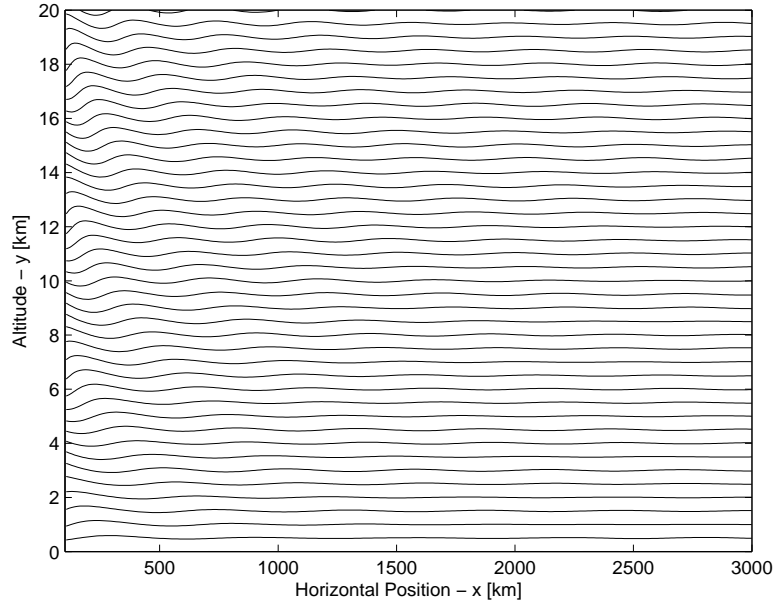


Figure 7: Nonlinear analytic streamfunction in the outer domain given by the matched asymptotic solution. The parameters used are the same as those for Figure 6.

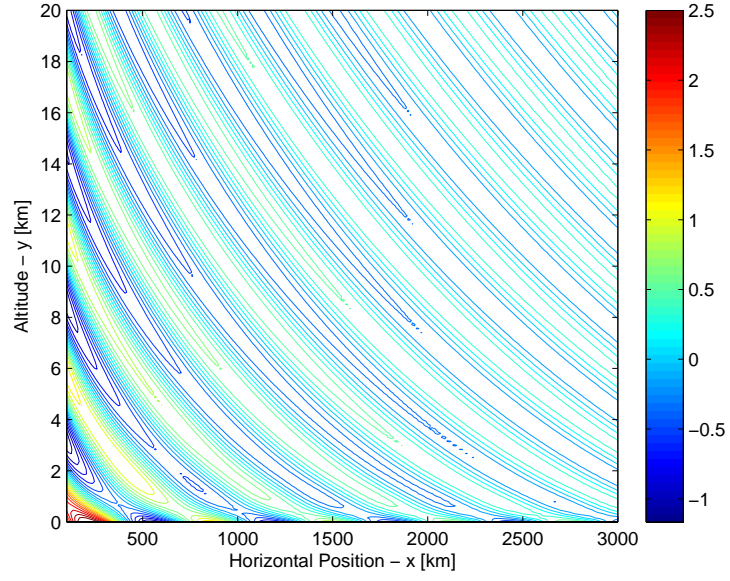


Figure 8: Spanwise velocity from linear analytic solution far downstream of Gaussian topography for  $\epsilon = 0.75$  and  $Ro = 3$ . The values of the Coriolis parameter, Brunt–Väisälä frequency, freestream velocity, mountain width and mountain height for this simulation were  $f = 1.0 \times 10^{-4} \text{ sec}^{-1}$ ,  $N_0 = 1.0 \times 10^{-2} \text{ sec}^{-1}$ ,  $U_0 = 10 \text{ m/s}$ ,  $L_0 = 33.3 \text{ km}$  and  $h_0 = 0.75 \text{ km}$ , respectively. The topography shape is Gaussian (9).

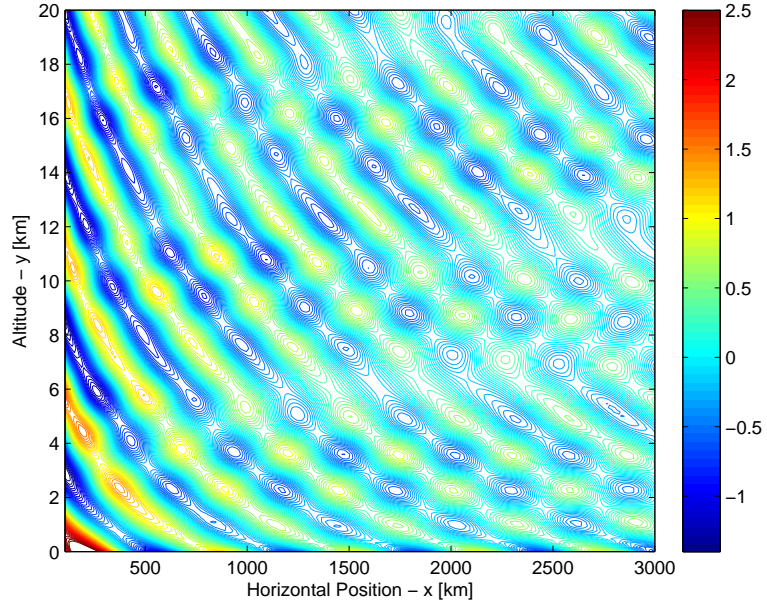


Figure 9: Nonlinear analytic spanwise velocity in the outer domain given by the matched asymptotic solution. The parameters used are the same as those for Figure 8.

### 1.7.1 Overview of Projection Method

One of the difficulties in the modeling of incompressible flow is that the time derivative of pressure does not appear explicitly, so it is not straightforward to write a time-evolution equation for it and integrate in time, as done with velocity and density. One approach to resolve this is known as the projection method wherein the velocity is evolved in time using a finite-difference approximation, and the time derivative of velocity is given by all the terms in the Navier-Stokes equation with the exception of the pressure gradient term. For a simple forward Euler time discretization, this could be written as

$$\mathbf{u}^* = \mathbf{u}^{(n)} + \Delta t \mathbf{f}^{(n)} \quad (77)$$

where  $\mathbf{u}^*$  is an initial approximation to the velocity vector at the next time step, and  $\mathbf{f}$  is the vector of forces acting on the fluid including all stresses with the exception of pressure. This new approximation of velocity,  $\mathbf{u}^*$  will not be divergence-free in general, which violates conservation of mass. In order to make the new velocity field divergence-free, the projection step is used, whereby  $\mathbf{u}^*$  is projected onto a divergence-free vector space. In time the velocity is advanced as

$$\mathbf{u}^{(n+1)} = \mathbf{u}^* - \Delta t \nabla p \quad (78)$$

Taking the divergence of this gives

$$\nabla \cdot \mathbf{u}^{(n+1)} = \nabla \cdot \mathbf{u}^* - \Delta t \nabla^2 p$$

The left-hand-side of this is zero in order for the flow to be incompressible, and the appropriate pressure is determined by solving the Poisson equation

$$\nabla^2 p = \frac{1}{\Delta t} \nabla \cdot \mathbf{u}^* \quad (79)$$

Once the pressure is known, its gradient can be determined and the velocity can be updated using (78).

The Euler equations are inherently nonlinear because of the advective terms. In this numerical model, the advective terms are treated using a finite-volume approach in order to conserve momentum. The second-order Godunov method is used to approximate fluxes across finite-volume boundaries. The implementation follows the work of Bell and others [2, 3] and is the approach used by Skopovi [18, 19].

### 1.7.2 Viscous Boundary Layers

Throughout the analytical derivation, the radiation condition was utilized to ensure energy propagates upwards and downstream, away from the topography. The radiation condition was required for the steady-state solution. If an initial value problem is solved, as is the case for these fully numeric simulations, a radiation condition is not needed because energy



will naturally propagate outward from the topography. However, another difficulty arises because the computational procedure is inherently limited to a finite domain. Thus the issue arises of what to do when the wave energy reaches the boundary of the computational domain. Methods of canceling the wave energy have been proposed for a monochromatic spectrum [7]. However, in the current problem, the spectrum is not monochromatic. Skopovi [18, 19, 20] has used viscous boundary layers to dissipate the wave energy before it reaches the boundary of the domain.

In this approach, the Euler equations of (1) are modified to include a Newtonian viscous dissipation term as

$$\begin{aligned}
\rho \left( \frac{Du}{Dt} + fw \right) &= -p_x + \mu \left( \frac{\partial^2 u}{\partial x^2} + \frac{\partial^2 u}{\partial y^2} \right) \\
\rho \frac{Dv}{Dt} &= -p_y - g\rho + \mu \left( \frac{\partial^2 v}{\partial x^2} + \frac{\partial^2 v}{\partial y^2} \right) \\
\rho \left( \frac{Dw}{Dt} - fu \right) &= -p_z + \mu \left( \frac{\partial^2 w}{\partial x^2} + \frac{\partial^2 w}{\partial y^2} \right) \\
\nabla \cdot \mathbf{u} &= 0 \\
\frac{D\rho}{Dt} &= 0
\end{aligned} \tag{80}$$

where  $\mu = \mu(x, y)$  is a nonuniform coefficient of viscosity. Note that this formulation does not agree with physical formulation of flow in a field of nonuniform viscosity, where the gradient of the stress tensor appears on the right-hand-side and

$$\nabla \cdot (\mu \nabla \mathbf{u}) \neq \mu \nabla^2 \mathbf{u}$$

Nevertheless, the viscous boundary layers are inherently non-physical and our only concern is the prevention of reflections at the boundary. Thus the choice of viscous layer thickness and viscosity profile is empirical. Following the work of Skopovi, we choose a sinusoidal profile for the viscosity in the viscous layers. In the viscous layer at the top of the domain, the viscosity is given as

$$\mu = \mu_0 \sin \left( \frac{\pi}{2} \frac{y - y_0}{Y - y_0} \right), \quad y_0 < y < Y$$

where  $y$  is the vertical coordinate,  $y_0$  the height at which the viscous boundary layer begins, and  $Y$  the height of the top of the computational domain. An analogous formula is implemented for the viscous boundary layers at the left and right edges of the computational domain, and the reader is referred to Skopovi [19] for more detail. A representative distribution of viscosity is shown in Figure 10 where  $x$  and  $y$  are nondimensional coordinates used in the computations.

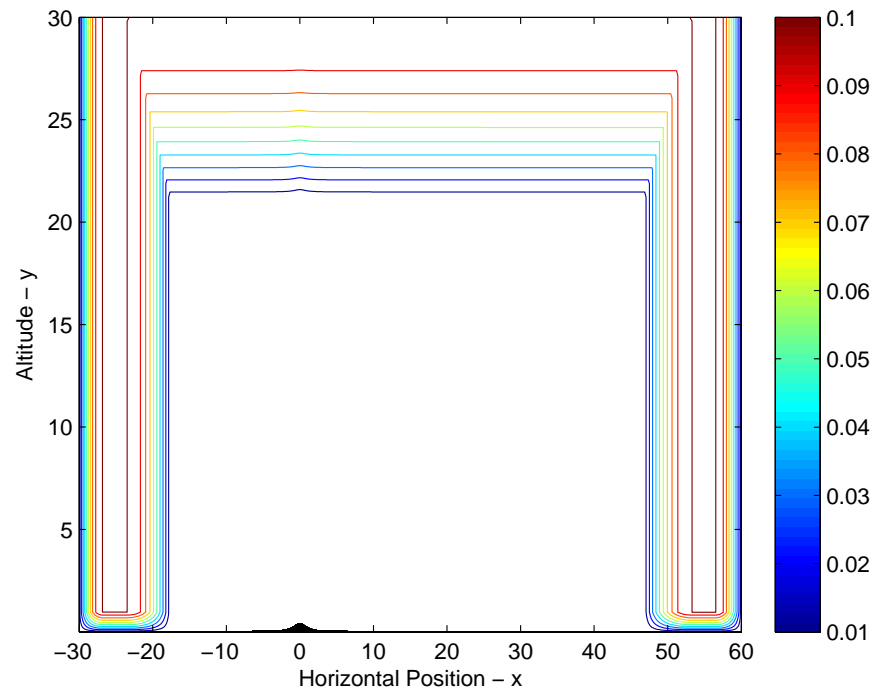


Figure 10: Contours of viscosity for viscous boundary layers used to damp and absorb waves at boundaries of domain. The viscous boundary layers are used as an artificial radiation condition.

The inclusion of viscous terms in an explicit temporal discretization results in a more severe stability constraint, requiring  $\Delta t \sim \mathcal{O}(\Delta x^2, \Delta y^2)$  as opposed to the stability constraint for inviscid flow of  $\Delta t \sim \mathcal{O}(\Delta x, \Delta y)$ . In order to eliminate the need for an extremely small timestep, the viscous terms are treated implicitly by solving

$$\mathbf{u}^* = \mathbf{u}^{(n)} + \Delta t \mu \nabla^2 \mathbf{u}^*$$

using Cholesky factorization.

## 1.8 Computational Results

Figures 11 and 12 show the streamlines and spanwise velocity, respectively, evaluated using the fully numeric simulation for stratified flow over topography with weak rotation. The results are for a nondimensional mountain amplitude of  $\epsilon = 0.40$  and the results are scaled up linearly to an amplitude of  $\epsilon = 0.75$  for comparison with the nonlinear results shown in Figures 13 and 14. The results are qualitatively quite similar to the linear, analytic solution shown in Figures 3 and 4 with different scaling because a Rossby number of 5 had been used for the linear, analytic results previously. The waves propagate upward and downstream (rightward) from the topography. The plotted solution has not yet reached steady-state far aloft and downwind of the topography. The results are plotted for this time despite having not achieved steady-state because as time increases, the viscous layers become saturated and are no longer able to dissipate all waves at the boundary. Thus for large times, spurious reflections from the viscous layers and boundaries are found in the interior of the domain. The results shown in Figures 11 through 14 have negligible reflections but have not reached steady-state throughout the domain.

Figures 13 and 14 show the numerically calculated streamfunction and spanwise velocity respectively. These plots are analogous to those in Figures 11 and 12 with the only difference being that the topography amplitude is  $\epsilon = 0.75$  for Figures 13 and 14, whereas it is  $\epsilon = 0.40$  for Figures 11 and 12.

Qualitatively, the numeric results with  $\epsilon = 0.40$  differ very little from those with  $\epsilon = 0.75$ . While the analytic theory showed much more structure in the spanwise velocity for the case of  $\epsilon = 0.75$ , the fully numeric solution does not show this. Part of the reason for this is that the numerical solutions have achieved steady-state for a very limited horizontal domain. The analytic results in Figure 9 show closed contours of spanwise velocity far downstream of the topography, and very few of these contours are present in the domain  $x < 900$  km, for which we have numeric results.

## 1.9 Discussion

The results of this section show that, for a single layer of uniformly stratified flow, nonlinear interactions above the mountain generate higher-harmonic disturbances that propagate far downstream of the topography. This is best seen in comparing Figure 9 for nonlinear spanwise velocity with Figure 8 for the corresponding linear result of spanwise velocity. While

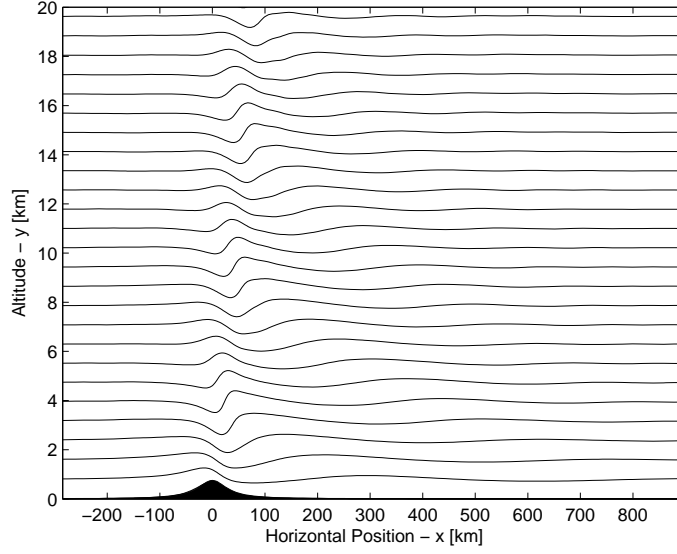


Figure 11: Streamlines from fully numeric simulation for relatively weak nonlinearity. The values of characteristic Coriolis parameter, Brunt–Väisälä frequency, undisturbed wind speed, mountain width and mountain height for this simulation were  $f = 1.0 \times 10^{-4} \text{ sec}^{-1}$ ,  $N_0 = 1.0 \times 10^{-2} \text{ sec}^{-1}$ ,  $U_0 = 10 \text{ m/s}$ ,  $L_0 = 33.3 \text{ km}$  and  $h_0 = 0.40 \text{ km}$ , giving nondimensional parameters  $Ro = 3$ ,  $\epsilon = 0.40$  and  $\mu = \frac{1}{6}$ . The streamlines are plotted at a computational time of  $t_{comp} = 200$ , corresponding to a nondimensional time of  $t = 33.33$  or a physical time of  $t_{dimensional} \approx 185 \text{ hr}$ . The amplitude of the streamfunction disturbance is scaled by a factor of 1.875 for comparison with results for the larger-amplitude mountain below.

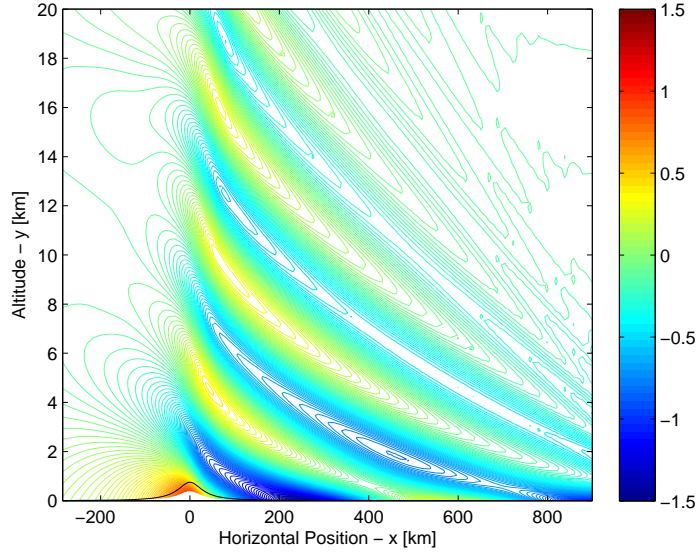


Figure 12: Spanwise velocity,  $w$  [m/s], from fully numeric simulation for relatively weak nonlinearity. The parameters for these results are the same as those for Figure 11. The amplitude of the spanwise velocity is scaled by a factor of 1.875 for comparison with results for the larger-amplitude mountain below.

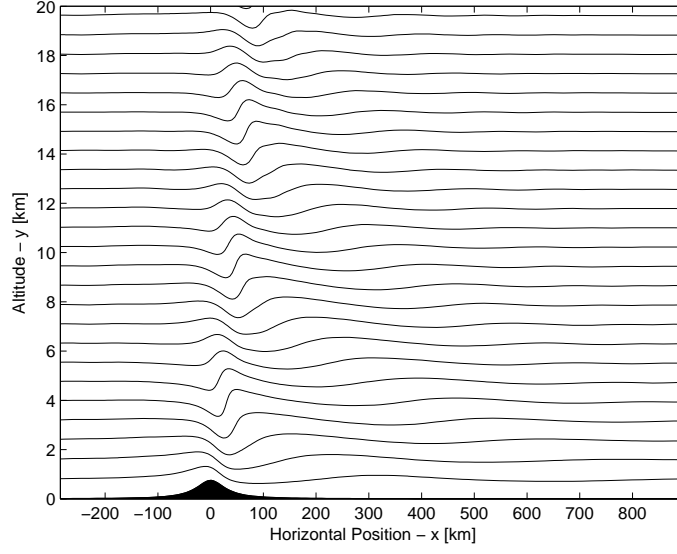


Figure 13: Streamlines from fully numeric simulation for mountain with nondimensional amplitude  $\epsilon = 0.75$ . The parameters are the same as those for Figure 12, with the exception of the topography height and nondimensional amplitude, for which the values are  $h_0 = 0.75$  km and  $\epsilon = 0.75$ , respectively. Furthermore, the amplitude of the response is unscaled.

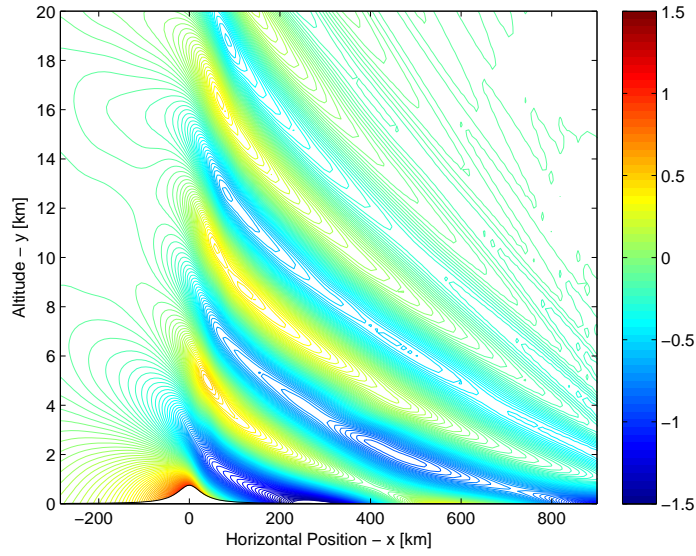


Figure 14: Spanwise velocity from fully numeric simulation for relatively strong nonlinearity.

these higher harmonics are present for a single layer atmosphere, they are relatively weak because the nonlinear interactions in Long’s solution for a single layer are relatively weak. Thus the analysis serves as a proof-of-concept showing inertia-gravity waves far downstream produced by nonlinear interactions above the mountain, but these waves have relatively small amplitude due to weak nonlinear interactions. The subsequent section shows that in a two-layer atmosphere, the effect of the tropopause can significantly increase the amplitude of the nonlinearly generated inertia-gravity waves downstream.

The numerical results in this section are rather inconclusive. The primary cause is limited computational resources. The fully numeric simulation is constrained to a finite domain and the simulations are started from a uniform velocity field and allowed to evolve in time. The spatial and temporal domains shown in Figures 11 through 14 are insufficient to conclusively resolve nonlinearities far downstream of the topography at steady-state. For example, the horizontal domain for the numerical results is limited to  $x < 900$  km in the numerical results of Figures 11 through 14. This implies that the analytical theory provides a predictive model yielding information unable to be obtained from these numeric simulations.

In summary, the results of this analysis show that nonlinearity in the inner solution slightly affects the spanwise velocity in the outer solution. However, this forcing is relatively weak because the nonlinearities above the topography in Long’s solution for a single, uniformly stratified layer are relatively weak, and the nonlinear solution does not differ appreciably from Long’s solution in the linear limit. Next we examine the effect of the tropopause in a model atmosphere with two layers of uniformly stratified flow and seek conditions for which the nonlinear forcing of the outer solution is stronger.

## 2 Two Layers of Uniform Stratification – Effect of the Tropopause

### 2.1 Governing Equations

In general, there is a change in the Brunt–Väisälä frequency across the tropopause, with the Brunt–Väisälä frequency typically being smaller in the troposphere and larger in the stratosphere. While the Brunt–Väisälä frequency is not spatially uniform in either layer of the atmosphere, we formulate a model to examine the effect this change in Brunt–Väisälä frequency across the tropopause has in conjunction with nonlinearity and rotation. The effect of the tropopause for cases excluding rotation has been previously studied by several investigators including Durran[6] and Davis[5]. In this investigation, we utilize the framework of matched asymptotics developed above to analyze a system with two layers of uniform Brunt–Väisälä frequency in the presence of nonlinearity and rotation. The model under investigation is sketched in Figure 15.

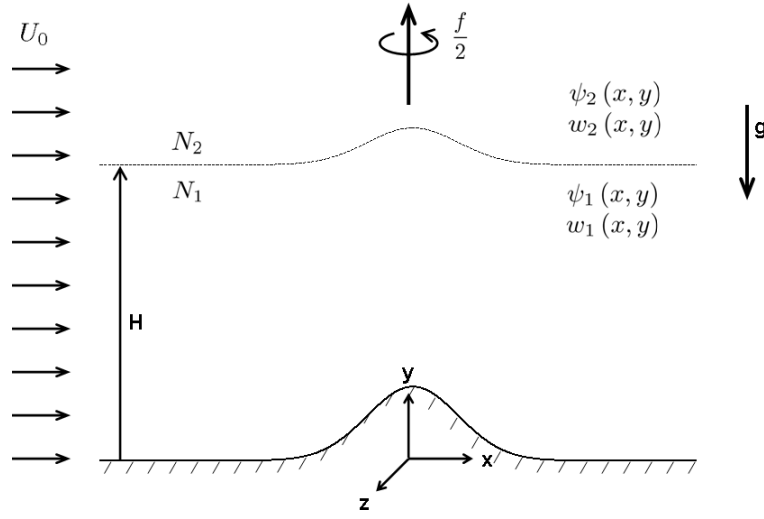


Figure 15: Physical system of stratified flow over topography in the presence of rotation incorporating the effect of the tropopause.

The governing equations for this system are those derived in §1.1 and given in (35) and (36) where we set the Brunt–Väisälä frequency to  $N_1$  in the troposphere and  $N_2$  in the stratosphere, with a step-change at the tropopause.

$$\begin{aligned}
 \Psi_{(1),yy} + N_1^2 (\Psi_{(1)} - y) &= -\frac{1}{Ro^2} \frac{\partial}{\partial \Psi} \int_{-\infty}^x w|_{\Psi} dx', \quad \Psi < \Psi^* \\
 \Psi_{(2),yy} + N_2^2 (\Psi_{(2)} - y) &= -\frac{1}{Ro^2} \frac{\partial}{\partial \Psi} \int_{-\infty}^x w|_{\Psi} dx', \quad \Psi > \Psi^* \\
 w &= \frac{\partial}{\partial \Psi} \int_{-\infty}^x (\Psi - y)|_{\Psi} dx', \quad \forall y > \epsilon h(x)
 \end{aligned} \tag{81}$$

where  $\Psi^*$  is the streamline on the tropopause separating the troposphere and stratosphere. As in the case of a single layer of stratified flow, the kinematic boundary condition at the surface of the topography is imposed, implying that there is no flow normal to the surface and resulting in the fact that the topography is itself a streamline.

$$\Psi = 0, \quad y = \epsilon h(x) \quad (82)$$

The radiation condition as  $y \rightarrow \infty$  must also be imposed. Finally, we must impose some interfacial conditions at the tropopause. The first is the kinematic condition requiring the flow in the vertical direction to be equal on either side of the tropopause, resulting in the fact that tropopause itself is a streamline and the streamfunction on either side must be equal to zero.

$$\Psi_{(1)} = \Psi_{(2)} = \Psi^*, \quad \Psi = \Psi^* \quad (83)$$

Since the mass flow rate between two streamlines is proportional to the difference in streamfunction, this is consistent with the fact that the troposphere and stratosphere are in contact with each other and there is no flow between the two layers. This assumes the tropopause has infinitesimal thickness, consistent with the model proposed in (81).

The second interface condition is a dynamic condition coming from a balance of pressure on either side of the tropopause streamline,  $\Psi^*$ .

$$p_1 = p_2, \quad \Psi = \Psi^*$$

which implies  $u_1 = u_2$  on  $\Psi = \Psi^*$  in the hydrostatic limit. Rewriting the horizontal velocity in terms of the streamfunction gives the second boundary condition at the tropopause.

$$\frac{\partial \Psi_{(1)}}{\partial y} = \frac{\partial \Psi_{(2)}}{\partial y}, \quad \Psi = \Psi^* \quad (84)$$

## 2.2 Linear, Uniformly Valid Solution

In the limit of  $\epsilon \rightarrow 0$ , the streamfunction disturbances are small (of order  $\epsilon$ ) and surfaces of constant altitude approach surfaces of constant streamfunction.

$$\Psi = y + \psi, \quad \psi = \mathcal{O}(\epsilon)$$

Then the boundary conditions at the topography and tropopause can be applied along contours of constant altitude. Decomposing the streamfunction into its undisturbed value,  $y$  and a streamfunction disturbance,  $\psi$ , the governing equations become

$$\begin{aligned} \psi_{(1),yy} + N_1^2 \psi_{(1)} + \frac{1}{Ro^2} \int_{-\infty}^x \int_{-\infty}^{x'} \psi_{(1),yy} dx'' dx', \quad y < H \\ \psi_{(2),yy} + N_2^2 \psi_{(2)} + \frac{1}{Ro^2} \int_{-\infty}^x \int_{-\infty}^{x'} \psi_{(2),yy} dx'' dx', \quad y > H \end{aligned} \quad (85)$$

$$w_{(1),x} = \psi_{(1),y}$$

$$w_{(2),x} = \psi_{(2),y}$$



subject to

$$\psi_{(1)} = -\epsilon h(x), \quad y = 0$$

$$\psi_{(1)} = \psi_{(2)}, \quad y = H \quad (86)$$

$$\frac{\partial \psi_{(1)}}{\partial y} = \frac{\partial \psi_{(2)}}{\partial y}, \quad y = H$$

and the radiation condition. The solution is

$$\begin{aligned} \psi_{(1)} &= 2\Re \left\{ \int_0^\beta \left[ -\epsilon \hat{h} \cosh \left( \frac{N_1 k y}{\sqrt{\beta^2 - k^2}} \right) + g \sinh \left( \frac{N_1 k y}{\sqrt{\beta^2 - k^2}} \right) \right] e^{ikx} dk \right. \\ &\quad \left. + \int_\beta^\infty \left[ -\epsilon \hat{h} \cos \left( \frac{N_1 k y}{\sqrt{k^2 - \beta^2}} \right) + g \sin \left( \frac{N_1 k y}{\sqrt{k^2 - \beta^2}} \right) \right] e^{ikx} dk \right\}, \quad y < H \\ \psi_{(2)} &= 2\Re \left\{ \int_0^\beta d \exp \left( \frac{-N_2 k y}{\sqrt{\beta^2 - k^2}} \right) e^{ikx} dk + \int_\beta^\infty c \exp \left( i \frac{N_2 k y}{\sqrt{k^2 - \beta^2}} \right) e^{ikx} dk \right\}, \quad y > H \\ w_{(1)} &= 2\Re \left\{ \int_0^\beta \frac{-iN_1}{\sqrt{\beta^2 - k^2}} \left[ -\epsilon \hat{h} \sinh \left( \frac{N_1 k y}{\sqrt{\beta^2 - k^2}} \right) + g \cosh \left( \frac{N_1 k y}{\sqrt{\beta^2 - k^2}} \right) \right] e^{ikx} dk \right. \\ &\quad \left. + \int_\beta^\infty \frac{-iN_1}{\sqrt{k^2 - \beta^2}} \left[ \epsilon \hat{h} \sin \left( \frac{N_1 k y}{\sqrt{k^2 - \beta^2}} \right) + g \cos \left( \frac{N_1 k y}{\sqrt{k^2 - \beta^2}} \right) \right] e^{ikx} dk \right\}, \quad y < H \\ w_{(2)} &= 2\Re \left\{ \int_0^\beta \frac{iN_2}{\sqrt{\beta^2 - k^2}} d \exp \left( \frac{-N_2 k y}{\sqrt{\beta^2 - k^2}} \right) e^{ikx} dk \right. \\ &\quad \left. + \int_\beta^\infty \frac{N_2}{\sqrt{k^2 - \beta^2}} c \exp \left( i \frac{N_2 k y}{\sqrt{k^2 - \beta^2}} \right) e^{ikx} dk \right\}, \quad y > H \end{aligned} \quad (87)$$

with constants of integration  $c(k)$ ,  $d(k)$  and  $g(k)$  determined from the matching conditions to be

$$\begin{aligned}
c(k) &= \frac{2N_1\hat{h}(k)}{(N_2 - N_1)\exp\left(i\frac{(N_1+N_2)kH}{\sqrt{k^2-\beta^2}}\right) - (N_1 + N_2)\exp\left(i\frac{(N_2-N_1)kH}{\sqrt{k^2-\beta^2}}\right)}, \quad \beta < k < \infty \\
d(k) &= \frac{-2N_1\hat{h}(k)}{(N_1 + N_2)\exp\left(\frac{(N_1-N_2)kH}{\sqrt{\beta^2-k^2}}\right) + (N_1 - N_2)\exp\left(\frac{-(N_1+N_2)kH}{\sqrt{\beta^2-k^2}}\right)}, \quad 0 < k < \beta \\
g(k) &= \begin{cases} \frac{(N_1 + N_2)\exp\left(\frac{(N_1-N_2)kH}{\sqrt{\beta^2-k^2}}\right) + (N_2 - N_1)\exp\left(\frac{-(N_1+N_2)kH}{\sqrt{\beta^2-k^2}}\right)}{(N_1 + N_2)\exp\left(\frac{(N_1-N_2)kH}{\sqrt{\beta^2-k^2}}\right) + (N_1 - N_2)\exp\left(\frac{-(N_1+N_2)kH}{\sqrt{\beta^2-k^2}}\right)}\hat{h}(k), & 0 < k < \beta \\ -i\frac{(N_1 - N_2)\exp\left(i\frac{(N_1+N_2)kH}{\sqrt{k^2-\beta^2}}\right) - (N_1 + N_2)\exp\left(i\frac{(N_2-N_1)kH}{\sqrt{k^2-\beta^2}}\right)}{(N_2 - N_1)\exp\left(i\frac{(N_1+N_2)kH}{\sqrt{k^2-\beta^2}}\right) - (N_1 + N_2)\exp\left(i\frac{(N_2-N_1)kH}{\sqrt{k^2-\beta^2}}\right)}\hat{h}(k), & \beta < k < \infty \end{cases}
\end{aligned} \tag{88}$$

The details of this solution are found in Appendix D.

### 2.3 Inner Solution

The preceding solution neglects the effect of nonlinearity, which is the primary concern of this study. In order to account for nonlinearity, a matched asymptotic solution is derived as in the case of a single layer of uniformly stratified flow. In the inner solution near the topography, treated as a weak perturbation to the two-layer analog of Long's solution. The governing equations for the inner solution are then

$$\begin{aligned}
\frac{\partial^2 \Psi_{(1)}^{(0)}}{\partial y^2} + N_1^2 (\Psi_{(1)}^{(0)} - y) &= 0, \quad \Psi < \Psi^* \\
\frac{\partial^2 \Psi_{(2)}^{(0)}}{\partial y^2} + N_2^2 (\Psi_{(2)}^{(0)} - y) &= 0, \quad \Psi > \Psi^*
\end{aligned} \tag{89}$$

$$w^{(0)} = \frac{\partial}{\partial \Psi^{(0)}} \int_{-\infty}^x (\Psi^{(0)} - y) \Big|_{\Psi^{(0)}} dx'$$

where the superscript (0) denotes the leading-order solution and the subscripts denote whether the solution is in the troposphere, (1), or the stratosphere, (2). Here the streamline,  $\Psi = \Psi^*$  is the streamline of the tropopause, which is not known *a priori* and must be determined as part of the solution of the equations.

The problem of two layers of uniformly stratified flow in the absence of rotation is an extension of Long's classic solution [14] and has been studied by Durran[6] and Davis[5]. The solution can be formulated generally as

$$\psi_{(1)} = a(x) \cos(N_1 y) + b(x) \sin(N_1 y), \quad \Psi < \Psi^* \quad (90)$$

$$\psi_{(2)} = c(x) \cos(N_2 y) + d(x) \sin(N_2 y), \quad \Psi > \Psi^*$$

where we have decomposed the streamfunction,  $\Psi$ , into the sum of its undisturbed value,  $y$  and a streamfunction disturbance,  $\psi$ . Then the kinematic boundary condition at the topography,  $y = h(x)$ , requires

$$a \cos(N_1 h) + b \sin(N_1 h) = -h(x) \quad (91)$$

and the radiation condition as  $y \rightarrow \infty$  gives

$$d(x) = \mathcal{H}\{c(x)\} \quad (92)$$

resulting in wave energy propagating vertically upwards. As in the linear case, two conditions are needed at the tropopause to match the solutions in the troposphere and stratosphere. We can write the curve of the troposphere as

$$\Psi^* = H + \psi^*(x) = H - \eta(x) \quad (93)$$

where  $H$  is the undisturbed height of the tropopause and  $\eta$  is the vertical displacement of the tropopause, giving the tropopause location as  $y = H + \eta(x)$ , which is also unknown. The first matching condition at the tropopause is the kinematic matching condition requiring the streamfunction in the troposphere and stratosphere to be equal at the tropopause. This gives

$$a \cos[N_1(H + \eta)] + b \sin[N_1(H + \eta)] = c \cos[N_2(H + \eta)] + d \sin[N_2(H + \eta)] \quad (94)$$

The second interface matching condition is the dynamic boundary condition requiring the pressure to be equal on either side of the tropopause. Integrating Bernoulli's equation from far upstream and noting that the density in the troposphere at the tropopause is equal to the density in the stratosphere at the tropopause, gives

$$u_{(1)} = u_{(2)}, \quad y = H + \eta \quad \Rightarrow \quad \frac{\partial \psi_{(1)}}{\partial y} = \frac{\partial \psi_{(2)}}{\partial y}, \quad y = H + \eta \quad (95)$$

Substituting the general solution of (90) gives

$$N_1 \{-a \sin[N_1(H + \eta)] + b \cos[N_1(H + \eta)]\} = N_2 \{-c \sin[N_2(H + \eta)] + d \cos[N_2(H + \eta)]\} \quad (96)$$

Finally, the fifth equation needed is simply a specification of the tropopause displacement,  $\eta$ .

$$\eta = -\psi^* = -a(x) \cos[N_1(H + \eta)] - b(x) \sin[N_1(H + \eta)] \quad (97)$$

Thus (91), (92), (94), (96) and (97) are the five equations used to determine  $a(x)$ ,  $b(x)$ ,  $c(x)$ ,  $d(x)$  and  $\eta(x)$ . These are system of nonlinear equations because the boundary and matching conditions are applied along contours of constant streamfunction, as opposed to contours of constant altitude. They can be solved numerically using an iterative procedure, such as Newton-Raphson.

## 2.4 Outer Solution

The outer solution is obtained by scaling the linear, uniformly valid solution of (87) into the outer variables as done for the single-layer case above. Without loss of generality, we can set the nondimensionalized Brunt–Väisälä frequency in the stratosphere equal to unity,  $N_2 = 1$ , and the nondimensionalized Brunt–Väisälä frequency in the tropopause to  $N_1 = N$ . Then the outer solution is

$$\begin{aligned}\tilde{\psi}_{(1)} &= -2 \left( \tilde{I}_1 + \tilde{I}_2 \right) \\ \tilde{\psi}_{(2)} &= -2 \left( \tilde{I}_3 + \tilde{I}_4 \right) \\ \tilde{w}_{(1)} &= -2 \left( \tilde{I}_5 + \tilde{I}_6 \right) \\ \tilde{w}_{(2)} &= -2 \left( \tilde{I}_7 + \tilde{I}_8 \right)\end{aligned}\tag{98}$$

where the integrals are defined in Appendix E and have asymptotic behavior as  $\tilde{x} \rightarrow 0$  of

$$\left. \begin{aligned}\tilde{\psi}_{(1)} &\sim 2\epsilon\hat{h}(0) \frac{1}{\tilde{x}} \frac{N \sin Ny}{N^2 \cos^2 NH + \sin^2 NH} \\ \tilde{\psi}_{(2)} &\sim 2\epsilon\hat{h}(0) \frac{1}{\tilde{x}} \frac{N}{N^2 \cos^2 NH + \sin^2 NH} [\sin NH \cos(y-H) + N \cos NH \sin(y-H)] \\ \tilde{w}_{(1)} &\sim \frac{2\epsilon\hat{h}(0) N}{N^2 \cos^2 NH + \sin^2 NH} \{N \ln |\tilde{x}| \cos Ny \\ &\quad + \frac{\pi}{2} \operatorname{sgn} \tilde{x} [N^2 \cos NH \sin N(y-H) + \sin NH \cos N(y-H)]\} \\ \tilde{w}_{(2)} &\sim \frac{2\epsilon\hat{h}(0) N}{N^2 \cos^2 NH + \sin^2 NH} \{\ln |\tilde{x}| [N \cos NH \cos(y-H) - \sin NH \sin(y-H)] \\ &\quad + \frac{\pi}{2} \operatorname{sgn} \tilde{x} [N \cos NH \sin(y-H) + \sin NH \cos(y-H)]\}\end{aligned}\right\}, \tilde{x} \rightarrow 0\tag{99}$$

and a jump in the spanwise velocity across the inner domain of

$$\begin{aligned}\tilde{w}_{(1)}\Big|_{0^-}^{0^+} &= \frac{2\pi\epsilon\hat{h}(0) N}{N^2 \cos^2 NH + \sin^2 NH} [N^2 \cos NH \sin N(y-H) + \sin NH \cos N(y-H)] \\ \tilde{w}_{(2)}\Big|_{0^-}^{0^+} &= \frac{2\pi\epsilon\hat{h}(0) N}{N^2 \cos^2 NH + \sin^2 NH} [N \cos NH \sin(y-H) + \sin NH \cos(y-H)]\end{aligned}\tag{100}$$

## 2.5 Matching

Rewriting the inner solution as

$$\begin{aligned}\psi_{(1)}^{(0)} &= r(x) \cos Ny + s(x) \sin Ny \\ \psi_{(2)}^{(0)} &= p(x) \cos(y - H) + \mathcal{H}\{p(x)\} \sin(y - H)\end{aligned}\tag{101}$$

the asymptotic behavior as  $x \rightarrow \infty$  is

$$\left. \begin{aligned} p(x) &\sim \frac{C}{x} \\ \mathcal{H}\{p(x)\} &\sim \frac{CN}{\tan NH} \frac{1}{x} \\ r(x) &\sim -\epsilon h(x) \\ s(x) &\sim \frac{C}{\sin NH} \frac{1}{x} \\ \eta(x) &\sim -p(x) \end{aligned} \right\}, \quad x \rightarrow \infty\tag{102}$$

where the constant  $C$  must be determined numerically. In the linear limit, the constant  $C$  approaches

$$C_{lin} = \frac{2N\epsilon\hat{h}(0) \sin NH}{N^2 \cos^2 NH + \sin^2 NH}\tag{103}$$

Thus

$$\left. \begin{aligned} \psi_{(1)}^{(0)} &\sim \frac{C}{\sin NH} \frac{\sin Ny}{x} \\ \psi_{(2)}^{(0)} &\sim C \frac{\cos(y - H) + \frac{N}{\tan NH} \sin(y - H)}{x} \end{aligned} \right\}, \quad x \rightarrow \infty\tag{104}$$

In order to properly match the jump in spanwise velocity, it is useful to rewrite the inner, nonlinear solution in terms of harmonics of the streamfunction as

$$\begin{aligned}\psi_{(1)}^{(0)} &= r \cos N(\Psi^{(0)} - H) + s \sin N(\Psi^{(0)} - H) \\ &\quad + \sum_{n=1}^{\infty} l_n^-(x) \sin nN(\Psi^{(0)} - y) + m_n^-(x) \cos nN(\Psi^{(0)} - y) \\ \psi_{(2)}^{(0)} &= p \cos(\Psi^{(0)} - H) + \mathcal{H}\{p\} \sin(\Psi^{(0)} - H) \\ &\quad + \sum_{n=1}^{\infty} l_n^+(x) \sin n(\Psi^{(0)} - y) + m_n^+(x) \cos n(\Psi^{(0)} - y)\end{aligned}\tag{105}$$

where  $l_n^\pm$  and  $m_n^\pm$  are the coefficients (as a function of  $x$ ) of the terms arising from nonlinear interactions in the inner solution. These terms will give rise to jumps in spanwise velocity at higher vertical harmonics and are the forcing of the higher harmonics in the outer solution. They can be evaluated by orthogonal decomposition as

$$\left. \begin{aligned} l_n^-(x) &= \frac{N}{\pi} \int_0^{\frac{2\pi}{N}} (\Psi^{(0)} - y) \sin nN\Psi^{(0)} d\Psi^{(0)} \\ m_n^-(x) &= \frac{N}{\pi} \int_0^{\frac{2\pi}{N}} (\Psi^{(0)} - y) \cos nN\Psi^{(0)} d\Psi^{(0)} \\ l_n^+(x) &= \frac{1}{\pi} \int_0^{2\pi} (\Psi^{(0)} - y) \sin n(\Psi^{(0)} - H) d(\Psi^{(0)} - H) \\ m_n^+(x) &= \frac{1}{\pi} \int_0^{2\pi} (\Psi^{(0)} - y) \cos n(\Psi^{(0)} - H) d(\Psi^{(0)} - H) \end{aligned} \right\}, \quad n = 2, 3, 4, \dots \quad (106)$$

and  $l_1^\pm$  and  $m_1^\pm$  can be found by subtracting the appropriate leading order function,  $p(x)$ ,  $\mathcal{H}\{p(x)\}$ ,  $r(x)$  or  $s(x)$ , from the orthogonal decomposition.

$$\begin{aligned} l_1^-(x) &= -s(x) + \frac{N}{\pi} \int_0^{\frac{2\pi}{N}} (\Psi^{(0)} - y) \sin N\Psi^{(0)} d\Psi^{(0)} \\ m_1^-(x) &= -r(x) + \frac{N}{\pi} \int_0^{\frac{2\pi}{N}} (\Psi^{(0)} - y) \cos N\Psi^{(0)} d\Psi^{(0)} \end{aligned} \quad (107)$$

$$l_1^+(x) = -p(x) + \frac{1}{\pi} \int_0^{2\pi} (\Psi^{(0)} - y) \sin(\Psi^{(0)} - H) d(\Psi^{(0)} - H)$$

$$m_1^+(x) = -\mathcal{H}\{p(x)\} + \frac{1}{\pi} \int_0^{2\pi} (\Psi^{(0)} - y) \cos(\Psi^{(0)} - H) d(\Psi^{(0)} - H)$$

Then the spanwise velocity is

$$\begin{aligned} w_{(1)}^{(0)} &= -N \sin N\Psi^{(0)} \int_0^x r(x') dx' + N \cos N\Psi^{(0)} \int_0^x s(x') dx' \\ &+ N \sum_{n=1}^{\infty} n \left\{ \cos nN\Psi^{(0)} \int_0^x l_n^-(x') dx' - \sin nN\Psi^{(0)} \int_0^x m_n^-(x') dx' \right\} + C_{(1)}(\Psi^{(0)}) \\ w_{(2)}^{(0)} &= -\sin(\Psi^{(0)} - H) \int_0^x p(x') dx' + \cos(\Psi^{(0)} - H) \int_0^x \mathcal{H}\{p(x')\} dx' \\ &+ \sum_{n=1}^{\infty} n \left\{ \cos n(\Psi^{(0)} - H) \int_0^x l_n^+(x') dx' - \sin n(\Psi^{(0)} - H) \int_0^x m_n^+(x') dx' \right\} + C_{(2)}(\Psi^{(0)}) \end{aligned} \quad (108)$$

Using the asymptotic behavior of the functions  $p(x)$ ,  $\mathcal{H}\{p(x)\}$ ,  $r(x)$  and  $s(x)$  given in (102), the asymptotic behavior of the spanwise velocity as  $x \rightarrow \infty$  is

$$\left. \begin{aligned} w_{(1)}^{(0)} &\sim \frac{CN}{\sin NH} \cos Ny \ln |x| \\ w_{(2)}^{(0)} &\sim C \left[ \frac{N}{\tan NH} \cos(y-H) - \sin(y-H) \right] \ln |x| \end{aligned} \right\}, \quad x \rightarrow \infty \quad (109)$$

exhibiting the same logarithmic divergence and lack of uniform validity as seen in the single layer of uniformly stratified flow and confirming the need for a matched asymptotic expansion. In addition to this logarithmic divergence, the spanwise velocity experiences a finite jump across the inner domain given by

$$\begin{aligned} w_{(1)}^{(0)} \Big|_{-\infty}^{\infty} &= -N \sin Ny \int_{-\infty}^{\infty} r(x') dx' + N \cos Ny \int_{-\infty}^{\infty} s(x') dx' \\ &\quad + N \sum_{n=1}^{\infty} n \left\{ \cos nNy \int_{-\infty}^{\infty} l_n^-(x') dx' - \sin nNy \int_{-\infty}^{\infty} m_n^-(x') dx' \right\} \\ w_{(2)}^{(0)} \Big|_{-\infty}^{\infty} &= -\sin(y-H) \int_{-\infty}^{\infty} p(x') dx' + \cos(y-H) \int_{-\infty}^{\infty} \mathcal{H}\{p(x')\} dx' \\ &\quad + \sum_{n=1}^{\infty} n \left\{ \cos n(y-H) \int_{-\infty}^{\infty} l_n^+(x') dx' - \sin n(y-H) \int_{-\infty}^{\infty} m_n^+(x') dx' \right\} + C_{(2)}(\Psi^{(0)}) \end{aligned} \quad (110)$$

In order to match the inner solution, we write the outer solution as a multiple of the linear outer solution given in (98) plus terms arising from nonlinearity in the inner solution.

$$\begin{aligned} \tilde{\psi}_{(1)}^{(0)} &= -2A(I_1 + I_2) + \psi_{(1),nonlin}^{(1)} + \sum_{n=2}^{\infty} \Phi_{(1),x}^{(n)} \\ \tilde{\psi}_{(2)}^{(0)} &= -2A(I_3 + I_4) + \psi_{(2),nonlin}^{(1)} + \sum_{n=2}^{\infty} \Phi_{(2),x}^{(n)} \\ \tilde{w}_{(1)}^{(0)} &= -2A(I_5 + I_6) + w_{(1),nonlin}^{(1)} + \sum_{n=2}^{\infty} \Phi_{(1),y}^{(n)} \\ \tilde{w}_{(2)}^{(0)} &= -2A(I_7 + I_8) + w_{(2),nonlin}^{(1)} + \sum_{n=2}^{\infty} \Phi_{(2),y}^{(n)} \end{aligned} \quad (111)$$

where  $\Phi_{(1),(2)}^{(n)}$  satisfy

$$\begin{aligned} \left( \frac{\partial^2 \Phi_{(1)}}{\partial y^2} + N^2 \Phi_{(1)} \right)_{\tilde{x}\tilde{x}} + \frac{\partial^2 \Phi_{(1)}}{\partial y^2} &= -2\pi N^2 (n^2 - 1) \delta'(\tilde{x}) \left\{ \hat{l}_n^-(0) \sin nNy + \hat{m}_n^-(0) \cos nNy \right\} \\ \left( \frac{\partial^2 \Phi_{(2)}}{\partial y^2} + N^2 \Phi_{(2)} \right)_{\tilde{x}\tilde{x}} + \frac{\partial^2 \Phi_{(2)}}{\partial y^2} &= -2\pi (n^2 - 1) \delta'(\tilde{x}) \left\{ \hat{l}_n^+(0) \sin n(y - H) + \hat{m}_n^+(0) \cos n(y - H) \right\} \end{aligned} \quad (112)$$

subject to the boundary condition at the topography, the matching conditions at the tropopause and the radiation condition as  $y \rightarrow \infty$ .

## 2.6 Results and Discussion – Analytic

In this two-layer model of the atmosphere, the height of the tropopause affects the amplitude of the waves. For certain tropopause heights, the amplitude of the waves can be significantly enhanced, which is commonly referred to as ‘tropopause tuning’. Likewise, detuning exists for other tropopause heights giving attenuated wave amplitudes. The phenomenon of tropopause tuning has been previously studied by Klemp and Lilly[11] and others who found that the response in the linear limit is tuned when the tropopause is located at odd multiples of half the vertical wavelength in the troposphere.

In order to investigate the phenomenon of tropopause tuning and the effect it has on inertial-gravity waves far downstream of the topography, we examined the response of the inner solution where rotation is negligible. The streamline slope is a measure of the nonlinearity of the solution, where the linear solution has slope of order  $\epsilon \rightarrow 0$  and the nonlinear solution has a finite slope. Figure 16 shows the maximum streamline slope in the lower layer of the inner solution as a function of tropopause height. It is seen that, for this range of tropopause heights, there are three distinct peaks at which the streamline slope is a local maximum, where the tropopause height is tuned.

The nonlinearity in the inner solution manifests itself in the outer solution through the nonlinear coefficients defined in (106) and (107). In order to verify that a tropopause height with steep streamlines will provide the largest amount of nonlinear forcing on the outer solution, these nonlinear coefficients,  $l_n^\pm$  and  $m_n^\pm$ , were examined as a function of tropopause height. Figure (17) shows a plot of  $\hat{m}_2^-(0) = \int_{-\infty}^{\infty} m_2(x) dx$  as a function of the tropopause height. The coefficient of the second harmonic was chosen because quadratic nonlinearities were larger than the higher harmonics. Again the three distinct local maxima are observed at approximately the same tropopause heights as those in Figure 16, confirming that steep streamlines give rise to larger nonlinearities.

Based upon the results of the streamline slope in Figure 16 and the coefficients of nonlinearity, of which Figure 17 is representative, two differencing cases were selected for comparison. A relatively tuned case with a tropopause height of  $H = 12.5$  km was compared with a



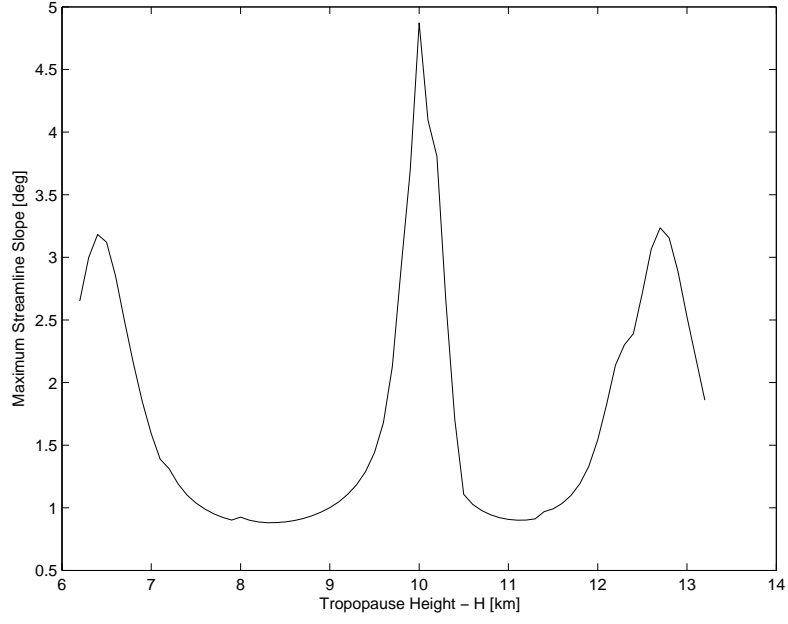


Figure 16: Maximum slope of streamlines in inner solution as a function of tropopause height for  $\epsilon = \frac{h_0 N_1}{U_0} = 0.375$ .

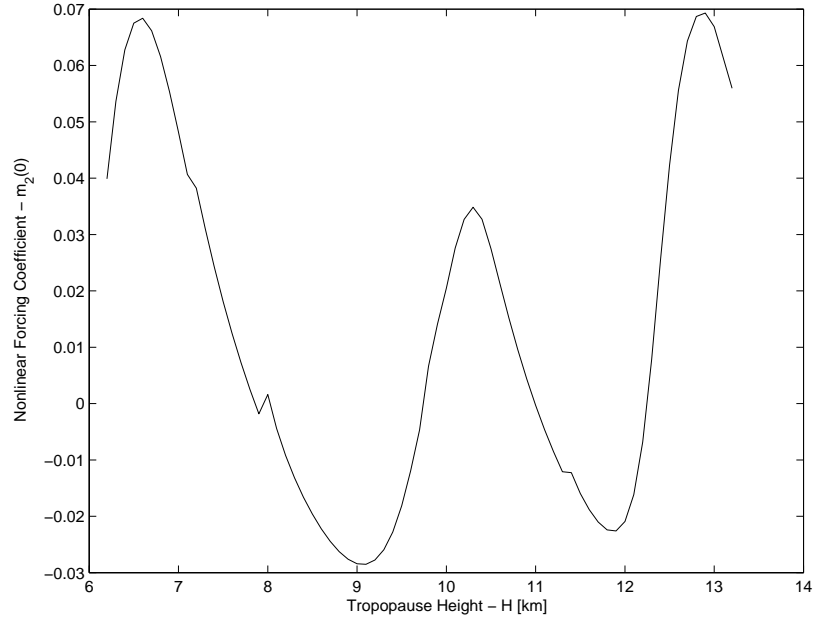


Figure 17: A representative coefficient,  $\hat{m}_2^-(0)$ , of nonlinearity below the tropopause giving rise to forcing of the outer solution by the nonlinearity in the inner solution. The  $n = 2$  mode is the quadratic nonlinearity and has the largest amplitude for this value of  $\epsilon \equiv \frac{h_0 N_1}{U_0} = 0.375$ .

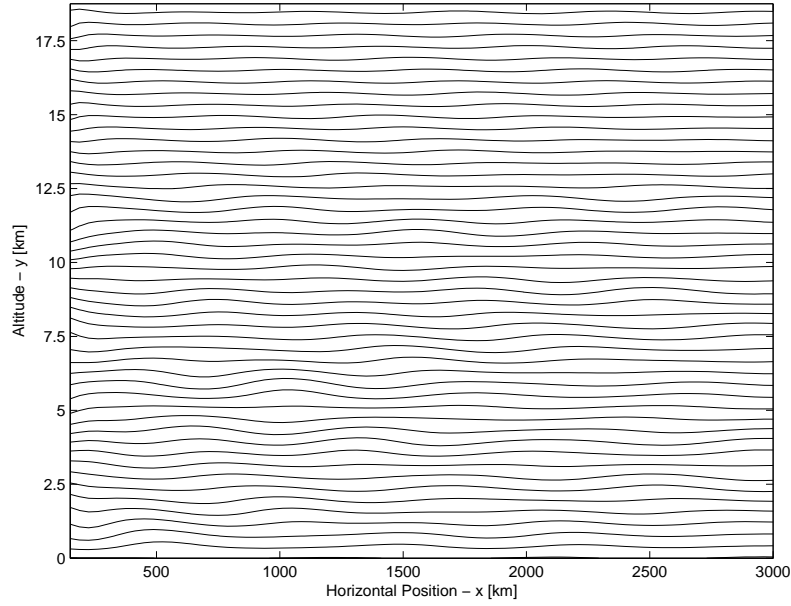


Figure 18: Streamfunction for flow of two layers of uniformly stratified fluid with mean velocity  $U_0 = 10$  m/s over a mountain of height  $h = 0.375$  km centered at  $x = 0$  km with Rossby number  $Ro = 3$ . Tuned case with tropopause height  $H = 12.5$  km. This case shows waves propagating far downwind of the topography with very little decrease in amplitude.

relatively detuned case with tropopause height  $H = 11.0$  km. Figures 18 and 19 show the analytical solutions for streamlines and spanwise velocity far downstream of the topography for the tuned case with tropopause height  $H = 12.5$  km. This is contrasted with the detuned case shown, for which the analogous results are shown in Figures 20 and 21.

The tuned and detuned streamlines in Figures 18 and 20, respectively, are qualitatively quite different. In the troposphere, the disturbance is significantly stronger for the tuned case. The waves in the troposphere propagate far downstream (3000 km) with no significant attenuation. The detuned streamlines in the troposphere show relatively weak waves that decay downstream of the mountain and are all but nonexistent 3000 km downstream of the topography. In the stratosphere, the differences between the tuned and detuned cases are not as severe. Both exhibit qualitatively similar streamline patterns, but in the tuned case the amplitude is larger further downstream.

The spanwise velocity profiles shown in Figure 19 for the tuned case and Figure 21 for the detuned case exhibit the same qualitative features as the streamlines. In the tropopause, the tuned response is much stronger than the detuned response and is nearly as strong 3000 km downstream of the mountain as it is 500 km downstream of the mountain. The detuned spanwise velocity in the troposphere is weaker than the tuned response, and its amplitude decays significantly as the distance downwind of the mountain increases. In the stratosphere, the spanwise velocity exhibits the closed contours characteristic of nonlinearities; whereas, the tuned response shows relatively long, smooth contours of spanwise velocity. This is

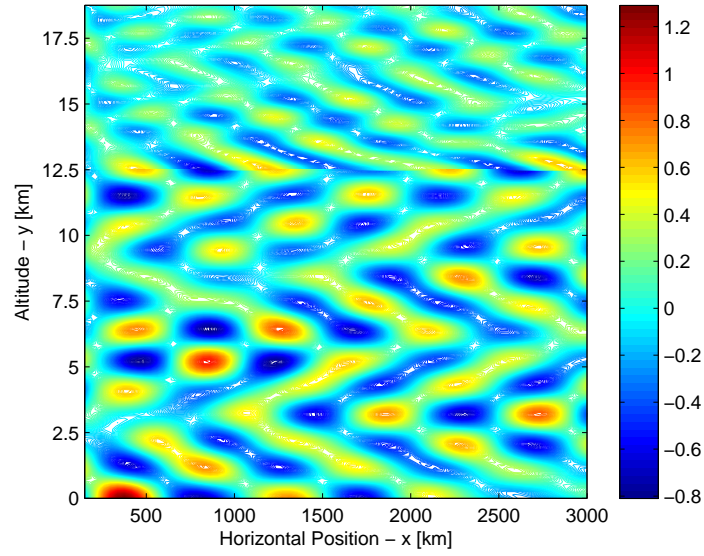


Figure 19: Contours of transverse velocity for flow of two layers of uniformly stratified fluid with mean velocity  $U_0 = 10$  m/s over a mountain of height  $h = 0.375$  km centered at  $x = 0$  km with Rossby number  $Ro = 3$ . Tuned case with tropopause height  $H = 12.5$  km. This case shows waves propagating far downwind of the topography with very little decrease in amplitude.

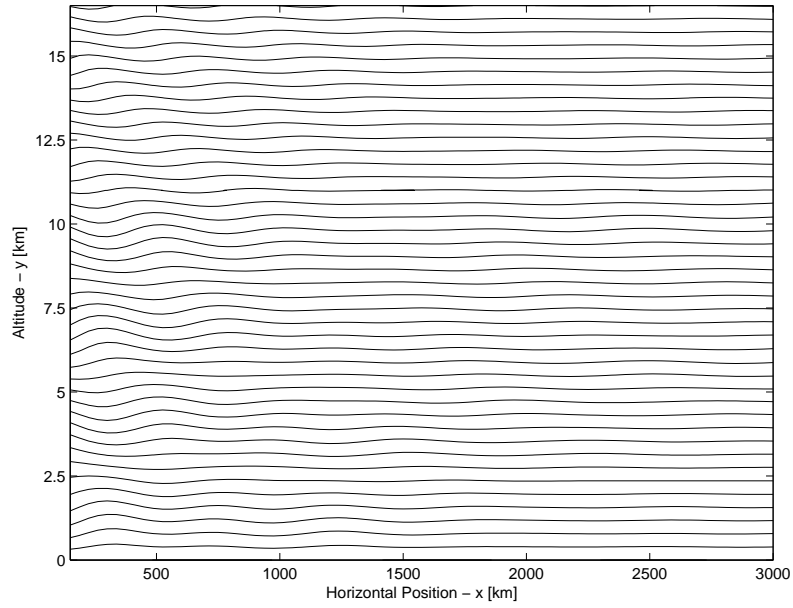


Figure 20: Streamfunction for flow of two layers of uniformly stratified fluid with mean velocity  $U_0 = 10$  m/s over a mountain of height  $h = 0.375$  km centered at  $x = 0$  km with Rossby number  $Ro = 3$ . Detuned case with tropopause height  $H = 11$  km. This response is relatively weak and decays far downstream of the topography.

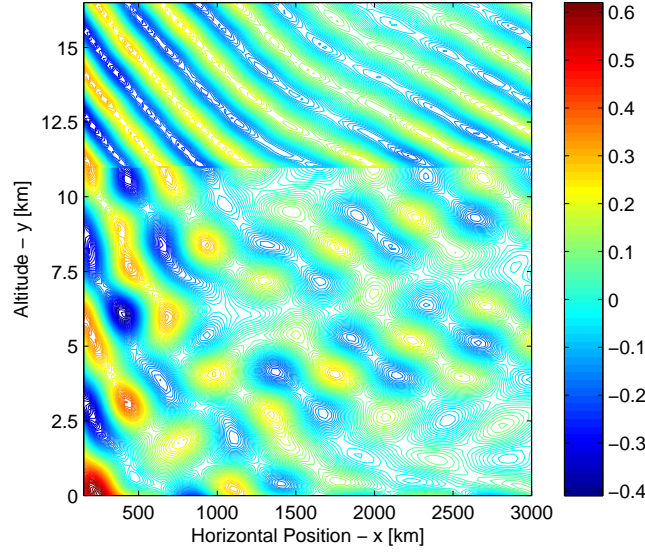


Figure 21: Contours of transverse velocity for flow of two layers of uniformly stratified fluid with mean velocity  $U_0 = 10$  m/s over a mountain of height  $h = 0.375$  km centered at  $x = 0$  km with Rossby number  $Ro = 3$ . Detuned case with tropopause height  $H = 11$  km. This response is relatively weak and decays far downstream of the topography.

similar to the observations in the single layer of uniformly stratified flow for the linear solution shown in Figure 8 and the nonlinear solution shown in Figure 9.

## 2.7 Results and Discussion – Numeric

In addition to the above analytic investigation of tropopause height, a companion numerical simulation was run to investigate the combined effect of the tropopause and nonlinearity. As stated above, the slopes of the streamlines in the inner solution along with the nonlinearity coefficients indicate that the tropopause is relatively tuned at heights of  $H \approx 6.5$  km, 10 km and 12.5 km. Because the inner solution is periodic, the effect of tropopause height is periodic with a period equal to the vertical wavelength in the troposphere. Thus the tuning seen at  $H = 12.5$  km investigated analytically above should be approximately equal to the tuning observed at a tropopause height of  $H = 6.5$  km. For the numerical simulations, a higher tropopause height will take longer to reach steady-state than a lower height, so the tropopause height of  $H = 6.5$  km was selected for our numerical investigation of tropopause tuning.

In the numeric code, the Brunt-Väisälä frequency profile is slightly smoothed. The functional form is a hyperbolic tangent specified as

$$N = \frac{1}{2} \{3 + a_N + b_N \tanh [c_N (z - d_N)]\} \quad (113)$$

where the four parameters  $a_N$ ,  $b_N$ ,  $c_N$  and  $d_N$  determine the location of the tropopause and

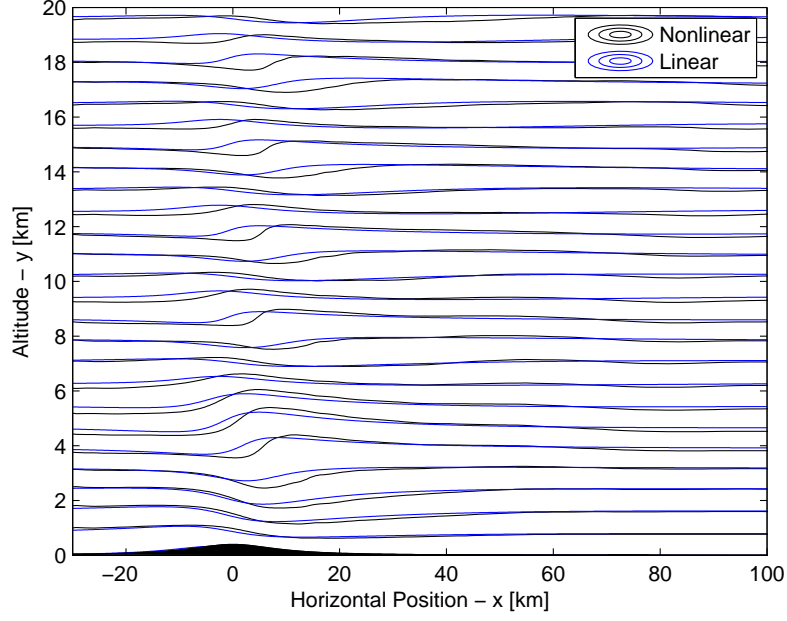


Figure 22: A comparison of numerically calculated nonlinear streamlines with the linear, analytic solution for two layers of uniformly stratified topography. The tropopause is located at a non-dimensional height of  $H = 6.5$ . In the numeric code, this is done using the functional form of (113). The amplitude of the topography is  $\epsilon \equiv \frac{h_0 N_1}{U_0} = 0.4$  and the Rossby number is  $Ro = 10$ .

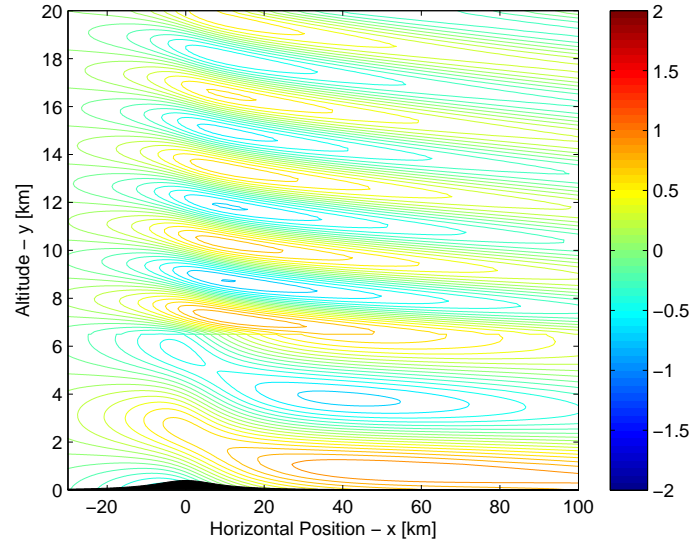
the sharpness of the transition of Brunt-Väisälä frequency in going from the troposphere to the stratosphere.

Figure 22 shows the streamlines for the numeric solution of stratified flow over topography in the presence of weak rotation, and provides a comparison with the linear, analytic, hydrostatic two-layer streamfunction solution of (87). The linear, analytic and nonlinear, numeric solutions differ considerably. In addition to numeric streamlines being shifted downstream of the linear, analytic streamlines (which is partially due to non-hydrostatic effects), the nonlinear slopes are also steeper. Because the numerical results are limited by computational constraints, it is impossible to see from these results whether the inertial-gravity waves propagate far downstream as they do in the analytical solution.

Figure 23 shows the spanwise velocity calculated for two layers of uniformly stratified flow with a tropopause height of  $H = 6.5$  km. The top figure shows the linear, hydrostatic, analytic response and the lower figure shows the fully numeric, nonlinear solution. Qualitatively the results show that the nonlinear response in the troposphere is much stronger than the corresponding linear response. This is consistent with the large nonlinear forcing coefficients in the troposphere of the analytic solution.

Figure 24 provides a more quantitative comparison of the spanwise velocity for the linear an

(a)



(b)

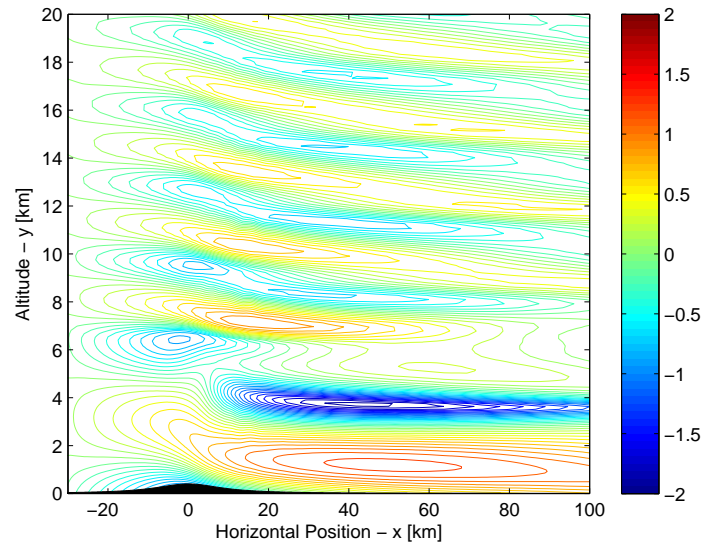


Figure 23: Spanwise velocity profile obtained from (a) the linear, analytic solution (b) the nonlinear, numeric solution for parameters given in Figure 22.

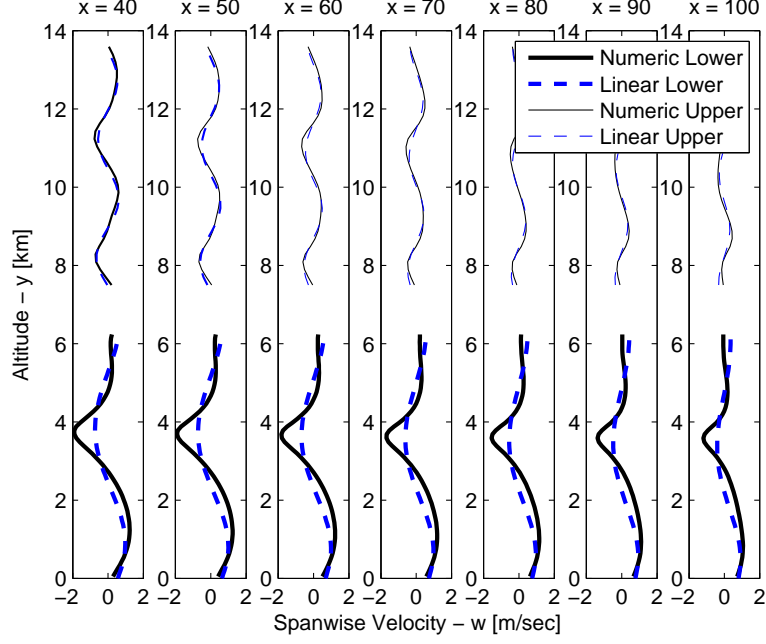


Figure 24: Spanwise velocity as a function of altitude for several locations downstream of the topography for parameters given in Figure 22. Dimensions of downstream locations are in kilometers, i.e 40 km, 50 km, etc.

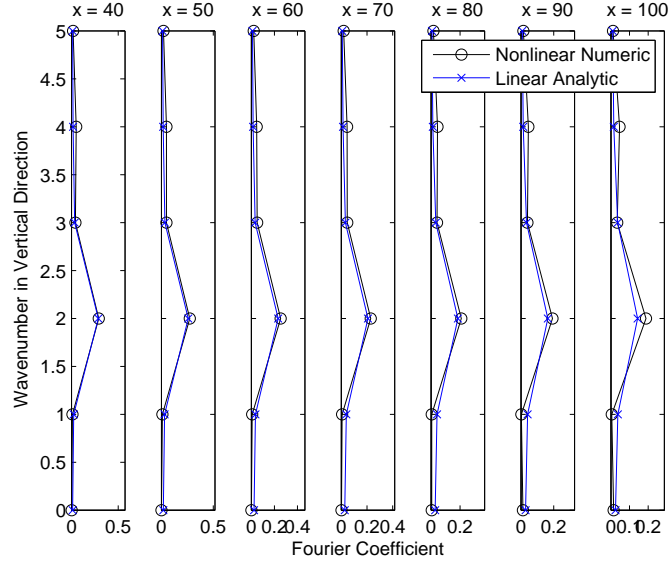
nonlinear cases. In the figure, the vertical profile of spanwise velocity is plotted at several stations downstream of the topography. Above the tropopause, there is very little difference between the linear and nonlinear solutions. However, below the troposphere, the nonlinear spanwise velocity is much larger (in magnitude) than the linear response, which is consistent with the qualitative observations made in Figure 23.

In order to make an even more detailed comparison between the linear and nonlinear solutions, the vertical spectrum of the spanwise velocity for both solutions was computed at several locations downstream of the topography. The results are shown in Figure 25. In the lower layer, the propagating component of the linear solution should have a vertical wavenumber of unity. For this case, the vertically propagating component of the linear solution in the stratosphere should have a vertical wavenumber of two because the Brunt–Väisälä frequency in the stratosphere is twice that in the troposphere. The linear spectra have strong peaks at the appropriate wavenumbers and are essentially zero for higher harmonics, which is consistent with the formulation of the linear solution given in (87). The forcing of the outer solution by nonlinearity in the inner solution gives rise to higher harmonics in the vertical, as formulated in (108). These higher harmonics are expressed using the Fourier coefficients  $\hat{l}_n^\pm(0)$  and  $\hat{m}_n^\pm(0)$ . The vertical spectra of spanwise velocity downstream of the topography in the troposphere show these higher harmonics. However, the spectra in the stratosphere do not. Again this is consistent with Figure 24 and indicates that the nonlinearity in the inner solution gives rise to higher harmonics in the troposphere that propagate far down-

stream, but the response in the stratosphere is largely unaffected by the nonlinearity for this particular tropopause height. A comprehensive study of the effects of tropopause altitude has not been done. It is possible that such a study would reveal tropopause heights giving rise to more pronounced nonlinearity in the stratosphere and less in the troposphere.



a.



b.

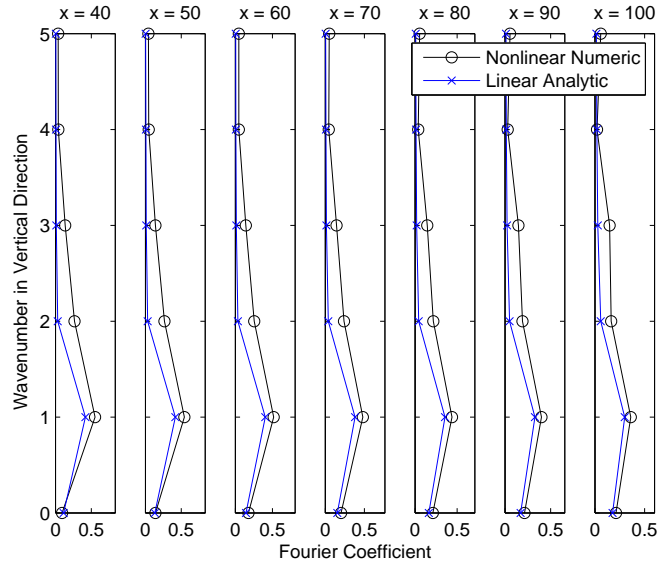


Figure 25: Vertical spectrum of spanwise velocity at several horizontal positions downstream of the topography for parameters given in Figure 22. Horizontal positions downstream of topography are given in kilometers, i.e 40 km, 50 km, etc. (a) Spectrum in the stratosphere. (b) Spectrum in the troposphere.

### 3 Effect of Unsteady Wind

#### 3.1 Introduction

The classic analyses of Queney [17] and Long [14] assume that flow of stratified fluid over topography is steady in time. Many of the subsequent studies have also used this assumption, and there are only a handful of investigations that account for unsteady wind in stratified flow over topography in the atmosphere. Among these are the theoretical works of Bell [4], Bannon and Zehnder [1] and Hines [9] and the numerical investigation of Lott and Teitelbaum [15]. More recently the effect of unsteady wind over topography has been examined by Skopovi [19]. Based on fully numerical simulations, Skopovi pointed out that slowly accelerated transient wind could produce streamlines that were significantly steeper than those for an impulsively started wind. In addition, his work showed that a monochromatic temporal fluctuation in wind speed could produce waves with larger amplitudes than those for a steady wind corresponding to the mean wind speed. Skopovi [19] used a fully numerical code to examine the effect of an oscillatory wind component,

$$U = U_0 (1 + \Delta \cos \omega t),$$

on nonlinear mountain waves. He noted that, for low background flow frequencies,  $\omega/N_0 = 0.1$ , say, ( $N_0$  is the buoyancy frequency), the nonlinear unsteady response may be amplified and can be dramatically different from the steady-state response corresponding to the mean wind  $U_0$ . This is illustrated in Fig. 26 below, which shows flow streamlines at  $t \approx 0.5$  hr and  $t \approx 2.2$  hr after the wind has been turned on. Note that, while the wind speed is equal to  $U_0 = 10$  m/sec at both these times, the response at  $t \approx 2.2$  hr is significantly stronger and quite different from the steady-state response.

These results call for a systematic study of the question: why does slowly varying wind matter? Qualitatively, the answer can be traced to the fact that the response in the hydrostatic limit ( $\mu = U_0/(NL) \ll 1$ ) evolves on a relatively long timescale  $t \sim L/(U_0\mu^2)$ . As a result, low-frequency wind oscillations can have an  $\mathcal{O}(1)$  effect, particularly in the nonlinear response. Moreover, as the group velocity vanishes in the frame of the mountain, the hydrostatic response is resonant, so small-amplitude wind oscillations,  $\Delta = \mathcal{O}(\mu^2)$ , can have an  $\mathcal{O}(1)$  effect as well. In this investigation we present an analytic theory for stratified flow over topography in the presence of an unsteady background flow along with some fully numeric computational results.

#### 3.2 Governing Equations

The asymptotic theory of Kantzios and Akylas [10], hereafter referred to as KA, generalizes Long's solution to account for slow temporal variations and weak spatial variations in upstream wind speed and Brunt–Väisälä frequency. The theory of KA is analogous to that of Grimshaw and Yi [8], who examined the case of a finite depth flow over topography. KA gives the leading-order streamfunction disturbance as

$$\psi = y + (Ae^{iy} + \text{c.c.}) \quad (114)$$

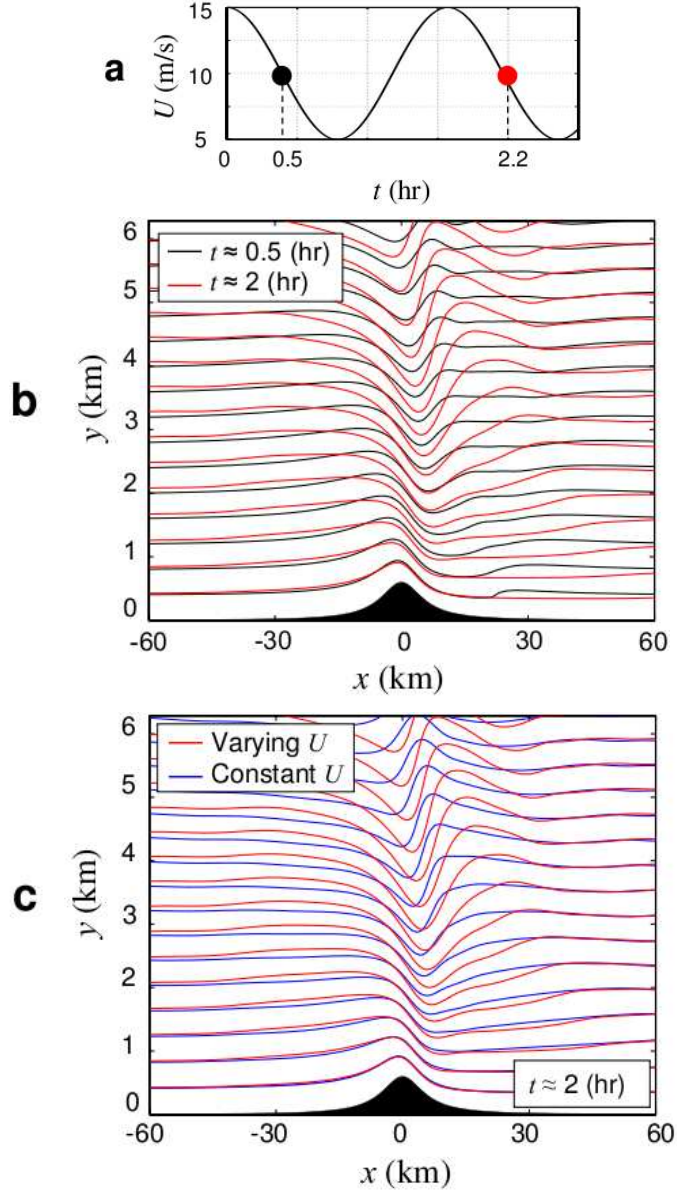


Figure 26: Previous numerical results of Skopovi [19] depicting response streamlines due to slowly fluctuating wind of the form  $U = U_0 (1 + \Delta \cos \omega t)$ , where  $U_0 = 10$  m/s,  $\Delta = 0.5$  and  $\omega/N_0 = 0.1$ , over topography of peak height  $h = 0.6$  km. (a) Fluctuation of free-stream flow in time. Results in Fig. 2.b are both at times when the free-stream velocity is at 10 m/s but are separated by one period of fluctuating free-stream velocity. (b) Comparison of transient response at two different times, which both correspond to a free-stream velocity of 10 m/s. Despite the free-stream velocity being the same in both cases, the streamlines differ significantly, indicating the importance of the fluctuating component of the wind. (c) A comparison of the transient response for a fluctuating wind to the steady-state response for a steady wind given by Long's solution. The results show that wave amplitudes forced by the transient wind can be significantly larger than those obtained in the steady-state solution for a steady wind. This unsteady wind may lead to wave breaking at mountain heights smaller than those predicted by Long's steady-state solution.

where  $A$  is the complex amplitude function

$$A = a(x, Y, T) + ib(x, Y, T) \quad (115)$$

and time and altitude have been scaled with the square of the longwave parameter,  $\mu \equiv \frac{U_0}{N_0 L_0} \ll 1$  as

$$\begin{aligned} T &= \mu^2 t \\ Y &= \mu^2 y \end{aligned} \quad (116)$$

where  $y$  and  $t$  are the nondimensional altitude and time defined previously. Then the complex amplitude is governed by a system of Volterra integral equations. Upon taking one derivative with respect to  $x$  of the first-kind formulation given in KA, the evolution equations become Volterra equations of the second kind given by

$$\begin{aligned} K_{11}^c a_T + K_{12}^c b_T + \int_{-\infty}^x dx' (K_{11x} a_T' + K_{12x} b_T') - \frac{1}{2} \alpha^2 a_{xxx} + b_{xY} &= 0 \\ K_{21}^c a_T + K_{22}^c b_T + \int_{-\infty}^x dx' (K_{21x} a_T' + K_{22x} b_T') - \frac{1}{2} \alpha^2 b_{xxx} - a_{xY} &= 0 \end{aligned} \quad (117)$$

where the kernels,  $K_{ij}$  are in general nonlinear functions of the complex amplitude,  $A = a + ib$ , and are given in Appendix F. The evolution equations are subject to the kinematic boundary condition at the surface of the topography requiring that the curve of topography be a streamfunction. Doing so gives the boundary condition

$$a \cos \epsilon f - b \sin \epsilon f = -\frac{1}{2} \epsilon f \quad (118)$$

where  $y = \epsilon f(x, T)$  is the curve defining the topography.

Following the work of Bell [4], we transform the governing equation from one in which the mountain is fixed and the wind unsteady to one in which the wind is steady and the mountain oscillates. Assuming a spatially uniform, undisturbed wind of the form

$$U = U_0 (1 + \mu^2 \Delta \cos \Omega T) \quad (119)$$

where  $U_0$  is the temporally averaged wind speed,  $\Delta$  is an amplitude of order unity and  $\Omega$  the frequency of order unity. Because  $\mu \ll 1$ , the wind is nearly constant in time with a very small fluctuating component. The frequency  $\Omega$  multiplies the stretched time,  $T$ , so despite  $\Omega = \mathcal{O}(1)$ , the frequency in unstretched coordinates is very small ( $\mu^2 \Omega$ ). The combination of a small amplitude wind oscillation at low frequency can give a leading-order disturbance. In the transformed coordinates where the wind is steady, this corresponds to the mountain having an amplitude of oscillation of order unity.

We define a new horizontal coordinate,  $\xi$ , for which the wind is steady and the topography oscillates. For an unsteady wind of the form (119), the transformation is

$$\xi = x + \frac{\Delta}{\Omega} \sin \Omega T \quad (120)$$

where the amplitude of the mountain oscillations in the steady wind coordinate system is  $\frac{\Delta}{\Omega} = \mathcal{O}(1)$ , which leads to a large-amplitude unsteady response despite the small-amplitude oscillations of wind in the original coordinate system. In this new coordinate system, the curve defining the topography becomes

$$y = \epsilon f(x, T) = \epsilon f(\xi) = \epsilon \begin{cases} e^{-\xi^2}, & \text{(Gaussian)} \\ \frac{1}{1 + \xi^2}, & \text{(Witch of Agnesi)} \end{cases} \quad (121)$$

### 3.3 Linear Limit

In the limit as the amplitude of the topography goes to zero,  $\epsilon \rightarrow 0$ , the matrix of kernels in (117) reduces to the diagonal matrix as

$$K_{11}, K_{22} \rightarrow 1, \quad K_{12}, K_{21} \rightarrow 0 \text{ as } \epsilon \rightarrow 0 \quad (122)$$

In this limit, the evolution equations are

$$\left. \begin{aligned} a_T - \frac{1}{2}\alpha^2 a_{\xi\xi\xi} + b_{\xi Y} &= 0 \\ b_T - \frac{1}{2}\alpha^2 b_{\xi\xi\xi} - a_{\xi Y} &= 0 \end{aligned} \right\}, \quad \epsilon \rightarrow 0 \quad (123)$$

subject to the linearized boundary condition

$$a = -\frac{1}{2}\epsilon f(\xi), \quad Y = 0, \epsilon \rightarrow 0 \quad (124)$$

If we further make the assumption that the response is hydrostatic, then the dispersive terms,  $a_{\xi\xi\xi}$  and  $b_{\xi\xi\xi}$  become zero and complex amplitude,  $A$ , can be written as an inverse Fourier transform as

$$A = -\epsilon \int_{\frac{Y}{T}}^{\infty} \hat{f}(k) e^{ikx} \exp \left[ ik \frac{\Delta}{\Omega} \sin \left( -\frac{\Omega}{k} Y + \Omega T \right) \right] dk, \quad \mu, \epsilon \rightarrow 0 \quad (125)$$

Skopovi [19] has also derived an alternate linear solution for the non-hydrostatic, steady-in-the-mean flow over topography. The solution incorporates dispersive effects and neglects the initial wave propagation in the transition from an undisturbed flow to the oscillatory flow over topography. Rather, the solution gives the oscillatory flow over topography once it has reached a periodic state. The solution is

$$\psi = \int_{-\infty}^{\infty} \hat{f}(k) \sum_{n=-\infty}^{\infty} \frac{-(k + \omega_0 + n)}{k} e^{imy} J_n \left( \frac{k\Delta}{\omega_0} \right) \exp i \left[ kx + my - \frac{k\Delta}{\omega_0} \sin(\omega_0 t) + \omega_0 n t \right] dk \quad (126)$$

where  $\omega_0$  is the frequency in the unstretched time domain,  $t$ , and the vertical wavenumber,  $m$ , is chosen to satisfy boundedness and the radiation condition, and is given as

$$m = \begin{cases} i \left| \frac{k}{k + \omega_0 n} \right| \sqrt{\mu^2 (k + \omega_0 n)^2 - N^2}, & \frac{N^2}{(k + \omega_0 n)^2} - \mu^2 < 0 \\ \frac{|k|}{k + \omega_0 n} \sqrt{N^2 - \mu^2 (k + \omega_0 n)^2}, & \frac{N^2}{(k + \omega_0 n)^2} - \mu^2 > 0 \end{cases} \quad (127)$$

### 3.4 Nonlinear Asymptotic Solution

For the general case of a finite-amplitude topography, the matrix of kernels does not reduce to the diagonal matrix. For weakly nonlinear solutions, the kernels can be evaluated analytically through asymptotic expansion of (114). However, at the limit of wave breaking when the streamlines become vertical, the kernels become singular. As this limit is approached, the kernels must be evaluated numerically. In addition to the presence of the off-diagonal kernels and the  $x$ -derivatives of the kernels in the integrals, the fully nonlinear problem differs from the linear problem in that the boundary condition must be applied along the contour of the topography as in (118), rather than at  $y = 0$ , as in (124). Several numerical methods have been investigated for the integration of these nonlinear evolution equations. Most notable among them was the modified Lax-Wendroff method employed by Prasad and Akylas [16]. However, in each of the methods tried, grid-scale oscillations appeared for topography of amplitude greater than approximately  $\epsilon = 0.50$ . These grid-scale oscillations generally appeared after approximately one quarter of the period of oscillation of the wind, which was on the order of one hundred computational timesteps. These grid-scale oscillations were not seen for smaller-amplitude topography. The method of filtering used by Prasad and Akylas [16] was implemented in an attempt to eliminate these grid-scale fluctuations. However, mild filtering was unable to adequately eliminate these erroneous oscillations, and work on their elimination for larger-amplitude topography is ongoing.

Figure 27 shows a streamlines for unsteady flow over topography for a nondimensional mountain amplitude of  $\epsilon = 0.5$  and amplitude of wind oscillation that is 18 percent of the mean wind speed of 10 m/s. A comparison of five different solutions is presented. The solution labeled “Linear Long’s” is Long’s solution for steady wind in the linear limit. The solution labeled “Long’s” is Long’s solution for steady wind over finite-amplitude topography. The solution labeled “CFD” is the fully numeric solution obtained by integrating the governing equations for the primitive variables ( $u$ ,  $v$ ,  $\rho$  and  $p$ ) in time. The solution labeled “Asymptotics” is the integration of the governing equations given in (117) subject to the boundary condition (118). Finally, the solution labeled “Linear Asymptotics” is the solution to the linearized governing equations in (123) subject to the linearized boundary condition (124).

Above the topography, the agreement between the asymptotic theory of KA and the computational solution is reasonably good. Downstream and aloft, the fully numeric solution exhibits waves of wavelength approximately 12 km. For this relatively small-amplitude topography ( $\epsilon = 0.50$ ), the unsteady streamlines do not appear to be significantly steeper than

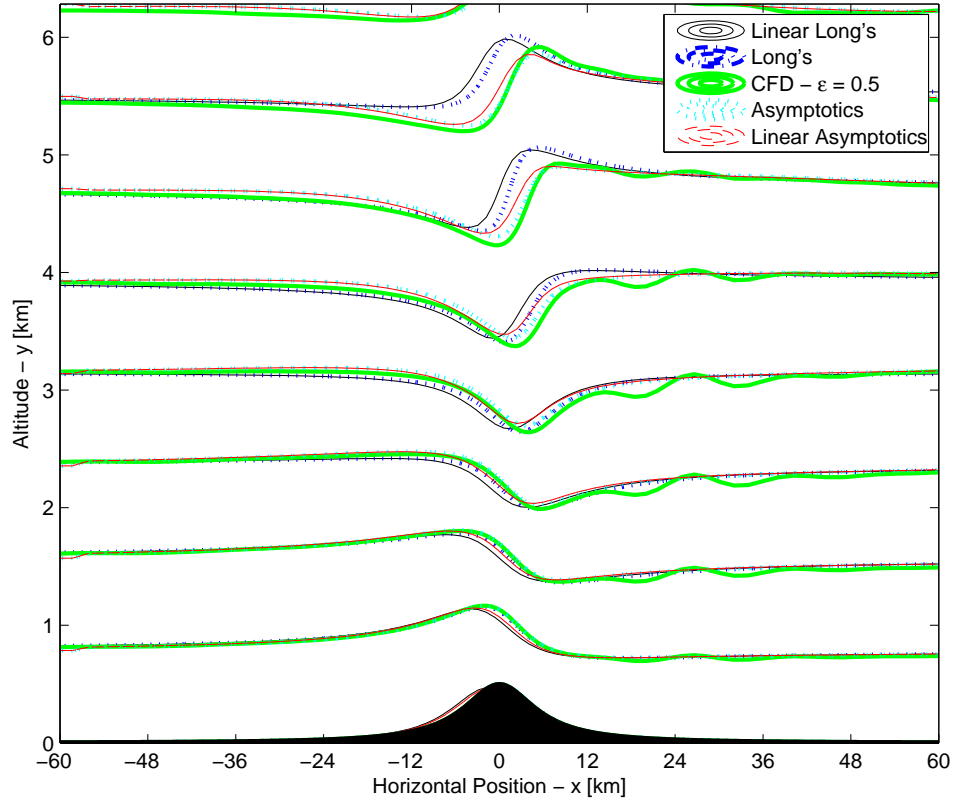


Figure 27: Streamlines for unsteady flow over topography.  $\mu = \frac{1}{6}$ .  $\epsilon = 0.5$ .  $\Delta = \Omega = 6.7858$ . Computational time  $t_{\text{computational}} = 250$ .

those for the steady flow of Long's solution. However, they are considerably steeper than the corresponding linear streamlines, suggesting that as the amplitude of the topography increases, the nonlinear effect of unsteadiness increases. Extrapolating this, it is plausible that slightly unsteady wind can produce significantly steeper streamlines, as shown by Skopovi [19].

Despite not having an asymptotic solution for larger amplitudes, numerical simulations have been done for unsteady wind over mountains with amplitudes larger than  $\epsilon = 0.50$ . Figure 28 shows streamlines for the fully numeric simulation of stratified flow over topography with unsteady upstream wind. The parameters are the same as those in the previous case with the exception that the mountain height is now  $h_0 = 0.73$  km, corresponding to a nondimensional amplitude of  $\epsilon = 0.73$  for characteristic wind speed  $U_0 = 10$  m/s and Brunt–Väisälä frequency  $N_0 = 0.01$  sec<sup>-1</sup>. The results show that the nonlinear response with weak fluctuations in upstream wind speed is significantly stronger than that predicted by Long's solution for steady wind. In particular, the streamline at approximately  $x = 10$  km,  $y = 4$  km is quite steep compared to Long's solution. This suggests that the critical amplitude for wave breaking for the unsteady wind is smaller than the critical amplitude for wave breaking for the steady Long's solution.



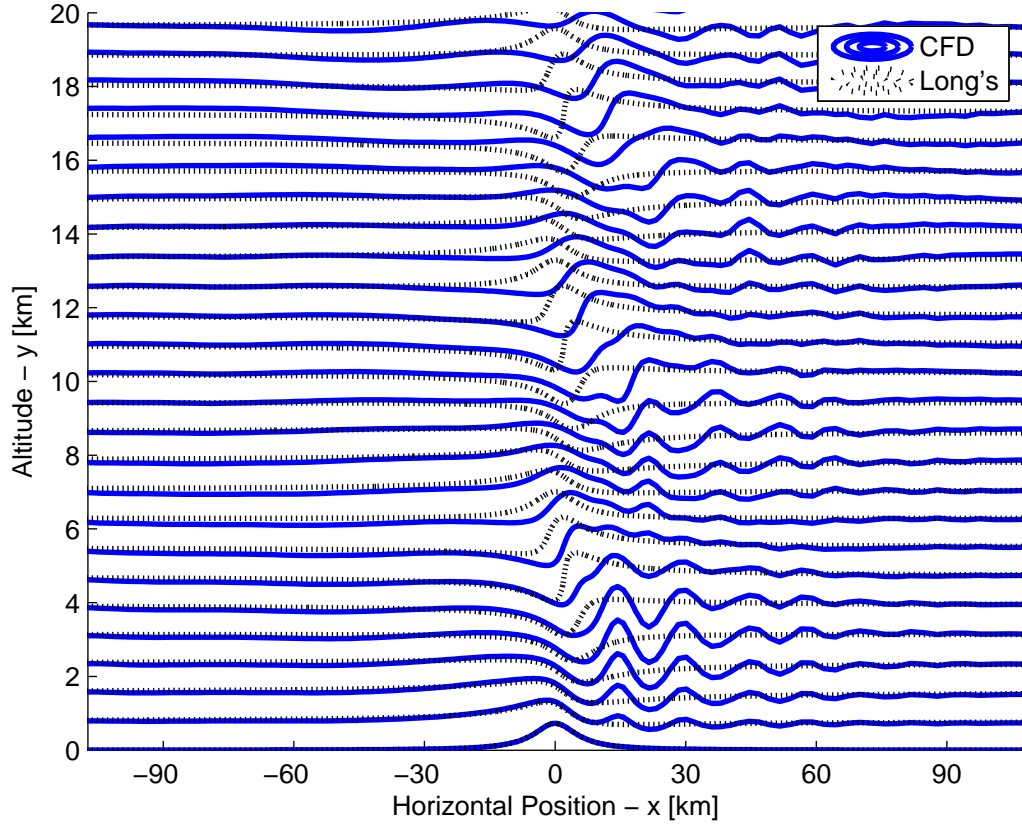


Figure 28: Streamlines for unsteady flow over topography.  $\mu = \frac{1}{6}$ .  $\epsilon = 0.73$ .  $\Delta = \Omega = 6.7858$ . Computational time  $t_{\text{computational}} = 450$ .

## 4 Conclusions

- In stratified flow over topography, rotation behaves as a singular perturbation when  $Ro \gg 1$ . For mountains of width less than approximately  $L = 50$  km, Coriolis forces do not have sufficient time to act on the flow as it passes over the mountain. However, far downstream of the mountain, rotation becomes as important as stratification because the Coriolis force has sufficient time to act upon the flow. The results of §1 show the effect of rotation far downstream of topography for large Rossby number.
- A matched asymptotic expansion has been developed for nonlinear stratified flow over topography in the limit  $Ro \gg 1$ . The inner region of the domain is near the mountain horizontally and extending upward indefinitely. In this region, rotation is a weak perturbation and the leading-order solution is that of Long. The outer region of the domain is far from the topography:  $x \gg \frac{U_0}{f}$ . Here the solution is linear but the rotation, in addition to stratification, is of leading-order importance. The matching process shows that nonlinear interaction in the inner solution give rise to higher-harmonic oscillations that propagate far downstream of the topography.
- Nonlinear interactions above the mountain give rise to steady, higher-harmonic gravity–inertial waves far downstream. The effect of nonlinearity for a single layer is most clearly seen in comparing the linear spanwise velocity shown in Figure 8 with the corresponding nonlinear spanwise velocity depicted in Figure 9. The structure of the spanwise velocity for the nonlinear case shows closed contours indicative of higher harmonics in the vertical direction. These higher harmonics are the signature of the nonlinear interactions above the topography. For the single layer, these nonlinear interactions are relatively weak because Long’s solution (with the nonlinear boundary condition) does not differ appreciably from the linear limit of Long’s solution. Thus nonlinear interactions are relatively weak and the higher harmonics far downstream are relatively weak for the single-layer model of the atmosphere. The effect becomes stronger when the tropopause is taken into account.
- The asymptotic theory has been qualitatively validated via comparison with fully numeric simulations of stratified flow on an  $f$ –plane. In particular, the simulations for two layers of uniformly stratified flow show the presence of higher harmonics. This can be seen in the vertical spectrum of spanwise velocity in Figure 25. However, comparison of the analytic theory with these numeric simulations is imperfect. In order to compare with the asymptotic theory, the numeric simulations should give steady-state solutions far downstream of the topography. Because of limits in computational resources, a steady-state solution is only obtained for relatively short distances downstream ( $x < 900$  km), preventing a good comparison with the analytical results. Nevertheless, the higher harmonics in the spanwise velocity shown in Figure 25 suggest that nonlinear interactions above the topography are significant and do give rise to higher harmonics downstream of the topography.

Because the analytical results can be easily evaluated arbitrarily far downstream, the analytical theory provides a predictive model that is valuable when numerical simulations may be impractical due to computational limitations.

- The combined effect of the Earth's rotation and the tropopause is to enhance and extend the wave activity far downstream from the topography, as shown in §2. The effect of tropopause tuning for two different tropopause heights was examined in §2. For a tropopause height of  $H = 12.5$  km (based on a wind speed  $U_0 = 10$  m/s and Brunt–Väisälä frequencies of  $N_1 = 0.01 \text{ sec}^{-1}$  and  $N_2 = 0.02 \text{ sec}^{-1}$  in the troposphere and stratosphere, respectively) the response above the mountain had significantly larger streamline slopes and nonlinear interactions than the case with a tropopause height of  $H = 11.0$  km. These nonlinear interactions above the topography produced higher harmonics in the wavefield far downstream of the topography, as shown in Figures 18 and 19. In general, the tropopause height at which the response is tuned depends on the Brunt–Väisälä frequencies in the troposphere and stratosphere as well as on the velocity upstream of the topography.
- The response due to unsteady wind can be significantly stronger than the response due to steady wind. The analytic theory shows that, even for small fluctuations in wind speed, waves of significantly larger amplitude can be produced than those for a steady wind corresponding to the mean wind speed. The amplitude of the response is based on the ratio of the amplitude of fluctuation in wind speed,  $\Delta$ , to the frequency of the fluctuation,  $\Omega$ , as given in Eqn. (119). Thus for low-frequency, low-amplitude fluctuations, the unsteady response can be of order unity. This unsteady wind can cause wave breaking at lower topography steepness. The previous numeric results of Skopovi 26 as well as the numeric results of the current study shown in Figures 27 and 28 confirm that an unsteady wind can produce steeper streamlines than the corresponding steady wind.

Future work includes the following:

- The preceding analysis of tropopause tuning only considered the comparison of two tropopause heights. The tuned case yielded a significantly amplified response in the troposphere, but the response in the stratosphere was not significantly enhanced by the nonlinearities. It is believed that other tropopause heights will yield larger nonlinearities, and a correspondingly larger-amplitude response in the stratosphere, and a less significant amplification in the troposphere. A search for tropopause heights producing amplified waves in the stratosphere, as opposed to the case shown in Figure 19 for which amplification occurs in the troposphere, will be done.
- Thus far, asymptotic results for unsteady wind for topographies of amplitude  $\epsilon > 0.5$  have not been obtained. The asymptotic model discussed in §3 will be used to study the effect of unsteady wind over steeper topographies. These results will be compared with the fully numeric simulations.
- The asymptotic model discussed in §3 is valid for slowly oscillating wind with small-amplitude oscillations. The current model will be extended to relax this restriction of small-amplitude wind oscillations, and a study of large-amplitude wind oscillations over finite-amplitude topography will be made.

## References

- [1] P. R. Bannon and J. A. Zehnder. Surface pressure and mountain drag for transient air-flow over a mountain ridge. *Journal of the Atmospheric Sciences*, 42(23):2454–2462, 1985.
- [2] J. B. Bell, P. Colella, and H. M. Glaz. A 2nd-order projection method for the incompressible navier stokes equations. *Journal of Computational Physics*, 85(2):257–283, 1989.
- [3] J. B. Bell and D. L. Marcus. A 2nd-order projection method for variable-density flows. *Journal of Computational Physics*, 101(2):334–348, 1992.
- [4] T. H. Bell. Lee waves in stratified flows with simple harmonic time-dependence. *Journal of Fluid Mechanics*, 67(FEB25):705–722, 1975.
- [5] K. S. Davis. *Flow of Nonuniformly Stratified Fluid of Large Depth over Topography*. M.S. Thesis. Mechanical Engineering, MIT, Cambridge, MA, USA, 1999.
- [6] D. R. Durran. 2-layer solutions to long’s equation for vertically propagating mountain waves - how good is linear-theory. *Quarterly Journal of the Royal Meteorological Society*, 118(505):415–433, 1992.
- [7] Dale R. Durran. *Numerical Methods for Wave Equations in Geophysical Fluid Dynamics*. Springer, New York, 1999.
- [8] R. Grimshaw and Z. X. Yi. Resonant generation of finite-amplitude waves by the flow of a uniformly stratified fluid over topography. *Journal of Fluid Mechanics*, 229:603–628, 1991.
- [9] C. O. Hines. Modulated mountain waves. *Journal of the Atmospheric Sciences*, 52(5):602–606, 1995.
- [10] Y. D. Kantzios and T. R. Akylas. An asymptotic theory of nonlinear stratified flow of large depth over topography. *Proceedings of the Royal Society of London Series a-Mathematical Physical and Engineering Sciences*, 440(1910):639–653, 1993.
- [11] J. B. Klemp and D. K. Lilly. Dynamics of wave-induced downslope winds. *Journal of the Atmospheric Sciences*, 32(2):320–339, 1975.
- [12] P. K. Kundu and I. M. Cohen. *Fluid Mechanics*. Elsevier Academic Press, London, 2004.
- [13] M. J. Lighthill. *Introduction to Fourier Analysis and Generalized Functions*. Cambridge University Press, Cambridge, 1958.
- [14] R. R. Long. Some aspects of the flow of stratified fluids. i. a theoretical investigation. *Tellus*, 1953.
- [15] F. Lott and H. Teitelbaum. Topographic waves generated by a transient wind. *Journal of the Atmospheric Sciences*, 50(16):2607–2624, 1993.

- [16] D. Prasad and T. R. Akylas. Wave trapping and upstream influence in stratified flow of large depth. *Journal of Fluid Mechanics*, 491:301–324, 2003.
- [17] P. Queney. The problem of air flow over mountains: A summary of theoretical results. *Bulletin of the American Meteorological Society*, 29:16–26, 1948.
- [18] I. Skopovi. *A Model for Nonlinear Gravity Waves in Stratified Flows*. M.S. Thesis. Mechanical Engineering, MIT, Cambridge, MA, USA, 2002.
- [19] I. Skopovi. *The Role of Background Flow Variations in Stratified Flows over Topography*. Doctoral Thesis. Mechanical Engineering, MIT, Cambridge, MA, USA, 2006.
- [20] I. Skopovi and T. R. Akylas. The role of buoyancy-frequency oscillations in the generation of mountain gravity waves. *Theoretical and Computational Fluid Dynamics*, 21(6):423–433, 2007.
- [21] R. B. Smith. Synoptic observations and theory of orographically disturbed wind and pressure. *Journal of the Atmospheric Sciences*, 39(1):60–70, 1982.
- [22] J. Trub and H. C. Davies. Flow over a mesoscale ridge - pathways to regime transition. *Tellus Series a-Dynamic Meteorology and Oceanography*, 47(4):502–524, 1995.

### III. APPENDICES

#### A Inner Limit of Outer Solution

The outer solution is

$$\begin{aligned}\tilde{\psi} &= -2\epsilon\hat{h}(0) \Re \left\{ \int_0^1 \exp\left(\frac{-\tilde{k}y}{\sqrt{1-\tilde{k}^2}}\right) e^{i\tilde{k}\tilde{x}} d\tilde{k} + \int_1^\infty \exp\left(\frac{i\tilde{k}y}{\sqrt{\tilde{k}^2-1}}\right) e^{i\tilde{k}\tilde{x}} d\tilde{k} \right\} \\ \tilde{w} &= -2\epsilon\hat{h}(0) \Re \left\{ \int_0^1 \frac{ie^{i\tilde{k}\tilde{x}}}{\sqrt{1-\tilde{k}^2}} \exp\left(\frac{-\tilde{k}y}{\sqrt{1-\tilde{k}^2}}\right) d\tilde{k} + \int_1^\infty \frac{e^{i\tilde{k}\tilde{x}}}{\sqrt{\tilde{k}^2-1}} \exp\left(\frac{i\tilde{k}y}{\sqrt{\tilde{k}^2-1}}\right) d\tilde{k} \right\}\end{aligned}\quad (128)$$

Defining the four integrals in the solution as

$$\begin{aligned}I_1 &\equiv \Re \left\{ \int_0^1 \exp\left(\frac{-\tilde{k}y}{\sqrt{1-\tilde{k}^2}}\right) e^{i\tilde{k}\tilde{x}} d\tilde{k} \right\} \\ I_2 &\equiv \Re \left\{ \int_1^\infty \exp\left(\frac{i\tilde{k}y}{\sqrt{\tilde{k}^2-1}}\right) e^{i\tilde{k}\tilde{x}} d\tilde{k} \right\} \\ I_3 &\equiv \Re \left\{ \int_0^1 \frac{ie^{i\tilde{k}\tilde{x}}}{\sqrt{1-\tilde{k}^2}} \exp\left(\frac{-\tilde{k}y}{\sqrt{1-\tilde{k}^2}}\right) d\tilde{k} \right\} \\ I_4 &\equiv \Re \left\{ \int_1^\infty \frac{e^{i\tilde{k}\tilde{x}}}{\sqrt{\tilde{k}^2-1}} \exp\left(\frac{i\tilde{k}y}{\sqrt{\tilde{k}^2-1}}\right) d\tilde{k} \right\}\end{aligned}\quad (129)$$

such that  $\tilde{\psi} = -2\epsilon\hat{h}(0) (I_1 + I_2)$  and  $\tilde{w} = -2\epsilon\hat{h}(0) (I_3 + I_4)$ . Then the limit of  $I_1$  is

$$\lim_{\tilde{x} \rightarrow 0} I_1 = \int_0^\infty \exp\left(\frac{-\tilde{k}y}{\sqrt{1-\tilde{k}^2}}\right) d\tilde{k} = \mathcal{O}(1) \text{ const}$$

For  $I_2$ , we make the transformation  $\sigma = \sqrt{\tilde{k}^2 - 1} |\tilde{x}|$  giving  $\tilde{k} = \frac{\sqrt{\sigma^2 + \tilde{x}^2}}{|\tilde{x}|}$  and  $d\tilde{k} = \frac{1}{|\tilde{x}|} \frac{\sigma}{\sqrt{\sigma^2 + \tilde{x}^2}} d\sigma$ . Then

$$I_2 = \Re \left\{ \int_1^\infty \exp\left(\frac{i\tilde{k}y}{\sqrt{\tilde{k}^2-1}}\right) e^{i\tilde{k}\tilde{x}} d\tilde{k} \right\} = \Re \left\{ \frac{1}{|\tilde{x}|} \int_0^\infty \exp\left(\frac{i\sqrt{\sigma^2 + \tilde{x}^2}y}{\sigma}\right) e^{i\sqrt{\sigma^2 + \tilde{x}^2}\text{sgn}\tilde{x}} \frac{\sigma}{\sqrt{\sigma^2 + \tilde{x}^2}} d\sigma \right\}$$

Taking the limit as  $\tilde{x} \rightarrow 0$  gives

$$\lim_{\tilde{x} \rightarrow 0} I_2 = \Re \left\{ \frac{1}{|\tilde{x}|} \int_0^\infty \exp(iy) e^{i\sigma\text{sgn}\tilde{x}} d\sigma \right\} = \frac{1}{|\tilde{x}|} \cos y \int_0^\infty \cos \sigma d\sigma - \frac{1}{\tilde{x}} \sin y \int_0^\infty \sin \sigma d\sigma$$

Using the theory of generalized functions [13], we rewrite these integrals as

$$\begin{aligned}\int_0^\infty \cos \sigma d\sigma &= \lim_{\epsilon \rightarrow 0} \int_0^\infty e^{-\epsilon\sigma} \cos \sigma d\sigma = 0 \\ \int_0^\infty \sin \sigma d\sigma &= \lim_{\epsilon \rightarrow 0} \int_0^\infty e^{-\epsilon\sigma} \sin \sigma d\sigma = 1\end{aligned}$$

finally giving

$$I_2 \sim -\frac{\sin y}{\tilde{x}} \quad (\tilde{x} \rightarrow 0)$$

and

$$\left. \begin{aligned}\tilde{\psi} &\sim 2\epsilon\hat{h}(0) \frac{\sin y}{\tilde{x}} \\ \tilde{u} &\sim 2\epsilon\hat{h}(0) \frac{\cos y}{\tilde{x}} \\ \tilde{v} &\sim 2\epsilon\hat{h}(0) \frac{\sin y}{\tilde{x}^2}\end{aligned}\right\} \quad (\tilde{x} \rightarrow 0) \quad (130)$$

The limit of  $I_3$  as  $\tilde{x} \rightarrow 0$  is

$$\lim_{\tilde{x} \rightarrow 0} I_3 = \Re \left\{ i \int_0^1 \frac{1}{\sqrt{1-\tilde{k}^2}} \exp \left( \frac{-\tilde{k}y}{\sqrt{1-\tilde{k}^2}} \right) d\tilde{k} \right\} = 0$$

In finding the limit of  $I_4$  as  $\tilde{x} \rightarrow 0$ , the same transformation is made as for  $I_2$ . Then

$$I_4 = \Re \left\{ \int_0^\infty \frac{e^{i\sqrt{\sigma^2 + \tilde{x}^2} \text{sgn} \tilde{x}}}{\sqrt{\sigma^2 + \tilde{x}^2}} \exp \left( \frac{i\sqrt{\sigma^2 + \tilde{x}^2} y}{\sigma} \right) d\sigma \right\}$$

and its limit as  $\tilde{x} \rightarrow 0$  is

$$\begin{aligned}\lim_{\tilde{x} \rightarrow 0} I_4 &= \Re \left\{ \int_0^\infty \frac{e^{i\sigma \text{sgn} \tilde{x}}}{\sqrt{\sigma^2 + \tilde{x}^2}} \exp(iy) d\sigma \right\} \\ &= \cos y \int_0^\infty \frac{\cos \sigma}{\sqrt{\sigma^2 + \tilde{x}^2}} d\sigma - \text{sgn} \tilde{x} \sin y \int_0^\infty \frac{\sin \sigma}{\sqrt{\sigma^2 + \tilde{x}^2}} d\sigma \\ &= \cos y K_0(\tilde{x}) - \text{sgn} \tilde{x} \sin y \int_0^\infty \frac{\sin \sigma}{\sqrt{\sigma^2 + \tilde{x}^2}} d\sigma\end{aligned}$$

where  $K_0$  is the modified Bessel function of the second kind. The asymptotic behavior of the modified Bessel function of the second kind is

$$K_0(\tilde{x}) = \ln \frac{2}{|\tilde{x}|} - \gamma + \mathcal{O}(\tilde{x}^2), \quad \tilde{x} \rightarrow 0$$

Taking the limit of the second integral in  $I_4$  as  $\tilde{x} \rightarrow 0$  gives

$$\lim_{\tilde{x} \rightarrow 0} \int_0^\infty \frac{\sin \sigma}{\sqrt{\sigma^2 + \tilde{x}^2}} d\sigma = \int_0^\infty \frac{\sin \sigma}{\sigma} d\sigma = \frac{\pi}{2}$$

Thus

$$I_4 \sim -\cos y \ln |\tilde{x}| - \frac{\pi}{2} \operatorname{sgn} \tilde{x} \sin y \quad (\tilde{x} \rightarrow 0)$$

and

$$\tilde{w} \sim 2\epsilon \hat{h}(0) \cos y \ln |\tilde{x}| + \pi \epsilon \hat{h}(0) \sin y \operatorname{sgn} \tilde{x} \quad (\tilde{x} \rightarrow 0) \quad (131)$$

The  $\operatorname{sgn} \tilde{x}$  function results in a jump in the spanwise velocity  $\tilde{w}$  across  $\tilde{x} = 0$ , giving

$$\tilde{w}|_{\tilde{x} \rightarrow 0^+} - \tilde{w}|_{\tilde{x} \rightarrow 0^-} = 2\pi \epsilon \hat{h}(0) \sin y = \sin y \int_{-\infty}^\infty h(x) dx \quad (132)$$



## B Matching: Jump in Spanwise Velocity due to Inner Solution

The leading order spanwise velocity in the inner solution is

$$\begin{aligned}
 w^{(0)}(x, \Psi^{(0)}) &= C(\Psi^{(0)}) - 2 \left[ \sin \Psi^{(0)} \int_0^x a(x') dx' + \cos \Psi^{(0)} \int_0^x b(x') dx' \right] \\
 &+ \sum_{n=1}^{\infty} n \left[ \cos n \Psi^{(0)} \int_0^x r_n(x') dx' - \sin n \Psi^{(0)} \int_0^x s_n(x') dx' \right]
 \end{aligned} \tag{133}$$

We would like to determine the jump in spanwise velocity in going from  $x \rightarrow -\infty$  to  $x \rightarrow \infty$ . This jump will be necessary in order to match the inner solution with the outer solution. We start by analyzing the behavior of the integral containing  $b(x)$ . From the radiation condition,  $b(x) = \mathcal{H}\{a(x)\}$  where  $\mathcal{H}$  is the Hilbert transform. Then

$$\begin{aligned}
 \int_0^x b(x') dx' &= \int_0^x \mathcal{H}\{a(x')\} dx' \\
 &= - \int_0^x \left\{ i \int_0^{\infty} \hat{a}(k) e^{ikx'} dk + c.c \right\}
 \end{aligned}$$

Switching the order of integration

$$\int_0^x b(x') dx' = - \left\{ i \int_0^{\infty} dk \hat{a}(k) \int_0^x e^{ikx'} dx + c.c \right\}$$

and evaluating the integral with respect to  $x'$  gives

$$\begin{aligned}
 \int_0^x b(x') dx' &= - \left\{ \int_0^{\infty} \hat{a}(k) \frac{(e^{ikx} - 1)}{k} dk + c.c \right\} \\
 &= - \left\{ i \int_0^{\infty} \hat{a}(k) \frac{\sin kx}{k} dk + c.c \right\} - \left\{ \int_0^{\infty} \hat{a}(k) \frac{(\cos kx - 1)}{k} dk + c.c \right\} \\
 &= - \left\{ i \int_0^{\infty} \hat{a}(k) \frac{\sin kx}{k} dk + c.c \right\} + 2 \left\{ \int_0^{\infty} \hat{a}(k) \frac{\sin^2 \frac{kx}{2}}{k} dk + c.c \right\}
 \end{aligned}$$

The first integrand is odd in  $x$  and the second term even in  $x$ . Looking at the integral from  $-\infty$  to  $\infty$ , the even integrand vanishes and we are left with

$$\int_{-\infty}^{\infty} b(x') dx' = -2i \int_0^{\infty} \hat{a}(k) \frac{\sin kx}{k} dk + c.c. = 0$$

because each of the conjugates is purely imaginary. Thus the term containing  $b(x)$  does not contribute to a finite jump across the topography in going from  $x \rightarrow -\infty$  to  $x \rightarrow \infty$ . Then we are left with a finite jump in the spanwise velocity given by

$$w^{(0)} \Big|_{-\infty}^{\infty} = -4\pi \hat{a}(0) \sin \Psi^{(0)} + 2\pi \sum_{n=1}^{\infty} n \left( \hat{r}_n(0) \cos n \Psi^{(0)} - \hat{s}_n(0) \sin n \Psi^{(0)} \right) \tag{134}$$

## C Details of Matching - Single Layer

In order to match the outer solution to the inner solution, we first scale the leading order outer solution by  $\frac{-2\hat{a}(0)}{\epsilon\hat{h}(0)}$ , which is unity in the linear limit where  $a(x) = -\frac{1}{2}\epsilon h(x)$ . Then the outer solution becomes

$$\begin{aligned}\tilde{\psi} &= 4\hat{a}(0) \Re\{I_1 + I_2\} \\ \tilde{w} &= 4\hat{a}(0) \Re\{I_3 + I_4\}\end{aligned}\tag{135}$$

with asymptotic behavior

$$\left. \begin{aligned}\tilde{\psi} &\sim -4\hat{a}(0) \frac{\sin y}{\tilde{x}} \\ \tilde{w} &\sim -4\hat{a}(0) \cos y \ln |\tilde{x}| = -4\hat{a}(0) \cos y \ln |x| - 4\hat{a}(0) \cos y \ln \beta\end{aligned}\right\} \tilde{x} \rightarrow 0$$

$$\tilde{w}|_{0-}^{0+} = -4\pi\hat{a}(0) \sin y$$

The  $\ln \beta$  term in the expression for  $\tilde{w}$  can be made to agree with the inner solution by defining the constant of integration in the inner solution as

$$C(\Psi^{(0)}) = -4\hat{a}(0) \cos y \ln \beta + D(\Psi^{(0)})$$

giving

$$\begin{aligned}w^{(0)} &= -4\hat{a}(0) \ln \beta \cos \Psi^{(0)} - 2 \left[ \sin \Psi^{(0)} \int_0^x a(x') dx' + \cos \Psi^{(0)} \int_0^x b(x') dx' \right] \\ &+ \sum_{n=1}^{\infty} n \left[ \cos n\Psi^{(0)} \int_0^x r_n(x') dx' - \sin n\Psi^{(0)} \int_0^x s_n(x') dx' \right] + D(\Psi^{(0)})\end{aligned}\tag{136}$$

At this point, the outer solution does not yet satisfy the required jump in spanwise velocity across the inner solution. This jump is induced by the higher harmonics,  $r_n(x)$  and  $s_n(x)$ . Thus we must add another component to the outer solution to achieve the necessary jump in spanwise velocity. We write

$$\begin{aligned}\tilde{\psi} &= 4\hat{a}(0) \Re\{I_1 + I_2\} + \tilde{\psi}_{II} \\ \tilde{w} &= 4\hat{a}(0) \Re\{I_3 + I_4\} + \tilde{w}_{II}\end{aligned}$$

where  $\tilde{\psi}_{II}$  and  $\tilde{w}_{II}$  must satisfy

$$\left. \begin{aligned}\tilde{\psi}_{II} &= o\left(\frac{1}{\tilde{x}}\right) \\ \tilde{w}_{II} &= o(\ln |\tilde{x}|)\end{aligned}\right\}, \tilde{x} \rightarrow 0$$

$$\tilde{w}_{II}|_{0-}^{0+} = 2\pi \sum_{n=1}^{\infty} n [\hat{r}(0) \cos ny - \hat{s}(0) \sin ny]$$

Since the outer problem is linear, we can superimpose solutions and separate  $\tilde{\psi}_{II}$  and  $\tilde{w}_{II}$  into vertical Fourier components as

$$\tilde{\psi}_{II} = \sum_{n=1}^{\infty} \tilde{\psi}^{(n)}$$

$$\tilde{w}_{II} = \sum_{n=1}^{\infty} \tilde{w}^{(n)}$$

such that each harmonic satisfies the appropriate matching conditions with the inner solution, namely

$$\left. \begin{aligned} \tilde{\psi}^{(n)} &= o\left(\frac{1}{\tilde{x}}\right) \\ \tilde{w}^{(n)} &= o(\ln |\tilde{x}|) \end{aligned} \right\}, \quad \tilde{x} \rightarrow 0$$

$$\tilde{w}^{(n)} \Big|_{0-}^{0+} = 2\pi n [\hat{r}(0) \cos ny - \hat{s}(0) \sin ny]$$

A new variable,  $\Phi^{(n)}$ , can be defined such that

$$\tilde{\Psi}^{(n)} = \Phi_x^{(n)}$$

$$\tilde{w}^{(n)} = \Phi_y^{(n)}$$

Then the governing equations in (66) can be written in terms of  $\Phi^{(n)}$  for  $n > 1$  as

$$\left(\Phi_{yy}^{(n)} + \Phi^{(n)}\right)_{\tilde{x}\tilde{x}} + \Phi_{yy}^{(n)} = 2\pi \left(n^2 - 1\right) \delta'(\tilde{x}) [\hat{r}_n(0) \sin ny + \hat{s}_n(0) \cos ny], \quad n > 1$$

subject to the boundary condition

$$\Phi^{(n)} = 0, \quad (y = 0, \tilde{x} \neq 0)$$

and the radiation condition. Taking the Fourier transform in the  $\tilde{x}$ -direction gives

$$(1 - k^2) \hat{\Phi}_{yy}^{(n)} - k^2 \hat{\Phi}^{(n)} = ik (n^2 - 1) [\hat{r}_n(0) \sin ny + \hat{s}_n(0) \cos ny], \quad n > 1$$

subject to

$$\hat{\Phi}^{(n)} = 0, \quad (y = 0)$$

The solution is then

$$\hat{\Phi}^{(n)} = \frac{ik}{k^2 - k_n^2} [\hat{r}_n(0) \sin ny + \hat{s}_n(0) \cos ny] + F(k) e^{im(k)y}, \quad n > 1$$

where

$$k_n \equiv \frac{n^2}{n^2 - 1} > 1$$

and the vertical wavenumber is

$$m(k) = \begin{cases} \frac{k}{\sqrt{k^2 - 1}}, & (|k| > 1) \\ i \frac{|k|}{\sqrt{1 - k^2}}, & (|k| < 1) \end{cases}$$

which is determined by the radiation condition. The boundary condition of zero streamline disturbance at  $y = 0$  requires

$$F(k) = -\frac{ik}{k^2 - k_n^2} \hat{s}_n(0)$$

Therefore, the solution is

$$\hat{\Phi}^{(n)} = \frac{ik}{k^2 - k_n^2} \left\{ \hat{r}_n(0) \sin ny + \hat{s}_n(0) [\cos ny - e^{im(k)y}] \right\}, n > 1 \quad (137)$$

In inverting the Fourier transform, care must be exercised because  $\hat{\Phi}^{(n)}$  has poles on the real axis at  $k = \pm k_n$ . The contours must be deformed in a manner consistent with the radiation condition in the horizontal direction. Since steady waves are observed downstream of the topography only, we require

$$c_g|_{\tilde{x}} \equiv \frac{\partial \omega}{\partial k} = 1 - \frac{|k|}{|m|} \frac{1}{\sqrt{k^2 + m^2}} > 0$$

Thus the integral is deformed beneath the poles giving

$$\begin{aligned} \Phi^{(n)} = & -2\pi \cos k_n \tilde{x} [\hat{r}_n(0) \sin ny + \hat{s}_n(0) \cos ny] H(\tilde{x}) \\ & + 2\hat{s}_n(0) \Im \left\{ \int_0^\infty \frac{k e^{ik\tilde{x}}}{k^2 - k_n^2} \exp\left(i \frac{ky}{\sqrt{k^2 - 1}}\right) dk \right\}, n > 1 \end{aligned}$$

Defining

$$\begin{aligned} I_5^{(n)} & \equiv \Im \left\{ \int_0^1 \frac{k e^{ik\tilde{x}}}{k^2 - k_n^2} \exp\left(-\frac{ky}{\sqrt{1 - k^2}}\right) dk \right\}, n > 1 \\ I_6^{(n)} & \equiv \Im \left\{ \int_1^\infty \frac{k e^{ik\tilde{x}}}{k^2 - k_n^2} \exp\left(i \frac{ky}{\sqrt{k^2 - 1}}\right) dk \right\}, n > 1 \end{aligned}$$

we rewrite the solution as

$$\Phi^{(n)} = -2\pi \cos k_n \tilde{x} [\hat{r}_n(0) \sin ny + \hat{s}_n(0) \cos ny] H(\tilde{x}) + 2\hat{s}_n(0) (I_5^{(n)} + I_6^{(n)}), n > 1$$

and examine the limit as  $\tilde{x} \rightarrow 0$ . For the first integral

$$\lim_{\tilde{x} \rightarrow 0} I_5^{(n)} = \Im \left\{ \int_0^1 \frac{k}{k^2 - k_n^2} \exp\left(-\frac{ky}{\sqrt{1 - k^2}}\right) dk \right\} = 0$$

because the integrand converges to a real number as  $\tilde{x} \rightarrow 0$ . Next we make the same transformation for  $I_6^{(n)}$  as was made in §1.4 where  $\sigma = \sqrt{k^2 - 1} |\tilde{x}|$ . Then

$$I_6^{(n)} = \Im \left\{ \int_0^\infty \sigma \frac{e^{i\sqrt{\sigma^2 + \tilde{x}^2} \operatorname{sgn} \tilde{x}}}{\sigma^2 - (k_n^2 - 1) \tilde{x}^2} \exp \left( \frac{i\sqrt{\sigma^2 + \tilde{x}^2} y}{\sigma} \right) d\sigma \right\}$$

As  $\tilde{x} \rightarrow 0$ , the integral becomes

$$I_6^{(n)} \sim \Im \left\{ \exp(iy) \int_0^\infty \frac{\sigma e^{i\sigma \operatorname{sgn} \tilde{x}}}{\sigma^2 - (k_n^2 - 1) \tilde{x}^2} d\sigma \right\}, \quad \tilde{x} \rightarrow 0$$

Now the integral behaves differently depending on whether  $\tilde{x}$  is greater or less than zero. For  $\tilde{x} > 0$  we close the contour of integration to the top and there is a pole inside the contour, giving

$$I_6^{(n)} \sim \Im \left\{ \exp(iy) \left[ i\pi + \int_0^\infty \frac{\rho e^{-\rho}}{\rho^2 + (k_n^2 - 1) \tilde{x}^2} d\rho \right] \right\}, \quad \tilde{x} \rightarrow 0^+$$

For negative  $\tilde{x}$ , the contour can be closed to the bottom, thereby excluding the singularity at  $\sigma = \sqrt{k_n^2 - 1} \tilde{x}$  and giving

$$I_6^{(n)} \sim \Im \left\{ \exp(iy) \int_0^\infty \frac{\rho e^{-\rho}}{\rho^2 + (k_n^2 - 1) \tilde{x}^2} d\rho \right\}, \quad \tilde{x} \rightarrow 0^-$$

For both  $\tilde{x} > 0$  and  $\tilde{x} < 0$  it is then necessary to evaluate the integral

$$\begin{aligned} \int_0^\infty \frac{\rho e^{-\rho}}{\rho^2 + (k_n^2 - 1) \tilde{x}^2} d\rho &= \frac{1}{2} \left[ e^{i\sqrt{k_n^2 - 1} \tilde{x}} \operatorname{Ei}_1 \left( i\sqrt{k_n^2 - 1} \tilde{x} \right) + e^{-i\sqrt{k_n^2 - 1} \tilde{x}} \operatorname{Ei}_1 \left( -i\sqrt{k_n^2 - 1} \tilde{x} \right) \right] \\ &= -\gamma - \ln \left( \sqrt{k_n^2 - 1} |\tilde{x}| \right) + \frac{1}{2} \pi \sqrt{k_n^2 - 1} \tilde{x} + \mathcal{O} \left\{ (k_n^2 - 1) \tilde{x}^2 \right\}, \quad \tilde{x} \rightarrow 0 \end{aligned}$$

Therefore

$$\begin{aligned} I_6^{(n)} &\sim \Im \left\{ \exp(iy) [i\pi H(\tilde{x}) - \ln |\tilde{x}|] \right\} \\ &\sim \pi H(\tilde{x}) \cos y - \ln |\tilde{x}| \sin y \end{aligned}$$

Finally, the behavior of  $\Phi^{(n)}$  as  $\tilde{x} \rightarrow 0$  is

$$\begin{aligned} \Phi^{(n)} &\sim -2\pi [\hat{r}_n(0) \sin ny + \hat{s}_n(0) \cos ny] H(\tilde{x}) \\ &\quad + 2\hat{s}_n(0) [\pi H(\tilde{x}) \cos y - \ln |\tilde{x}| \sin y], \quad |\tilde{x}| \rightarrow 0, n > 1 \end{aligned}$$

Taking derivatives with respect to  $\tilde{x}$  and  $y$  gives  $\tilde{\psi}^{(n)}$  and  $\tilde{w}$ , respectively.

$$\left. \begin{aligned} \tilde{\psi}^{(n)} &\sim -\frac{2\hat{s}_n(0) \sin y}{\tilde{x}} \\ \tilde{w}^{(n)} &\sim \begin{aligned} &-2\pi n [\hat{r}_n(0) \cos ny - \hat{s}_n(0) \sin ny] H(\tilde{x}) \\ &-2\hat{s}_n(0) [\pi H(\tilde{x}) \sin y + \ln |\tilde{x}| \cos y] \end{aligned} \end{aligned} \right\}, \quad \tilde{x} \rightarrow 0, n > 1$$

$$\tilde{w}^{(n)} \Big|_{0^-}^{0^+} = 2\pi n [-\hat{r}_n(0) \cos ny + \hat{s}_n(0) \sin ny] - 2\pi \hat{s}_n(0) \sin y, \quad n > 1$$

This result contains the necessary jump in spanwise velocity across the topography of

$$\tilde{w} \Big|_{0^-}^{0^+} = 2\pi n [-\hat{r}_n(0) \cos ny + \hat{s}_n(0) \sin ny]$$

but it also contains an additional, unwanted term in the jump. Furthermore,  $\tilde{w}$  and  $\tilde{\psi}$  do not decay sufficiently fast as  $\tilde{x} \rightarrow 0$ . Thus in order to eliminate these additional, unwanted terms, we add a linear multiple of the original linear solution, which was previously given as

$$\tilde{\psi} = \Re \{I_1 + I_2\}$$

$$\tilde{w} = \Re \{I_3 + I_4\}$$

To be specific, we write the outer solution as

$$\begin{aligned} \tilde{\psi} &= \left[ 4\hat{a}(0) - \sum_{n=2}^{\infty} \hat{s}_n(0) \right] \Re \{I_1 + I_2\} + \sum_{n=2}^{\infty} \Phi_{\tilde{x}}^{(n)} \\ \tilde{w} &= \left[ 4\hat{a}(0) - \sum_{n=2}^{\infty} \hat{s}_n(0) \right] \Re \{I_3 + I_4\} + \sum_{n=2}^{\infty} \Phi_y^{(n)} \end{aligned} \tag{138}$$

Thus we have accounted for the entire jump condition with the exception of first-harmonic jump caused by nonlinearities

$$\tilde{w}^{(1)} \Big|_{0^-}^{0^+} = 2\pi (\hat{r}_1(0) \cos y - \hat{s}_1 \sin y)$$

The solution for the first harmonic outer solution must satisfy

$$\begin{aligned} &(\tilde{\psi}_{yy}^{(1)} + \tilde{\psi}^{(1)})_{\tilde{x}\tilde{x}} + \tilde{\psi}_{yy}^{(1)} = 0 \\ &\tilde{\psi}^{(1)} = 0, \quad (y = 0, \tilde{x} \neq 0) \\ &\tilde{\psi}_y^{(1)} = \tilde{w}_{\tilde{x}}^{(1)} \end{aligned} \tag{139}$$

subject to the matching conditions as  $\tilde{x} \rightarrow 0$  given by

$$\left. \begin{aligned} \tilde{\psi}^{(1)} &= o\left(\frac{1}{\tilde{x}}\right) \\ \tilde{w}^{(1)} &= o(\ln |\tilde{x}|) \end{aligned} \right\} \tilde{x} \rightarrow 0$$

$$\tilde{w}^{(1)}\Big|_{0-}^{0+} = 2\pi [\hat{r}_1(0) \cos y - \hat{s}_1(0) \sin y]$$

We then write the solution as

$$\tilde{\psi}^{(1)} = \tilde{\psi}_a^{(1)} + \tilde{\psi}_b^{(1)}$$

$$\tilde{w}^{(1)} = \tilde{w}_a^{(1)} + \tilde{w}_b^{(1)}$$

where

$$\tilde{\psi}_a^{(1)} = \Re \left\{ \int_0^1 \exp\left(\frac{-ky}{\sqrt{1-k^2}}\right) e^{ik\tilde{x}} dk + \int_1^\infty \cos\left(\frac{ky}{\sqrt{k^2-1}}\right) e^{ik\tilde{x}} dk \right\}$$

$$\tilde{\psi}_b^{(1)} = \Re \left\{ \int_1^\infty \sin\left(\frac{ky}{\sqrt{k^2-1}}\right) e^{ik\tilde{x}} dk \right\}$$

$$\tilde{w}_a^{(1)} = -\Im \left\{ \int_0^1 \frac{e^{ik\tilde{x}}}{\sqrt{1-k^2}} \exp\left(\frac{-ky}{\sqrt{1-k^2}}\right) dk + \int_1^\infty \frac{e^{ik\tilde{x}}}{\sqrt{k^2-1}} \sin\left(\frac{ky}{\sqrt{k^2-1}}\right) dk \right\}$$

$$\tilde{w}_b^{(1)} = \Im \left\{ \int_1^\infty \frac{e^{ik\tilde{x}}}{\sqrt{k^2-1}} \cos\left(\frac{ky}{\sqrt{k^2-1}}\right) dk \right\}$$

such that both  $(\tilde{\psi}_a^{(1)}, \tilde{w}_a^{(1)})$  and  $(\tilde{\psi}_b^{(1)}, \tilde{w}_b^{(1)})$  independently satisfy (139). It is now necessary to determine the asymptotic behavior of this solution as  $\tilde{x} \rightarrow 0$ . We define

$$I_7 \equiv \Re \left\{ \int_1^\infty \cos\left(\frac{ky}{\sqrt{k^2-1}}\right) e^{ik\tilde{x}} dk \right\}$$

$$I_8 \equiv -\Im \left\{ \int_1^\infty \frac{e^{ik\tilde{x}}}{\sqrt{k^2-1}} \sin\left(\frac{ky}{\sqrt{k^2-1}}\right) dk \right\}$$

such that

$$\tilde{\psi}_a^{(1)} = I_1 + I_7$$

$$\tilde{w}_a^{(1)} = I_3 + I_8$$

which utilizes  $I_1$  and  $I_3$  defined in Appendix A. Then making the transformation  $\sigma =$

$\sqrt{k^2 - 1} |\tilde{x}|$  as before gives

$$\left. \begin{aligned} I_7 &\sim \Re \left\{ \frac{1}{|\tilde{x}|} \int_0^\infty e^{i\sigma \operatorname{sgn} \tilde{x}} \cos y d\sigma \right\} = \frac{\cos y}{|\tilde{x}|} \int_0^\infty \cos \sigma d\sigma \sim 0 \\ I_8 &\sim -\Im \left\{ \sin y \int_0^\infty \frac{e^{i\sigma \operatorname{sgn} \tilde{x}}}{\sqrt{\sigma^2 + \tilde{x}^2}} d\sigma \right\} = -\sin y \operatorname{sgn} \tilde{x} \int_0^\infty \frac{\sin \sigma}{\sqrt{\sigma^2 + \tilde{x}^2}} d\sigma \sim -\frac{\pi}{2} \operatorname{sgn} \tilde{x} \sin y \\ \tilde{\psi}_b^{(1)} &\sim \Re \left\{ \frac{\sin y}{|\tilde{x}|} \int_0^\infty e^{i\sigma \operatorname{sgn} \tilde{x}} d\sigma \right\} \sim \frac{\sin y}{|\tilde{x}|} \int_0^\infty \cos \sigma d\sigma \sim 0 \\ \tilde{w}_b^{(1)} &\sim \Im \left\{ \cos y \int_0^\infty \frac{e^{i\sigma \operatorname{sgn} \tilde{x}}}{\sqrt{\sigma^2 + \tilde{x}^2}} d\sigma \right\} \sim \cos y \operatorname{sgn} \tilde{x} \int_0^\infty \frac{\sin \sigma}{\sqrt{\sigma^2 + \tilde{x}^2}} d\sigma \sim \frac{\pi}{2} \cos y \operatorname{sgn} \tilde{x} \end{aligned} \right\}, \tilde{x} \rightarrow 0$$

Utilizing the previous results that  $I_1 \sim \mathcal{O}(1)$  const and  $I_3 \rightarrow 0$  as  $\tilde{x} \rightarrow 0$  gives

$$\left. \begin{aligned} \tilde{\psi}_a^{(1)} &\sim \mathcal{O}(1) \text{ const} \\ \tilde{\psi}_b^{(1)} &\sim 0 \\ \tilde{w}_a^{(1)} &\sim -\frac{\pi}{2} \sin y \operatorname{sgn} \tilde{x} \\ \tilde{w}_b^{(1)} &\sim \frac{\pi}{2} \cos y \operatorname{sgn} \tilde{x} \end{aligned} \right\}, \tilde{x} \rightarrow 0 \quad (140)$$

$$\tilde{w}_a^{(1)} \Big|_{0-}^{0+} = -\pi \sin y$$

$$\tilde{w}_b^{(1)} \Big|_{0-}^{0+} = \pi \cos y$$

Thus the solution accounting for the nonlinear components generated at the first harmonic should be

$$\begin{aligned} \tilde{\psi}^{(0)} &= \\ \tilde{\psi}^{(0)} &= 2 \left[ \hat{r}_1(0) w_b^{(1)} + \hat{s}_1(0) w_a^{(1)} \right] \end{aligned} \quad (141)$$



## D Details of Linear, Uniformly Valid Solution to Two Layers of Uniform Stratification

The governing equations for two layers of uniformly stratified flow in the linear limit are

$$\begin{aligned}\psi_{(1),yy} + N_1^2\psi_{(1)} + \beta^2 \int_{-\infty}^x \int_{-\infty}^{x'} \psi_{(1),yy} dx'' dx', \quad y < H \\ \psi_{(2),yy} + N_2^2\psi_{(2)} + \beta^2 \int_{-\infty}^x \int_{-\infty}^{x'} \psi_{(2),yy} dx'' dx', \quad y > H\end{aligned}\tag{142}$$

$$w_{(1),x} = \psi_{(1),y}$$

$$w_{(2),x} = \psi_{(2),y}$$

where  $\Psi = y + \psi$  and  $\beta = \frac{1}{Ro}$  subject to

$$\begin{aligned}\psi_{(1)} &= -\epsilon h(x), \quad y = 0 \\ \psi_{(1)} &= \psi_{(2)}, \quad y = H \\ \frac{\partial \psi_{(1)}}{\partial y} &= \frac{\partial \psi_{(2)}}{\partial y}, \quad y = H\end{aligned}\tag{143}$$

and the radiation condition.

Taking two derivatives of the equations for the streamfunction with respect to  $x$  gives

$$\begin{aligned}(\psi_{(1),yy} + N_1^2\psi_{(1)})_{xx} + \beta^2\psi_{(1),yy} &= 0, \quad y < H \\ (\psi_{(2),yy} + N_2^2\psi_{(2)})_{xx} + \beta^2\psi_{(2),yy} &= 0, \quad y > H\end{aligned}\tag{144}$$

and in Fourier space

$$k^2 (\hat{\psi}_{(1),yy} + N_1^2\hat{\psi}_{(1)}) - \beta^2\hat{\psi}_{(1),yy} = 0, \quad y < H\tag{145}$$

$$\begin{aligned}k^2 (\hat{\psi}_{(2),yy} + N_2^2\hat{\psi}_{(2)}) - \beta^2\hat{\psi}_{(2),yy} &= 0, \quad y > H \\ (k^2 - \beta^2) \hat{\psi}_{(1),yy} + N_1^2k^2\hat{\psi}_{(1)} &= 0, \quad y < H\end{aligned}\tag{146}$$

$$\hat{\psi}_{(1),yy} + \frac{N_1^2k^2}{(k^2 - \beta^2)}\hat{\psi}_{(1)} = 0, \quad y < H\tag{147}$$

$$\hat{\psi}_{(2),yy} + \frac{N_2^2k^2}{(k^2 - \beta^2)}\hat{\psi}_{(2)} = 0, \quad y > H$$

subject to the boundary condition at the topography

$$\hat{\psi}_{(1)} = -\epsilon \hat{h}, \quad y = 0 \quad (148)$$

and the matching conditions at the tropopause

$$\begin{aligned} \hat{\psi}_{(1)} &= \hat{\psi}_{(2)}, \quad y = H \\ \frac{\partial \hat{\psi}_{(1)}}{\partial y} &= \frac{\partial \hat{\psi}_{(2)}}{\partial y}, \quad y = H \end{aligned} \quad (149)$$

The general solution in the Fourier domain is

$$\begin{aligned} \hat{\psi}_{(1)} &= a(k) \exp\left(i \frac{N_1 k y}{\sqrt{k^2 - \beta^2}}\right) + b(k) \exp\left(-i \frac{N_1 k y}{\sqrt{k^2 - \beta^2}}\right) \\ \hat{\psi}_{(2)} &= c(k) \exp\left(i \frac{N_1 k y}{\sqrt{k^2 - \beta^2}}\right) + d(k) \exp\left(-i \frac{N_1 k y}{\sqrt{k^2 - \beta^2}}\right) \end{aligned} \quad (150)$$

Before imposing the boundary conditions at the topography and tropopause, it is convenient to first take the inverse Fourier transform and impose the radiation condition in the upper solution. In general, the inverse Fourier transform can be written

$$\psi_{(i)} = 2\Re \left\{ \int_0^\beta \hat{\psi}_{(i)} e^{ikx} dk + \int_\beta^\infty \hat{\psi}_{(i)} e^{ikx} dk \right\} \quad (151)$$

because the streamfunction disturbance,  $\psi$ , is a physical quantity and must be real. Taking the inverse Fourier transform of the general solution in (150) gives

$$\begin{aligned} \psi_{(1)} &= 2\Re \left\{ \int_0^\beta \left[ a \exp\left(\frac{N_1 k y}{\sqrt{\beta^2 - k^2}}\right) + b \exp\left(\frac{-N_1 k y}{\sqrt{\beta^2 - k^2}}\right) \right] e^{ikx} dk \right. \\ &\quad \left. + \int_\beta^\infty \left[ a \exp\left(i \frac{N_1 k y}{\sqrt{k^2 - \beta^2}}\right) + b \exp\left(-i \frac{N_1 k y}{\sqrt{k^2 - \beta^2}}\right) \right] e^{ikx} dk \right\} \\ \psi_{(2)} &= 2\Re \left\{ \int_0^\beta \left[ c \exp\left(\frac{N_2 k y}{\sqrt{\beta^2 - k^2}}\right) + d \exp\left(\frac{-N_2 k y}{\sqrt{\beta^2 - k^2}}\right) \right] e^{ikx} dk \right. \\ &\quad \left. + \int_\beta^\infty \left[ c \exp\left(i \frac{N_2 k y}{\sqrt{k^2 - \beta^2}}\right) + d \exp\left(-i \frac{N_2 k y}{\sqrt{k^2 - \beta^2}}\right) \right] e^{ikx} dk \right\} \end{aligned} \quad (152)$$

The radiation condition above the tropopause requires  $d(k) = 0$  for  $k > \beta$  and boundedness

as  $y \rightarrow \infty$  requires  $c(k) = 0$  for  $k < \beta$  giving

$$\begin{aligned}\psi_{(1)} = & 2\Re \left\{ \int_0^\beta \left[ a \exp \left( \frac{N_1 k y}{\sqrt{\beta^2 - k^2}} \right) + b \exp \left( \frac{-N_1 k y}{\sqrt{\beta^2 - k^2}} \right) \right] e^{ikx} dk \right. \\ & \left. + \int_\beta^\infty \left[ a \exp \left( i \frac{N_1 k y}{\sqrt{k^2 - \beta^2}} \right) + b \exp \left( -i \frac{N_1 k y}{\sqrt{k^2 - \beta^2}} \right) \right] e^{ikx} dk \right\} \\ \psi_{(2)} = & 2\Re \left\{ \int_0^\beta d \exp \left( \frac{-N_2 k y}{\sqrt{\beta^2 - k^2}} \right) e^{ikx} dk + \int_\beta^\infty c \exp \left( i \frac{N_2 k y}{\sqrt{k^2 - \beta^2}} \right) e^{ikx} dk \right\}\end{aligned}\quad (153)$$

To facilitate the application of the boundary condition, we rewrite the solution in the troposphere as

$$\begin{aligned}\psi_{(1)} = & 2\Re \left\{ \int_0^\beta \left[ f \cosh \left( \frac{N_1 k y}{\sqrt{\beta^2 - k^2}} \right) + g \sinh \left( \frac{N_1 k y}{\sqrt{\beta^2 - k^2}} \right) \right] e^{ikx} dk \right. \\ & \left. + \int_\beta^\infty \left[ f \cos \left( \frac{N_1 k y}{\sqrt{k^2 - \beta^2}} \right) + g \sin \left( \frac{N_1 k y}{\sqrt{k^2 - \beta^2}} \right) \right] e^{ikx} dk \right\} \\ \psi_{(2)} = & 2\Re \left\{ \int_0^\beta d \exp \left( \frac{-N_2 k y}{\sqrt{\beta^2 - k^2}} \right) e^{ikx} dk + \int_\beta^\infty c \exp \left( i \frac{N_2 k y}{\sqrt{k^2 - \beta^2}} \right) e^{ikx} dk \right\}\end{aligned}\quad (154)$$

The boundary condition at the surface of topography requires  $f(k) = -\epsilon \hat{h}(k)$ , giving

$$\begin{aligned}\psi_{(1)} = & 2\Re \left\{ \int_0^\beta \left[ -\epsilon \hat{h} \cosh \left( \frac{N_1 k y}{\sqrt{\beta^2 - k^2}} \right) + g \sinh \left( \frac{N_1 k y}{\sqrt{\beta^2 - k^2}} \right) \right] e^{ikx} dk \right. \\ & \left. + \int_\beta^\infty \left[ -\epsilon \hat{h} \cos \left( \frac{N_1 k y}{\sqrt{k^2 - \beta^2}} \right) + g \sin \left( \frac{N_1 k y}{\sqrt{k^2 - \beta^2}} \right) \right] e^{ikx} dk \right\} \\ \psi_{(2)} = & 2\Re \left\{ \int_0^\beta d \exp \left( \frac{-N_2 k y}{\sqrt{\beta^2 - k^2}} \right) e^{ikx} dk + \int_\beta^\infty c \exp \left( i \frac{N_2 k y}{\sqrt{k^2 - \beta^2}} \right) e^{ikx} dk \right\}\end{aligned}\quad (155)$$

Then the matching conditions of (149) give

$$\begin{aligned}
& -\epsilon \hat{h} \cosh \left( \frac{N_1 k H}{\sqrt{\beta^2 - k^2}} \right) + g \sinh \left( \frac{N_1 k H}{\sqrt{\beta^2 - k^2}} \right) = d \exp \left( \frac{-N_2 k H}{\sqrt{\beta^2 - k^2}} \right), \quad 0 < k < \beta \\
& -\epsilon \hat{h} \cos \left( \frac{N_1 k H}{\sqrt{k^2 - \beta^2}} \right) + g \sin \left( \frac{N_1 k H}{\sqrt{k^2 - \beta^2}} \right) = c \exp \left( \frac{i N_2 k H}{\sqrt{k^2 - \beta^2}} \right), \quad k > \beta \\
& N_1 \left[ -\epsilon \hat{h} \sinh \left( \frac{N_1 k H}{\sqrt{\beta^2 - k^2}} \right) + g \cosh \left( \frac{N_1 k H}{\sqrt{\beta^2 - k^2}} \right) \right] = -N_2 \left[ d \exp \left( \frac{-N_2 k H}{\sqrt{\beta^2 - k^2}} \right) \right], \quad 0 < k < \beta \\
& N_1 \left[ \epsilon \hat{h} \sin \left( \frac{N_1 k H}{\sqrt{k^2 - \beta^2}} \right) + g \cos \left( \frac{N_1 k H}{\sqrt{k^2 - \beta^2}} \right) \right] = i N_2 c \exp \left( \frac{i N_2 k H}{\sqrt{k^2 - \beta^2}} \right), \quad k > \beta
\end{aligned} \tag{156}$$

Solving gives

$$\begin{aligned}
c(k) &= \frac{2N_1 \epsilon \hat{h}(k)}{(N_2 - N_1) \exp \left( i \frac{(N_1 + N_2) k H}{\sqrt{k^2 - \beta^2}} \right) - (N_1 + N_2) \exp \left( i \frac{(N_2 - N_1) k H}{\sqrt{k^2 - \beta^2}} \right)}, \quad \beta < k < \infty \\
d(k) &= \frac{-2N_1 \epsilon \hat{h}(k)}{(N_1 + N_2) \exp \left( \frac{(N_1 - N_2) k H}{\sqrt{\beta^2 - k^2}} \right) + (N_1 - N_2) \exp \left( \frac{-(N_1 + N_2) k H}{\sqrt{\beta^2 - k^2}} \right)}, \quad 0 < k < \beta \\
g(k) &= \begin{cases} \frac{(N_1 + N_2) \exp \left( \frac{(N_1 - N_2) k H}{\sqrt{\beta^2 - k^2}} \right) + (N_2 - N_1) \exp \left( \frac{-(N_1 + N_2) k H}{\sqrt{\beta^2 - k^2}} \right)}{(N_1 + N_2) \exp \left( \frac{(N_1 - N_2) k H}{\sqrt{\beta^2 - k^2}} \right) + (N_1 - N_2) \exp \left( \frac{-(N_1 + N_2) k H}{\sqrt{\beta^2 - k^2}} \right)} \epsilon \hat{h}(k), & 0 < k < \beta \\ -i \frac{(N_1 - N_2) \exp \left( i \frac{(N_1 + N_2) k H}{\sqrt{k^2 - \beta^2}} \right) - (N_1 + N_2) \exp \left( i \frac{(N_2 - N_1) k H}{\sqrt{k^2 - \beta^2}} \right)}{(N_2 - N_1) \exp \left( i \frac{(N_1 + N_2) k H}{\sqrt{k^2 - \beta^2}} \right) - (N_1 + N_2) \exp \left( i \frac{(N_2 - N_1) k H}{\sqrt{k^2 - \beta^2}} \right)} \epsilon \hat{h}(k), & \beta < k < \infty \end{cases}
\end{aligned} \tag{157}$$

Thus the streamfunction solution is (155) with  $c(k)$ ,  $d(k)$  and  $g(k)$  given in (157).

The spanwise velocity is determined from the streamfunction solution. For the linear case, the spanwise velocity is  $w_x = \psi_y$ . Taking the Fourier transform of this gives

$$\hat{w} = -\frac{i}{k} \hat{\psi}_y \tag{158}$$

Thus the spanwise velocity can be written

$$\begin{aligned}
w_{(1)} = & 2\Re \left\{ \int_0^\beta \frac{-iN_1}{\sqrt{\beta^2 - k^2}} \left[ -\epsilon \hat{h} \sinh \left( \frac{N_1 k y}{\sqrt{\beta^2 - k^2}} \right) + g \cosh \left( \frac{N_1 k y}{\sqrt{\beta^2 - k^2}} \right) \right] e^{ikx} dk \right. \\
& \left. + \int_\beta^\infty \frac{-iN_1}{\sqrt{k^2 - \beta^2}} \left[ \epsilon \hat{h} \sin \left( \frac{N_1 k y}{\sqrt{k^2 - \beta^2}} \right) + g \cos \left( \frac{N_1 k y}{\sqrt{k^2 - \beta^2}} \right) \right] e^{ikx} dk \right\}, \quad y < H \\
w_{(2)} = & 2\Re \left\{ \int_0^\beta \frac{iN_2}{\sqrt{\beta^2 - k^2}} d \exp \left( \frac{-N_2 k y}{\sqrt{\beta^2 - k^2}} \right) e^{ikx} dk \right. \\
& \left. + \int_\beta^\infty \frac{N_2}{\sqrt{k^2 - \beta^2}} c \exp \left( i \frac{N_2 k y}{\sqrt{k^2 - \beta^2}} \right) e^{ikx} dk \right\}, \quad y > H
\end{aligned} \tag{159}$$

## E Outer Solution for Two Layers of Uniformly Stratified Flow

The integrals for the outer solution given in (98) are defined as

$$\begin{aligned}
\tilde{I}_1 &\equiv \epsilon \Re \left\{ \int_0^1 \hat{h}(\tilde{k}) \frac{N \cosh\left(\frac{N\tilde{k}(y-H)}{\sqrt{\beta^2-\tilde{k}^2}}\right) - \sinh\left(\frac{N\tilde{k}(y-H)}{\sqrt{\beta^2-\tilde{k}^2}}\right)}{N \cosh\left(\frac{N\tilde{k}H}{\sqrt{\beta^2-\tilde{k}^2}}\right) + \sinh\left(\frac{N\tilde{k}H}{\sqrt{\beta^2-\tilde{k}^2}}\right)} e^{i\tilde{k}\tilde{x}} d\tilde{k} \right\} \\
\tilde{I}_2 &\equiv \epsilon \Re \left\{ \int_1^\infty \hat{h}(\tilde{k}) \frac{N \cos\left(\frac{\tilde{k}N(y-H)}{\sqrt{\tilde{k}^2-\beta^2}}\right) + i \sin\left(\frac{\tilde{k}N(y-H)}{\sqrt{\tilde{k}^2-\beta^2}}\right)}{N \cos\left(\frac{\tilde{k}NH}{\sqrt{\tilde{k}^2-\beta^2}}\right) - i \sin\left(\frac{\tilde{k}NH}{\sqrt{\tilde{k}^2-\beta^2}}\right)} e^{i\tilde{k}\tilde{x}} d\tilde{k} \right\} \\
\tilde{I}_3 &\equiv \epsilon \Re \left\{ \int_0^1 \hat{h}(\tilde{k}) \frac{N \exp\left(-\frac{\tilde{k}(y-H)}{\sqrt{\beta^2-\tilde{k}^2}}\right)}{\sinh\left(\frac{\tilde{k}NH}{\sqrt{\beta^2-\tilde{k}^2}}\right) + N \cosh\left(\frac{\tilde{k}NH}{\sqrt{\beta^2-\tilde{k}^2}}\right)} e^{i\tilde{k}\tilde{x}} d\tilde{k} \right\} \\
\tilde{I}_4 &\equiv \epsilon \Re \left\{ \int_1^\infty \hat{h}(\tilde{k}) \frac{N \exp\left(i\frac{\tilde{k}(y-H)}{\sqrt{\tilde{k}^2-\beta^2}}\right)}{N \cos\left(\frac{\tilde{k}NH}{\sqrt{\tilde{k}^2-\beta^2}}\right) - i \sin\left(\frac{\tilde{k}NH}{\sqrt{\tilde{k}^2-\beta^2}}\right)} e^{i\tilde{k}\tilde{x}} d\tilde{k} \right\} \\
\tilde{I}_5 &\equiv \epsilon \Re \left\{ \int_0^1 -i\hat{h}(\tilde{k}) \frac{N}{\sqrt{\beta^2-\tilde{k}^2}} \frac{N \sinh\left(\frac{N\tilde{k}(y-H)}{\sqrt{\beta^2-\tilde{k}^2}}\right) - \cosh\left(\frac{N\tilde{k}(y-H)}{\sqrt{\beta^2-\tilde{k}^2}}\right)}{N \cosh\left(\frac{N\tilde{k}H}{\sqrt{\beta^2-\tilde{k}^2}}\right) + \sinh\left(\frac{N\tilde{k}H}{\sqrt{\beta^2-\tilde{k}^2}}\right)} e^{i\tilde{k}\tilde{x}} d\tilde{k} \right\} \\
\tilde{I}_6 &\equiv \epsilon \Re \left\{ \int_1^\infty -i\hat{h}(\tilde{k}) \frac{N}{\sqrt{\tilde{k}^2-\beta^2}} \frac{-N \sin\left(\frac{\tilde{k}N(y-H)}{\sqrt{\tilde{k}^2-\beta^2}}\right) + i \cos\left(\frac{\tilde{k}N(y-H)}{\sqrt{\tilde{k}^2-\beta^2}}\right)}{N \cos\left(\frac{\tilde{k}NH}{\sqrt{\tilde{k}^2-\beta^2}}\right) - i \sin\left(\frac{\tilde{k}NH}{\sqrt{\tilde{k}^2-\beta^2}}\right)} e^{i\tilde{k}\tilde{x}} d\tilde{k} \right\} \\
\tilde{I}_7 &\equiv \epsilon \Re \left\{ \int_0^1 \frac{i\hat{h}(\tilde{k})}{\sqrt{\beta^2-\tilde{k}^2}} \frac{N \exp\left(-\frac{\tilde{k}(y-H)}{\sqrt{\beta^2-\tilde{k}^2}}\right)}{\sinh\left(\frac{\tilde{k}NH}{\sqrt{\beta^2-\tilde{k}^2}}\right) + N \cosh\left(\frac{\tilde{k}NH}{\sqrt{\beta^2-\tilde{k}^2}}\right)} e^{i\tilde{k}\tilde{x}} d\tilde{k} \right\} \\
\tilde{I}_8 &\equiv \epsilon \Re \left\{ \int_1^\infty \frac{\hat{h}(\tilde{k})}{\sqrt{\tilde{k}^2-\beta^2}} \frac{N \exp\left(i\frac{\tilde{k}(y-H)}{\sqrt{\tilde{k}^2-\beta^2}}\right)}{N \cos\left(\frac{\tilde{k}NH}{\sqrt{\tilde{k}^2-\beta^2}}\right) - i \sin\left(\frac{\tilde{k}NH}{\sqrt{\tilde{k}^2-\beta^2}}\right)} e^{i\tilde{k}\tilde{x}} d\tilde{k} \right\}
\end{aligned} \tag{160}$$

## F Details - Unsteady Wind

The kernels in the nonlinear evolution equations are defined as

$$\begin{aligned}
K_{11}(x, x') &= \frac{1}{8\pi} \int_0^{2\pi} d\psi y_a \left( y'_a + (y' y'_a)_\psi - y y'_{a\psi} \right) \\
K_{12}(x, x') &= \frac{1}{8\pi} \int_0^{2\pi} d\psi y_a \left( y'_b + (y' y'_b)_\psi - y y'_{b\psi} \right) \\
K_{21}(x, x') &= \frac{1}{8\pi} \int_0^{2\pi} d\psi y_b \left( y'_a + (y' y'_a)_\psi - y y'_{a\psi} \right) \\
K_{22}(x, x') &= \frac{1}{8\pi} \int_0^{2\pi} d\psi y_b \left( y'_b + (y' y'_b)_\psi - y y'_{b\psi} \right)
\end{aligned} \tag{161}$$